Polycrystalline Silicon Capacitive MEMS Strain Sensor for Structural Health Monitoring of Wind Turbines

by

Maziar Moradi

A thesis
presented to the University of Waterloo
in fulfillment of the
thesis requirement for the degree of
Doctor of Philosophy
in
Electrical and Computer Engineering

Waterloo, Ontario, Canada, 2016

© Maziar Moradi 2016

AUTHOR'S DECLARATION

I hereby declare that I am the sole author of this thesis. This is a true copy of the thesis, including any required final revisions, as accepted by my examiners.

I understand that my thesis may be made electronically available to the public.

Abstract

Wind energy is a fast-growing sustainable energy technology and driven by the need for more efficient energy harvesting, size of the wind turbines has increased over the years for both off-shore and land-based installations. Therefore, structural health monitoring and maintenance of such turbine structures have become critical and challenging. To keep the number of physical inspections to minimum without increasing the risk of structural failure, a precise and reliable remote monitoring system for damage identification is necessary. Condition-based maintenance which significantly improves safety compared to periodic visual inspections, necessitates a method to determine the condition of machines while in operation and involves the observation of the system by sampling dynamic response measurements from a group of sensors and the analysis of the data to determine the current state of system health. This goal is being pursued in this thesis through the development of reliable sensors, and reliable damage detection algorithms.

Blade strain is the most important quantity to judge the health of wind turbine structure. Sensing high stress fields or early detection of cracks in blades bring safety and saving in rehabilitation costs. Therefore, high performance strain measurement system, consisting of sensors and interface electronics, is highly desirable and the best choice. It has been revealed that the conventional strain gauge techniques exhibit significant errors and uncertainties when applied to composite materials of wind turbine blades. Micro-electro-mechanical system (MEMS) based sensors are very attractive among other sensing techniques owing to high sensitivity, low noise, better scaling characteristics, low cost and higher potential for integration with low power CMOS circuits. MEMS sensors that are fabricated on a chip can be either bonded to the surface of wind turbine blade or embedded into the fiber reinforced composite. Therefore, MEMS technology is selected to fabricate the strain sensor in this work.

Two new sensor structures that can be used for strain measurement are designed. While the proposed sensors focus on high sensitivity, they are based on simple operating principle of comb-drive differential variable capacitances and chevron displacement amplification. Device performances are validated both by analytical solutions and finite element method simulations.

The transmission of strain fields in adhesively bonded strain sensors is also studied. In strain sensors that are attached to host structures using adhesive layers such as epoxy, complete strain transfer to the sensor is hindered due to the influence of the adhesive layer on the transfer. An analytical model, validated by finite element method simulation, to provide insight and accurate formulation for strain transfer mechanism for bonded sensors is developed. The model can predict the strain transmission ratio through a sensor gauge factor, and it clearly establishes the effects of the flexibility, length, and thickness of the adhesive layer and sensor substrate.

Several fabrication steps were required to realize the MEMS capacitive strain sensor in our lab. Polycrystalline silicon is selected as the structural layer and silicon nitride as the sacrificial layer. Polysilicon is deposited using LPCVD and SiN is deposited by PECVD in our lab. A comprehensive material study of silicon nitride and polycrystalline silicon layers is therefore performed. The whole fabrication process involves deposition, etching, and photolithography of five material layers. Although this process is developed to realize the MEMS strain sensors, it is also able to fabricate other designs of surface micromachining structures as well. The fabricated MEMS capacitive strain sensors are tested on a test fixture setup. The measurement setup is created under the probe station by using a cantilever beam fixed on one side and free on other side where a micrometer applies accurate displacement. The displacement creates bending stress on the beam which transfers to the MEMS sensor through the adhesive bond. Measurement results are in a good match with the simulation results.

Finally, a real-time non-destructive health monitoring technique based on multi-sensor data fusion is proposed. The objective is to evaluate the feasibility of the proposed method to identify and localize damages in wind turbine blades. The structural properties of turbine blade before and after damage are investigated and based on the obtained results, it is shown that information from smart sensors, measuring strains and vibrations, distributed over the turbine blades can be used to assist in more accurate damage detection and overall understanding of the health condition of blades. Data fusion technique is proposed to combine the diagnostic tools to improve the detection system with providing a more robust reading and fewer false alarms.

Acknowledgements

First, I would like to thank my advisor, Professor Siva Sivoththaman. Even though I came from a different technical background, he believed in my passion and trusted me to work in his lab. I deeply appreciate the amount of independence he gave me, which helped me pursue my ideas. His guidance through this work helped me a lot in accomplishing this research work. I would also like to offer my thanks to the members of my dissertation committee, Professor Yang, Professor Lien, Professor Mansour, and Professor Saini for their constructive questions and suggestions that all helped elevate the quality of this work.

I had a great opportunity to work at the CAPDS Lab for fabrication of MEMS devices. I would like to express my deepest appreciation to our lab manager Mr. Joseph Street to maintain all the equipment in our lab. I learned a lot about microfabrication, electrical engineering, and science from him. I would like to thank all my colleagues for all the discussions we had on our research projects. It has been a unique experience learning about so many different projects, and incorporating all the valuable insights earned, in my research. I am especially thankful to Dr. Bahareh Sadeghimakki and Dr. Roohen Tarighat for training me with some cleanroom equipment when I started to work in this group. I had the pleasure to have wonderful colleagues, Dr. Ehsan Fathi, Dr. Christopher Baldus-Jeursen, Lin Tian, Zhen Gao, Nasim Bakhshizadeh, Dr. Bita Janfeshan, Dr. Navid Jahed, Mohsen Mahmoudysepehr, Shadi Dashmiz and Lilly Zheng. I am grateful to Dr. Albert Chen, Dr. Ali Najafi Sohi, and Ahmed Abdel Aziz for all the useful discussions we had about MEMS, and their helps and advice on my research.

I would like to sincerely appreciate my parents for their never-ending love and unconditional support. Last but not least; I am deeply grateful to my dearest friend, my love, and my wife, Nadia. Taking this journey without her endless love and support was indeed impossible.

Table of Contents

List of Figures ix
List of Tables xii
1. Introduction 1
1.1 Structural Health Monitoring of Wind Turbines 1
1.2 Essential Structural Health Parameters 4
1.3 Research Motivations 7
1.4 Objectives of Research 9
1.5 Thesis Outline 10
2. Literature Review of Damage Detection Methods and Strain Sensors 12
2.1 Condition Monitoring of Wind Turbines 12
2.2 Wind Turbine Blade Damage Detection Techniques 12
2.2.1 Conventional strain gauges 12
2.2.2 Acoustic emission sensors 13
2.2.3 Fiber optic sensors 13
2.2.4 Other techniques 14
2.3 Strain Sensor Technology 14
2.3.1 Metal Strain Sensors 16
2.3.2 Semiconductor strain sensors 17
2.3.3 Piezoelectric Strain Sensors 18
2.3.4 Surface Acoustic Wave Strain Sensors 18
2.3.5 Fiber Optic Strain Sensors 18
2.4 Silicon Micromachined MEMS Strain Sensing 20
3. Design and Simulation of MEMS Strain Sensors 21
3.1 Introduction 21
3.2 Capacitive Sensing Modes 23
3.3 Chevron-based Mechanical Motion Amplification 24
3.3.1 Theoretical Analysis and Bending Model Derivation 25

3.3.2 Finite Element Modeling 28
3.4 Motion Amplified Capacitive Strain Sensors 30
3.4.1 Variable-gap Design 30
3.4.2 Variable-area Design 31
3.5 FEM Simulation Results 31
3.6 Resonant Strain Sensor 31
3.7 Conclusions 32
4. Modeling and Analysis of Strain Transfer to the MEMS Sensors 37
4.1 Introduction 37
4.2 Strain Analysis and Model Development 39
4.3 Finite Element Analysis 44
4.4 Results and Discussions 46
4.4.1 Effects of Adhesive Layer's Geometry and Mechanical Properties 46
4.4.2 Effects of Sensor Substrate 47
4.5 Strain Transmission Enhancement 47
4.6 Conclusions 51
5. Material and Technology Development for MEMS Sensor Fabrication 52
5.1 Introduction 52
5.2 Process Design and Material Selections 52
5.3 Process Development of PECVD Silicon Nitride 55
5.3.1 Introduction 55
5.3.2 Experimental procedure 57
5.3.3 Results and discussions 58
5.3.4 Selection of the optimal process conditions 67
5.4 Process Development of LPCVD Polycrystalline Silicon 69
5.4.1 Introduction 69
5.4.2 Deposition process 69
5.4.3 Deposition of polysilicon by LPCVD in our lab 72
5.4.4 Characterization methods 73

5.4.5 Results and discussions ... 74
5.4.6 Optimum deposition conditions ... 76
5.5 Photolithography, Pattern Transfer, and Plasma Etching ... 77
5.6 Process Integration for MEMS Device Fabrication ... 79
6. Measurement and Characterization of Fabricated MEMS Sensors ... 85
6.1 Bent cantilever Beam Test Setup ... 85
6.2 Displacement Under Microscope ... 88
6.3 Evaluation of MEMS Sensors ... 889
6.3.1 Strain sensors bonding and adhesive materials ... 89
6.3.2 Measurement results of variable-gap design sensor ... 90
6.3.3 Measurement results of variable-area design sensor ... 90
6.4 Conclusions ... 92
7. Development of Multisensor Approach for Reliable Management of Sensors Signals ... 93
7.1 Introduction ... 93
7.2 Damage Detection Methodology ... 95
7.2.1 Strain distribution perturbation analysis ... 96
7.2.2 Natural frequency analysis ... 97
7.3 Multisensor Fusion Model ... 98
7.3.1 Fusion module for sensor validation ... 98
7.3.2 Fusion module system health diagnosis ... 100
7.4 Simulation and Results ... 102
7.4.1 Finite element method model ... 102
7.4.2 Effect of damage on strain fields ... 102
7.4.3 Effect of damage on natural frequencies ... 103
7.5 Multisensor Fusion Model Validation ... 106
7.6 Conclusions ... 107
8. Conclusions ... 110
Bibliography ... 113

List of Figures

Fig. 1.1: Global annual and cumulative installed wind energy capacity 2
Fig. 1.2: Wind , high load, or lightning strike induced broken, damaged, or burned blades... 4
Fig. 2.1: The Huggenberger tensometer with its double lever mechanism 17
Fig. 2.2: Characteristic design of a metal foil strain gauge 17
Fig. 2.3: Piezoelectric strain sensor, Fiber optic strain sensor, and Basic SAW filter. 19
Fig. 3.1: Illustration of five different possible capacitive sensing modes. 24
Fig. 3.2: Basic idea of sacrificial layer etching. 24
Fig. 3.3: Displacement amplification microdevice with four Chevron-beams 26
Fig. 3.4: The fixed-guided schematic and the variables used in the solution. 27
Fig. 3.5: Comparison of mechanical gain obtained analytically and by FEM simulation using COMSOL Multiphysics® at different inclination angles. 29
Fig. 3.6: Effect of both bent-beams length and inclination angle on mechanical gain obtained analytically a different points. 29
Fig. 3.7: Variable-gap comb-drive capacitive sensor consisting of interdigitated fixed and movable electrodes. 33
Fig. 3.8: Variable-area comb-drive capacitive sensor consisting of interdigitated movable electrodes 33
Fig. 3.9: A zoom view showing electrodes displaced from their original positions due to the applied strain. 34
Fig. 3.10: Complete design of the variable-gap and variable-area design sensors simulated in COMSOL Multiphysics® with the mechanical and electrical interconnections between four comb-drive structures. 34
Fig. 3.11: Simulation results of the MEMS strain sensors performance characteristics 35
Fig. 3.12: Device structure and its shape change on its first mode at 24kHz. 36
Fig. 3.13: The COMSOL Multiphysics® FEM simulation result showing the resonant frequency change rate for the applied strains 36
Fig. 4.1: 3D schematic of the strained host structure, bonding layer and the substrate......... 40
Fig. 4.2: Displacement equilibrium diagram of the investigated adhesive bonded structure. 40
Fig. 4.3: Strain distribution in the sensor substrate along the length of the bonding layer for various values of Γ. 43
Fig. 4.4: Strain distribution of the host structure along the length of the bonding layer for various values of Γ. 44
Fig. 4.5: Finite element model of the investigated adhesive bonded structure. 45
Fig. 4.6: The close agreement of the FEA simulation results and the analytical solutions. .. 45
Fig. 4.7: Shear stress distribution in the adhesive layer. 46
Fig. 4.8: Simulation results describing the influence of adhesive layer thickness on sensor

gauge factor at different values of sensor length. ... 47
Fig. 4.9: Simulation results describing the effect of mechanical properties (Young's Modulus) of the bonding adhesive layer on sensor gauge factor at different values of thicknesses. ... 48
Fig. 4.10: Simulation results describing the effect of sensor substrate thickness and its mechanical properties on sensor gauge factor at different values of length. ... 49
Fig. 4.11: Tapered structure to achieve higher uniformity. The dashed line displays the strain distribution of the substrate.. ... 49
Fig. 4.12: Etched surface trench on the silicon chip made where the sensing MEMS element is going to be placed. This technique enhances the transferred strain up to 30%... 50
Fig. 4.13: Another proposed model with geometrical features in substrate to enhance the strain transmission ratio. The complete etched away feature reduces the stiffness of the substrate and increases the overall gauge factor. ... 50
Fig. 5.1: Cross sectional view showing all 5 layers of the process flow (not to scale). ... 54
Fig. 5.2: Schematic diagram of Plasmalab Oxford PECVD chamber used for SiN deposition in this study. ... 59
Fig. 5.3: Plasmalab Oxford PECVD in our lab used for SiN deposition. ... 59
Fig. 5.4: SiN film's deposition rate versus temperature and pressure ... 63
Fig. 5.5: SiN film's total stress versus temperature and pressure ... 63
Fig. 5.6: SiN film's etch rate versus temperature and pressure ... 64
Fig. 5.7: SiN film's refractive index versus temperature and pressure ... 64
Fig. 5.8: SiN film's deposition rate versus gas ratio and plasma power ... 65
Fig. 5.9: SiN film's total stress versus gas ratio and plasma power ... 65
Fig. 5.10: SiN film's etch rate versus gas ratio and plasma power. ... 66
Fig. 5.11: SiN film's refractive index versus gas ratio and plasma power ... 66
Fig. 5.12: The infrared transmission spectra of SiN film deposited at different measurement temperatures. ... 67
Fig. 5.13: Optical micrograph of the cracked SiN film surface. ... 68
Fig. 5.14: LPCVD machine in our lab with gass conections and the schematic of the tube. 72
Fig. 5.15: Effect of silane flow rate and temperature on deposition rate polysilicon. ... 74
Fig. 5.16: Top: Raman measurement of three different deposition temperature showing the better crystallinity at higher temperatures. Bottom: Different gas flow rates deposited at 630°C showing that lower flow rate causes less residual stress of the polysilicon film. ... 75
Fig. 5.17: Effect of residual stress on free standing structure. The structure is buckled up due to the compressive residual stress before annealing. ... 77
Fig. 5.18: The starting wafer is RCA cleaned, followed by a 300 nm layer of SiN 1 followed by a layer of 300 nm of Poly 1. The wafer is then coated with photoresist. The photoresist is patterned by exposing it to UV light through the first level mask and

then developing it. Plasma etching is used to remove the unwanted polysilicon. This method of patterning the wafers with photoresist, etching and stripping the remaining photoresist is used repeatedly in the process. 80
Fig. 5.19: A 2.0 µm layer of SiN 1 is deposited on the wafers by PECVD to serve as the sacrificial layer. Then the wafer is coated with photoresist and the anchors are patterned and then plasma etched... 81
Fig. 5.20: A 2 µm layer of n-doped polysi is deposited by LPCVD followed by a 950°C/5 min anneal. The anneal serves to activate dopants, grow grain sizes and reduce the residual stress. Then Poly 2 is etched by plasma processing. After the etch is completed, next the metal layer is deposited by lift-off patterning which does not require etching. Finally, the structure is released by immersion in BHF solution.. 82
Fig. 5.21: Scanning electron micrographs of the final device (design 1) 83
Fig. 5.22: Scanning electron micrographs of the final device (design 2) 84
Fig. 6.1: Pictures of MEMS sensors bonded to Plexiglas and Silicon substarte in the text setup under probe station and also schematics of bent cantilever test setup........... 86
Fig. 6.2: FEM analysis of strain distribution on a cantilever beam showing the distorted distribution close to the clamped side of the beam. 87
Fig. 6.3: Displacement of fingers after application of 500µε of tensile strain...................... 88
Fig. 6.4: Measured capacitance output characteristic of variable gap design sensor, bonded to the substrate using wax and epoxy adhesives. 90
Fig. 6.5: Measured capacitance output characteristic of variable area design sensor, bonded to the substrate using wax and epoxy adhesives. ………………………………... 91
Fig. 7.1: Cross section of a wind turbine blade with a small crack of 2 cm depth and 3mm opening is implemented in the model. The inset shows how strain field distribution is disturbed due to a notch-shaped crack on the blade. 97
Fig. 7.2: Kalman filtering to achieve accurate estimates of sensor readings. 99
Fig. 7.3: The operation of the proposed intelligent turbine damage detection system.. 101
Fig. 7.4: The generated mesh and the finite element model of the blade used for COMSOL simulations. 103
Fig. 7.5: Simulation of stress distribution and deflection of a healthy blade. In this particular case, the tip of the blade is deflected about 20cm. 104
Fig. 7.6: FEM simulation output showing the variation in stress fields of a damaged blade model. The inset shows sudden decrease around the damage location and increase beneath or at both corner sides of the crack. 104
Fig. 7.7: Strain in vicinity of the crack for healthy and damaged blades. Sudden decrease of strain magnitude is detectable even at locations as far as more than 1 m on each side of the crack... 105
Fig. 7.8: Sensor validation and damage detection reasoning process map. 108
Fig. 7.9: Simulation results for the multisensor damage detection architecture.. 109

List of Tables

Table 1.1: List of different parameters which are important either for health monitoring of the structure or better controlling and efficient operation of wind turbines. 6
Table 3.1: chevron beams FEM simulation physical characteristics..................................... 28
Table 4.1: Dimensions and mechanical properties used in the analytical solution and finite element analysis. 43
Table 5.1: Summary of performed recipes. 60
Table 5.2: Responses of film properties to variation of process conditions. 68
Table 7.1: Natural frequency comparison between undamaged and damaged states........... 106

1. Introduction

With constant growth in population and economic worldwide, energy consumption, mostly fossil energy, has increased rapidly to improve the living conditions. However, due to the recent energy crisis, as fossil energy is rather limited, and the need to get clean energy, renewable energy resources have obtained great attention. Among different types of renewable energy sources, because of relative cost effectiveness and maturity of the technology, wind energy is the most attractive and many countries are relying more on wind power. Fig. 1.1 shows the annually and cumulative installed wind energy capacity from 1997 to 2014 around the globe. In 1997, there was only 1530 MW of wind energy generating capacity installed. However, this number increased to 51473 MW in 2014. In the USA alone, 65879 MW of installed wind capacity was available as of 2014, and 9694 MW in Canada [1].

1.1 Structural Health Monitoring of Wind Turbines

Toward more efficient energy harvesting, the size of wind turbines has increased over the years and an increasing number of wind turbines will be built at off-shore sites in the future due to environmental requirements and a limited number of on-shore sites with favorable wind potential. Such turbines are difficult and expensive to be accessed. Therefore, maintenance, repair works, and structural health monitoring (SHM) of the turbine structure have been made more difficult and at the same time essential as structural damage may invoke catastrophic detriment to the integrity of the system. Damage and failure can happen at any part of a wind turbine but considerable attention has been given to the blades as they are the main elements of the system, they cost sometimes up to 20% of the total cost and the most expensive type of damage to repair. Moreover, rotating damaged blade will cause other secondary damages to the whole wind turbine. Damage to a blade can occur in various ways but they can be extensively avoided by developing successful

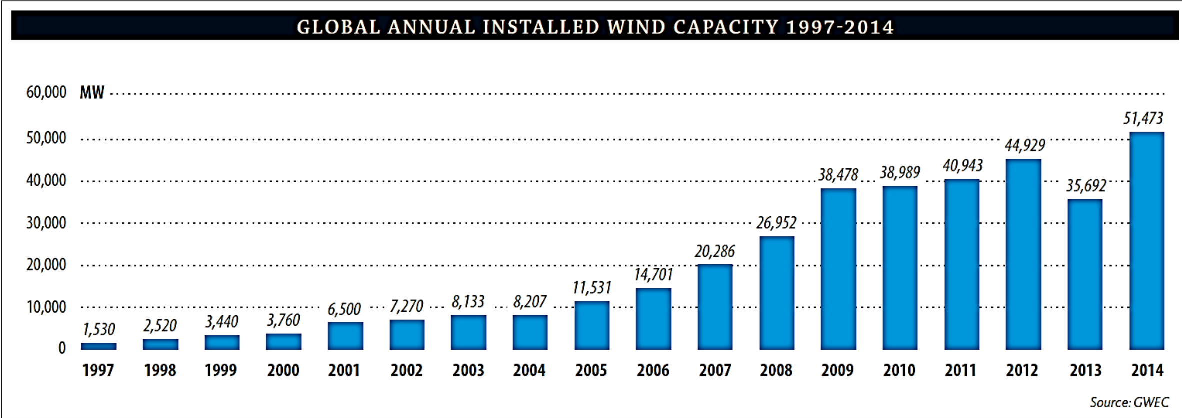

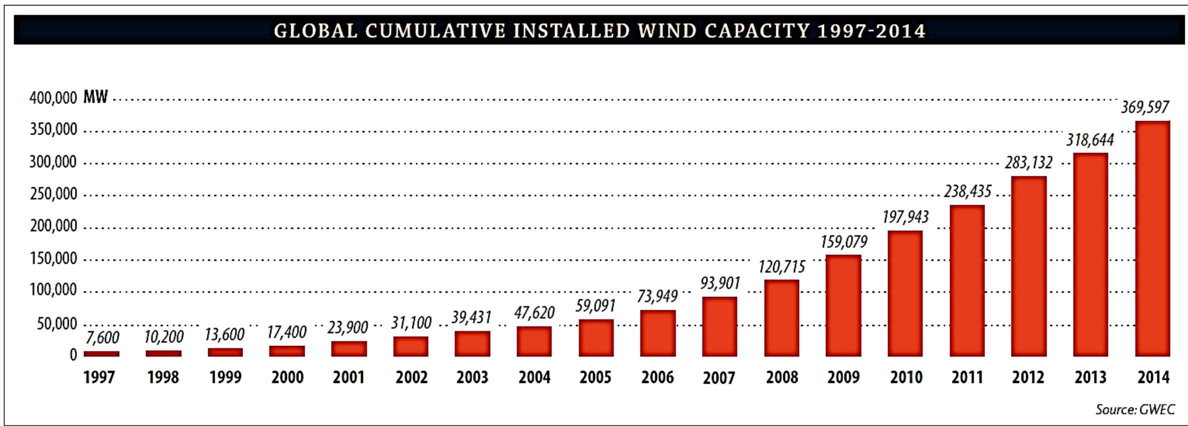

Fig. 1.1: Global annual and cumulative installed wind energy capacity 1996–2014 (Adapted from Ref. [1])

health monitoring method which sensing technology and the associated signal interpretation algorithms are its key factors. As defined by Li *et al.* [2], SHM refers to the use of in situ measurements and analyses of key structural and environmental parameters under operating conditions in order to provide early warnings about abnormal states or accidents to avoid damages and also sending feedbacks for maintenance and rehabilitation requirements. Damage can be changes to the material or geometric properties of a structure that adversely affect structural functions and performance [3]. The advantages of applying damage detection or SHM techniques on wind turbines are [4]: reducing expensive labor costs for regular manual inspection, preventing unnecessary replacement of components, reducing downtimes and frequency of breakdowns, improving reliability of power generation while preventing overload of the turbine, avoiding replacement by repairing the detected damage location in advance, etc.

Structural health monitoring refers to the damage detection and monitoring of various properties of a structural system. The term 'health' involves damage, loading and operational capability of a

turbine. The successful application of SHM has been used for the damage diagnosis in other rotating machinery, aircrafts, bridges, and structures like oil rigs too [3]. Previously, to ensure maximum operating time between shutdowns, machines were used to be running until break, but that breakdowns were occasionally catastrophic. This type of maintenance is called corrective maintenance and immediate repair or replacement of the failed part may be necessary and unscheduled downtime will result. Preventive maintenance was the first response to concerns for safety and production loss. In this case, maintenance or monitoring of the machine is performed by periodic scheduled non-destructive evaluations and visual observations, or even replacement of parts at regular time intervals regardless of condition. This method requires more frequent maintenance works and therefore more expenses than necessary. However recently, condition-based maintenance (CBM) is increasingly being used instead [5]. Condition-based maintenance is performed when one or more indicators (sensors) show that the structure is going to fail and needs maintenance. This type of maintenance significantly increases safety and saves a lot in cost, and it has been widely accepted that the use of sensors for damage detection is economically feasible and even advantageous in industry [6], [7]. This requires a way to determine the condition of machines while in operation and involves the observation of the system by sampling dynamic response measurements from a group of sensors and the analysis of the data to determine the current state of system health, or as discussed before, a successful structural health monitoring system. In order to build such a system, first we have to know important parameters to judge the structural health condition of a wind turbine.

Damage and failure can happen at any part of a wind turbine; it can be rotor blade, drive train, moment transmitting components, hydraulic system, braking system, safety devices and sensors, transformer station, even the tower and concrete foundation, and so on [8]. Different types of stress [9], fatigue [10], wind gusts, moisture, corrosion and even lightning strikes [11] are the main causes of wind turbine structural damages (see Fig. 1.2). Although damage at any component is important, as it was also mentioned before, considerable attention has been given to the blades. They are the main elements of the system, they cost sometimes up to 20% of the total cost and the most expensive type of damage to repair [11]. Moreover, rotating damaged blade will cause other secondary damages to the whole wind turbine. Finally, studies have also shown that break or other damages of the blade is the most frequent damage of wind turbine systems [12–14].

Fig. 1.2: Wind, high load, or lightning strike induced broken, damaged, or burned blades (Adapted from Ref. [16])

Damage to a blade can occur in various ways [15] but they can be extensively avoided by developing successful health monitoring method which sensing technology and the associated signal interpretation algorithms are its key factors. For better diagnosis of potential damage or problems, even multiple sensors can be deployed to simultaneously monitor the structure. Hence, the SHM process would involve performing periodic measurements from an array of sensors, signal analysis and extraction of damage indicating features and determining the current status of structural health of the system. Moreover, to achieve high efficient wind turbines, realizing a practical monitoring system requires characterization of the dynamic behavior as essential as health monitoring of the structure. Suitable sensors and controlling devices are also able to preserve wind turbine dynamic stability and enhance performance under variable wind conditions.

1.2 Essential Structural Health Parameters

Table 1.1 lists essential parameters either for health monitoring of the blade structure or better

controlling and efficient operation of wind turbines. Among these parameters, the most important one which is blade strain is the subject of this research work. After understanding how sensing this parameter can help us creating a successful SHM technique and showing that strain sensing, both temporal and in spatial domain serve as a good indicator for continuous damage detection and catastrophic failure prediction, the primary objective of the research reported here is to develop and fabricate a sensor for real-time detection of blade damages in wind turbines.

Wind turbine blades are subject to various types of loads. The aerodynamic force, the weight, the centrifugal forces, the inertial force (during shutdown and start-up), and some other intermittent forces are major sources of load on the blades. There are two types of aerodynamic forces from the wind. The drag force which is almost in the horizontal direction along the direction of wind, and the lift force which is in the vertical plane. These forces are functions of wind speed, pitch angle, and rotation speed. They also change in different operation conditions [17]. Blades are also subject to their own weight and a centrifugal force along the length of blade when rotating. The magnitude of the weight force is constant but the direction changes with respect to the blade during rotation. On the other hand, the centrifugal force direction is always in the outward direction with respect to the blade but its magnitude changes with the turbine rotation speed. However, the magnitude of the centrifugal force is normally higher than the weight even at low rpm. One of the most critical load is the flapwise bending load that become dangerous specially when the wind turbine is parked and the blade is hit by extreme wind or when the braking system fails and the blades spin out of control [18].

All the different types of loads mentioned above will create tensile, compressive or bending stresses, and like any other materials and components, blades undergo shape changes or strains. High or long lasting strain may lead to crack formation, yielding, or fatigue in the structure material. Micro-fractures form too, when composite structure of wind turbine blade is under stress or like other structures and components when blade undergoes progressive damage due to loading conditions, environmental effect and other factors. High stress fields then create bigger cracks and this leads to possible turbine failures. Therefore, blade strain is one of the most important quantities to judge the health of wind turbine structure. Sensing high stress fields or early detection of cracks in blades bring safety and saving in rehabilitation costs. Therefore, high performance strain measurement system, consisting of sensors and interface electronics, is highly desirable.

Table 1.1: List of different parameters which are important either for health monitoring of the structure or better controlling and efficient operation of wind turbines.

Essential Parameters	Comments
Blade Strain (Loading)	▪ Best parameter for load measurement of wind turbine blades. ▪ Excessive (compressive or tensile) strain will cause composite failure. ▪ Crack and delamination can be detected using strain sensors. ▪ Excessive strain will lead to fatigue. ▪ Strain gauge is able to measure the strain.
Blade Acceleration & Vibration	▪ Excessive vibration or a change in natural frequency of the system is an early indication of damage. ▪ Extreme change in velocity can lead to fatigue. ▪ Change in eigen modes can be detected with accelerometers. ▪ An accelerometer or strain sensor can be used to detect the frequency of vibration. ▪ Vibration sensor can be placed at tip where acceleration is greatest.
Wind Speed, Wind Gust & Turbulence	▪ High wind failure must be detected rapidly or otherwise the turbine spins out of control. ▪ Wind turbine control systems cannot efficiently operate without wind parameter data. ▪ Turbulence measurement using piezoelectric microphone.
Temperature & Humidity	▪ Temperature effect on blade material. ▪ Temperature gradient over the blade. ▪ As a corrective factor for sensing elements. ▪ Humidity is an important cause of delaminations and debondings in blades.

Researches on wind turbine load measurements have been carried out for many years and it has been revealed that the conventional strain gauge techniques exhibit significant errors and uncertainties when applied to composite materials of wind turbine blades. On the other hand, blades for large wind turbines can reach up to 70 meters and consequently the areas swept are huge which may cause the structures to be subjected to effects that are barely evident on smaller machines. In particular, the wind field will not be uniform over the area and one blade experiences conditions that are different to others. The wind load at each blade should be sensed independently to operate the rotor in a more balanced condition. Sometimes, this is not only the matter of maximum strain; excessive strain exacerbates the growing effects of fatigue. By controlling the stress, the potential for damage over time is reduced and the wind turbine's operational life prolongs.

Application of multiple strain sensors can provide useful information on strain distributions along the blade. This can be extremely helpful since strain distribution will considerably change in proximity of cracks. Therefore, by use of strain sensors it is possible to measure changes in strain distribution caused by propagating damages. The necessary number of sensors and how close they have to be placed depends on the size of damage the system is monitoring (this subject is carefully studied in Chapter 7). Nonlinear behavior of the blade obtained from strain sensor measurements also give good indication of how close the blade is to a failure [19]. It is very important to note that instead of distributing the sensors all over the blade, we can alternatively place the sensors only in the damage hot spots. This will reduce the number of sensors and simplify the data processing and analysis. The critical fact here is the importance of optimal placement of the sensor which produces reliable data about damages or impending failures [20]. Different hot spots or the locations where damage is likely to happen are observed or simulated and reported in articles. For example, 30% and 70% in length from the root of the blade are found to be prone to damage [21], [10]. Damage to the tower can also happen and the possible tower failure may create a catastrophic accident and a total damage of the turbine. Tower must be built in a way that is able to support tall and high capacity turbines. However, it has been found that collapse of the tower is one of the common causes of turbine accidents [14]. So, a successful strain measurement method can also be applied to the tower and prevent any possible failures [22].

1.3 Research Motivations

Wind turbine blades are subject to various types of loads that causes tensile, compressive or bending stresses on them and undergo shape changes or strains. High or long lasting strain may lead to crack formation, yielding, or fatigue in the structure material. Loading conditions, environmental effect and other factors form progressive damages and micro-fractures. High stress fields then create bigger cracks and possible turbine failures. Therefore, strain would be the most fundamental parameters for health monitoring the structure and sensing high stress fields and early detection of cracks ensure safety and cost-saving operation. As it is not possible to eliminate stress and strain in structures and machines, reliable monitoring systems consisting of sensors and interface electronics are highly desirable to prevent catastrophic failures.

Microelectromechanical system (MEMS) based sensors are very attractive among other sensing principles and techniques due to several. Conventional strain sensors based on piezoelectric elements or metal foils are inadequate for high performance and low cost applications due to their large temperature dependence, lower sensitivity, and incompatibility to standard CMOS integration. Fiber optic strain sensors, despite several advantages, have certain limitations too. For example, a large number of interconnects are required in order to create the fiber optic network, and probably surface treatment is needed. When each sensor is wired to a central processing unit, damage to any paths would also cause the entire sensor to be lost. Silicon micromachining technology can be used to fabricate MEMS-based strain sensors with micron-scale dimensions which enable point strain measurement with high accuracy. Among the different sensing principles, MEMS capacitive sensors are attractive because of their suitability for integration with low power CMOS circuits, low noise, high dynamic range, minimum temperature dependence, and excellent sensitivity. Therefore, the ultimate goal of this research is to design MEMS sensors for strain measurement of wind turbine blades. The proposed structure must be simple, highly sensitive, and linear. First, the concept model should be tested by finite element method (FEM) simulations. After validation of the proposed design, the MEMS sensor is to be realized in our lab through several microfabrication process steps.

With the sensors becoming more miniaturized and high in accuracy, the properties of the medium that bonds the sensor to the wind turbine blade become critical. The overall sensor design should also include the bonding layers, taking into account their geometric dimensions and mechanical properties in order to achieve a near-unity strain transfer ratio. Therefore, consideration must be given to the load transfer from one adherend to another through an adhesive medium. A realistic and accurate analytical model should be drawn and even techniques for improving the strain transfer be proposed based on the modeling results. The presented analysis can also be used to calibrate strain sensors.

As only one single damage indicator is not reliable, practical health monitoring schemes often combine different analysis methods. In most cases, single sensors cannot be fully reliable to always deliver accurate information. In a structure like a turbine blade, sensors are placed in different locations and for better damage detection technique; multiple properties must be observed simultaneously. Fusing sensors measurement data can provide robust reading and finally correct

inferences can be drawn. A successful system based on this technique includes multiple sensors mounted in different locations over turbine blade. The data monitored by the sensors, must be sent to the controller for transmission to other sensors, actuators, or subsystems. Therefore, the sensor system has to combine the MEMS-based sensing technology with the signal and data processing components, or even wireless communicating part (probably, RF-MEMS, or an antenna). Following the last decade progress in the field of MEMS technology and the fabrication of integrated chips that has been achieved, realizing a MEMS-based chip consists chiefly of micro-sensors, micro-actuator, communication, and signal processing components will be extremely desirable and useful in this application. This wireless capability relieves the burden of cabling issues which will be extremely favored in wind turbine application.

1.4 Objectives of Research

The objectives of this research are:

- Important parameters in wind turbine structural safety is to be studied and the most important property and the right technology should be selected to judge the health of a wind turbine.
- To perform a review of current damage detection techniques and to explain specifications required of an ideal sensor and the properties generally used to judge the quality of a sensor.
- Efficient and implementable sensor to be designed, and simulated. The design of the sensors must be done for simple fabrication methods and be possible to be fabricated in our lab.
- The mechanism of transferring the mechanical properties from wind turbine blade to the MEMS sensor should be studied and understood. Considering the geometric dimensions and mechanical properties, to predict the behavior and achieve correct readings.
- An integrated and fully in-house fabrication process is to be developed which involves comprehensive material study too.
- A suitable test platform setup should be created to evaluate the performance of fabricated sensors.
- To propose a damage detection algorithm based on multi-sensor technique that combines the diagnostic tools to improve the detection system with more robust and reliable reading of sensors signal data and fewer false alarms.

1.5 Thesis outline

Chapter 1 – Introduction: Importance, advantages, and different methods of health monitoring of wind turbines is discussed. A list of important parameters in wind turbine structural safety is studied. Blade strain was selected as the most important property to judge the health of wind turbine. Finally, MEMS was proposed as the best technology for fabricating such sensors.

Chapter 2 – Literature Review of Damage Detection Methods and Strain Sensors: A review of the state-of-the-art in the condition monitoring of wind turbines, describing the different maintenance strategies and damage detection techniques is provided. Stress and strain are briefly explained and specifications of an ideal sensor and the properties generally used to judge the quality of a strain sensor are listed. Finally, a brief overview of competing strain sensing technologies and their advantages and disadvantages are given.

Chapter 3 – Design and Simulation of MEMS Strain Sensors: Two new physical designs for sensors that can be used for strain measurement are presented. While the proposed sensor designs focus on high sensitivity, they are based on simple operating principle of comb-drive differential variable capacitances and displacement amplification. The bent beams convert small amount of applied strains to measurable changes in capacitance of comb fingers. The design of the structures enables simple fabrication methods for the realization of the sensors. Device performances are validated both by analytical solution and finite element method simulations. The obtained nominal capacitance is 25 fF, with sensitivities of 13 aF and 2.7 aF per microstrain (με) while demonstrating maximum strain range of ±1000 με and ±1800 με, respectively for the first and second designs. As a resonant strain sensor, the first design exhibits a sensitivity of about 8.6 Hz/με.

Chapter 4 – Modeling and Analysis of Strain Transfer of the Designed MEMS Sensors****s:*** The transmission of strain fields in adhesively bonded MEMS strain sensors is analyzed. In strain sensors that are attached to host structures using adhesive layers such as epoxy, complete strain transfer to the sensor is hindered due to the influence of the adhesive layer on the transfer. This chapter presents an analytical model, validated by finite element method simulation, to provide insight and accurate formulation for strain transfer mechanism for bonded sensors. A shear-lag parameter has been introduced to account for the component geometry and properties. The model is capable of predicting the strain transmission ratio through a sensor gauge factor, and it clearly

establishes the effects of the flexibility, length, and thickness of the adhesive layer and MEMS sensor substrate. Finally, modifications to sensor substrates, by the implementation of micromachined tapered edges and trench etching, are proposed in order to increase the strain transmission ratio. It has been found, for the selected case study, that the sensor sensitivity could be enhanced by up to 30%. This work on bonding analysis is applicable for performance prediction and calibration in sensor systems design.

Chapter 5 – Material and Technology Development for MEMS Sensor Fabrication: Several fabrication steps are required to realize the capacitive strain sensor. Polycrystalline silicon is selected as the structural layer and silicon nitride as the sacrificial layer. Polysilicon is deposited using LPCVD and SiN is deposited by PECVD in our lab. A comprehensive material study of silicon nitride and polycrystalline silicon layers is performed. The whole process involves deposition and photolithography of five material layers. Although this process is developed to realize the MEMS strain sensor designs but also it is able to fabricate other designs of surface micromachining as well.

Chapter 6 – Measurement and Characterization of Fabricated MEMS Sensors: This chapter presents the test results of the fabricated MEMS capacitive strain sensor and its related test fixture setup and bonding. The measurement setup is created by a cantilever beam fixed on one side and free on other side where a micrometer applies accurate displacement. The displacement creates bending stress on the beam which transfers to the MEMS sensor through the adhesive bond. Measurement results are in an acceptable match with the simulation results.

Chapter 7 – Development of Multisensor Approach for Reliable Management of Sensors Signals: A real-time non-destructive health monitoring technique based on multi-sensor data fusion is proposed. The objective is to evaluate the feasibility of the proposed method to identify and localize damages in wind turbine blades. The structural properties of turbine blade before and after damage are investigated through different sets of finite element method simulations. Based on the obtained results, it is shown that information from smart sensors, measuring strains and vibrations, distributed over the turbine blades can be used to assist in more accurate damage detection and overall understanding of the health condition of blades. Data fusion technique is proposed to combine these two diagnostic tools to improve the detection system with providing a more robust reading and fewer false alarms.

2. Literature Review of Damage Detection Methods and Strain Sensors

2.1 Condition Monitoring of Wind Turbines

Condition monitoring systems are combination of sensors and signal processing equipment that provide continuous indications of wind turbine condition based on different techniques. These systems monitor the status of critical components such as blades, generator, gearbox, bearings and tower to detect indications of developing failure. A good technique with appropriate data acquisition and signal processing can detect faults while the turbine is operational and damage prevention actions can be planned in time. In this way, downtime and maintenance costs are reduced and at the same time reliability and safety are increased.

2.2 Wind Turbine Blade Damage Detection Techniques

Numerous wind turbine blade damage detection, condition monitoring, and structural health monitoring devices and techniques exist, each with its own advantages and disadvantages, majority of these methods have limitations with regard to large-scale sensing, difficult signal interpretation, or have safety issues.

2.2.1 Conventional strain gauges

Strain gauges have been traditionally used for measuring stress and are easily recognizable. They are typically metal foil pattern bonded on a flexible substrate. The flexible substrate is also bonded to the monitored structure. The strain transferred to the metal foil changes its resistivity and is measure by a simple connected circuit. The disadvantage of metal foil strain gauges is that they

are not reliable on the long term and prone to failure. They are also very sensitive to lightning strikes. Furthermore, they suffer from ambient noise and this reduces their sensitivity to some types of blade damages [23].

2.2.2 Acoustic emission sensors

Acoustic emission (AE) sensors are piezoelectric crystals that monitor sound/stress waves propagating on the blade surface due to structural damages such as breakage, delamination, or debonding [24]. The most interesting property of AE sensors is that they do not need excitation, and will work passively by listening to sound waves. The disadvantage of AE sensors is that they must be located very close to damage locations, and also meaningful interpretation of AE signals are sometimes difficult.

2.2.3 Fiber optic sensors

Fiber optic (FO) sensing [25] is the most widely used method for SHM of wind turbine blades. It works based on the principle of the power reduction of the light passing through the fiber depends on the strain of the structure that the fiber is attached to. Fiber optic strain sensors are currently applied in wind turbine structural monitoring because of their light weight, immunity to electromagnetic interference, and their lightning safety. Among different types of FO strain sensors [25], fiber Bragg gratings (FBGs) have the advantage of a direct relation between the measured Bragg wavelength and strain [26]. Despite many advantages, there are certain limitations to FO sensors too. In order to create the fiber optic network, a lot of interconnects are required and this poses a challenge to its implementation and probably requires surface treatment. Each sensor is wired to a central processing unit and if any path is damaged, the sensor is entirely lost. Hence a discrete sensor network will offer a significant advantage in this case (discrete strain measurement will be sensitive to the choice of location, the bonding and protection methods though). Also, optical techniques require complex signal analysis especially for a large array of sensors. A sharp bend in the fiber optic will affect the reading and it cannot be used a completely conformal sensor. Although temperature variation does not affect the optical properties but it will cause expansion or contraction of the optical fiber and this will make it challenging to attribute the signal variation to strain or temperature change. Finally, fiber optic sensors are sometimes too expensive for some applications [27].

2.2.4 Other techniques

There are several other damage detection techniques. Ultrasonic testing [28] is a technique that an ultrasonic wave passes through the material and will face mode conversion by defects if existed; Thermal imaging method [29] detects temperature differences due to surface defects by infrared sensors; X-ray radioscopy [30] reveals cracks or delaminations detecting variations in attenuation of X-ray in propagation paths; Eddy current [31] method detects the presence of flaw if secondary magnetic field is modified. There are also other methods such as: PZT patches [32], smart materials and strain memory alloy method [33] wavelet transforms [34], microwave techniques [35], etc.

Sensing and control mechanisms deploying devices based on MEMS receive serious consideration due to their fast response, high accuracy, stability, and minimum size and weight. They can provide successful operation of condition monitoring systems and therefore better energy capture efficiency of wind turbines. At the same time, low cost sensing possibility of MEMS sensors and its compatibility for integration with CMOS technology for data analysis are the key factors to obtain wind turbine reliability goals. Fabrication of an integrated MEMS sensor capable of sensing the important parameters for wind turbine structural health is the ultimate goal of this research work.

2.3 Strain Sensor Technology

Strength of material calculation has been the common method of assessing structural parts of machines, buildings, vehicles, aircrafts, etc. This method is only acceptably accurate when the component loads are qualitatively and quantitatively known. The risk of overloading was traditionally countered by using safety margins, for example by over-dimensioning. However, in order to reduce the cost and to save weight, modern design strategies demand savings in material. At the same time, the material stresses must be known to satisfy the safety requirements and to deliver a satisfactory component service life. Therefore, measurements under operational conditions, or as it was discussed before, condition based measurements are necessary. The mechanical stress that the material is subjected is the most important quantity employed in the evaluation of structural parts. However, mechanical stresses are practically impossible to determine under operational conditions, but a practical method based on a relationship between

the material stress and the resulting deformation, called 'strain', which was discovered by Hooke can be used instead for the experimental determination of material stresses. Strain also occurs on the surface of objects and is therefore accessible for measurement and the results can be used for experimental stress analysis.

Two basic types of force can produce stress on a body, surface forces and body forces. Surface forces act on the surfaces and are exerted when bodies come in contact with each other. Body forces act on each element of the body and the most common examples are gravitational and centrifugal forces. Stress is defined as the surface force acting on a solid body per unit area of a differential volume element. When the stress is perpendicular to the surface, it is called normal stress (σ), and shear stress (τ) when the force is acting along the face. The unit commonly used for stress is N/m^2. The body is deformed when stress is applied to it and the consequent differential deformation is called strain (ε). Normal stress causes normal strain, or uniaxial strain, which is defined as the ratio of change in length to the original length. Shear stress creates shear strain that shows movement of plates over each other (γ). Strain is unit less and generally expressed in micro strain.

The relationship between stress and strain is required in mechanical modeling and it varies greatly depending on material properties. At low normal stresses, all materials show linear relationship with the proportionality constant known as Young's modulus (E). Brittle materials like silicon are broken when the stress reaches the yielding stress. Ductile materials like nickel have straight stress-strain relationship at low stress but a nonlinear one around the yielding point. Similarly shear modulus (G) is also defined for shear stress and shear strain relationship.

As it was explained before, stress analysis and strain measurement is the best way to assess the structural health of a wind turbine. The development of strain sensors has had different paths and they have been fabricated based on different technologies such as mechanical, optical, acoustical, electrical, and etc. Although no strain sensor has all the specifications required of an ideal sensor, the properties generally used to judge the quality of a strain sensor are the following [36]:

- It should be able to measure strains with high accuracy.
- The sensor size should be as small as possible.
- The calibration constant should not vary with time, temperature, or other factors.

- The response control speed of the sensor which is mainly controlled by its structure inertia should be sufficient for fast dynamic measurements.
- It should be inexpensive, and easy to install and operate.
- It should present a linear response over a wide range.
- Has minimum effect on strain distribution of the host structure.

Over the years, a large number of strain sensors with different designs have been developed. Cumbersome mechanical devices such as *Huggenberger* and *Johansson Mikrokator* were the first strain sensing devices invented and used which measures and displays the strain using a lever ratio of about one thousand. Despite the ingenious design of such devices, their range of application and significance are restricted due to the several intrinsic disadvantages such as the restriction of making only static measurements. As a result of these shortcomings, electrical measurement techniques emerged to provide solution.

2.3.1 Metal strain sensors

Following the publication of experimental results obtained by Lord Kelvin and Charles Wheatstone, attention was given to measuring change of resistance in an electrical conductor due to the effects of mechanical stress using Wheatstone bridge circuit. Due to number of reasons, many years passed until the first strain sensor based on this effect was developed. Eventually, the metal foil strain sensor, or strain gauge, was produced by Saunders and Roe in 1952. The simplified structure is shown in Fig. 2.1, it is a metallic foil pattern which is supported by an insulating flexible backing. The strain gauge is attached to the host structure by an adhesive material. As the host structure deforms, the metal foil is deformed too and undergoes tension or compression. This dimension change causes the metal foil resistance to increase or decrease. The resistance variation depends on the amount of deformation and is measured using a Wheatstone bridge. The change in resistance and consequently the sensitivity of sensors can be increased by using piezoresistive metals. Resistivity of piezoresistive materials change when undergo mechanical strains. Copper-Nickel, Nickel-Chromium, Iron-Chromium-Aluminum, Platinum-Tungsten and some other metallic alloys exhibit this property well and are used in fabrication of such sensors. Metal film grids are fragile and easy to break. So, the metal film is always bonded to a plastic backing sheet and obviously, an adhesive layer must be used to bond the strain gauge to the host structure.

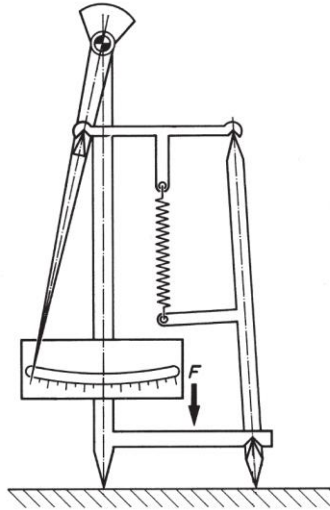

Fig. 2.1: The Huggenberger tensometer with its double lever mechanism [adapted from Ref. 34].

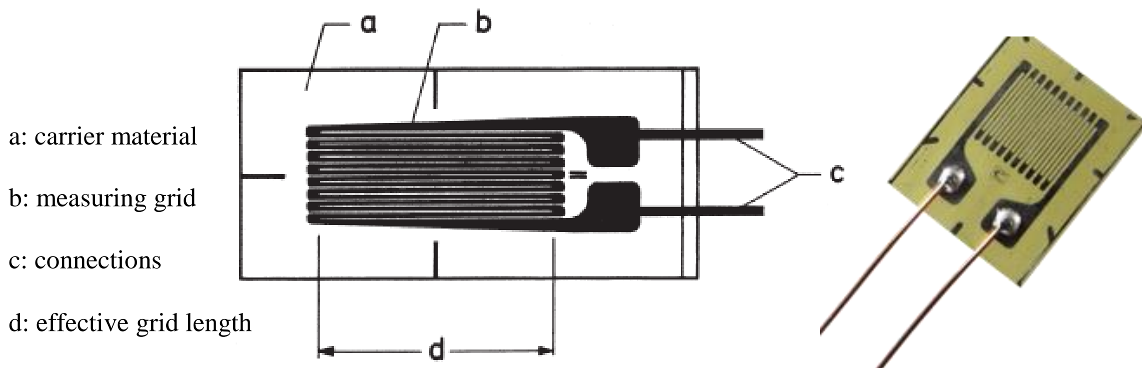

Fig. 2.2: Characteristic design of a metal foil strain gauge [adapted from Ref. [37] and [38].

A wide variety of adhesive materials are available for this purpose. Factors such as operating temperature, the curing temperature, the maximum strain, and acceptable strain transfer are important in selecting the suitable adhesive material. Metal foil strain sensors (see Fig. 2.2) were manufactured in different types for various measurement tasks and conditions. Their adaptability, accuracy, and being somewhat easy to install made their use widespread in the field of general-purpose experimental stress analysis.

2.3.2 Semiconductor strain sensors

Semiconductor strain sensors are the other type of electrical resistive strain sensors. The measurement concept is based on the piezoresistive effect in semiconductors discovered by C.S. Smith in 1954. Germanium was initially used, but was replaced later by silicon. They are sort of

similar to metal foil strain sensors in construction. They consist of a thin layer of semiconductor fixed to an insulating carrier foil and connecting gold leads. Semiconductor strain sensors gained a very good market due to their high sensitivity (gauge factor) which is about fifty to sixty times that of metal strain gauges. However, this advantage is balanced with several disadvantages like high cost, limited range, large temperature effect, nonlinear characteristics, and being brittle.

2.3.3 Piezoelectric strain sensors

If a piezoelectric material such as quartz is used as the sensing part of transducers, the sensor creates electrical charge on its surfaces which is proportional to the applied strain and can be measured with charge amplifiers. Barium titanate is another common piezoelectric material but the latest piezoelectric strain sensors which are widely used in structural health monitoring are using lead zirconate titanate piezoelectric ceramic (PZT). It is fabricated in patches and is bonded to the monitored structure (See Fig. 2.3a). The PZT patches are piezoelectric materials which generate surface charges in response to mechanical stresses and conversely experience mechanical deformations when electric field is applied. In the above mentioned technique, the PZT patch is excited by an alternating voltage, this produces deformations, and the response of the area is transferred back to the PZT in the form of impedance. Any damage to the structure manifests itself as a deviation in impedance. Piezoelectric materials show instability in properties at higher temperatures which affects the sensor's reliability. Also, this sensor has large impedance at the output which requires custom designed measurement electronics for signal conditioning.

2.3.4 Surface acoustic wave strain sensors

Surface acoustic waves (SAW) sensors [41] can detect temperature, strain, mass, conductivity, and other phenomena. SAW sensors measure changes in the path over which the acoustic waves travel [42] (See Fig. 2.3c). Although these sensors had some commercial success but they suffer from current issues and packaging problems. Also, SAW devices are typically fabricated on piezoelectric substrates and this limits the flexibility in reducing CTE mismatch with other materials.

2.3.5 Fiber optic strain sensors

Fiber optic strain sensors are currently the most widely used in wind turbine structural monitoring

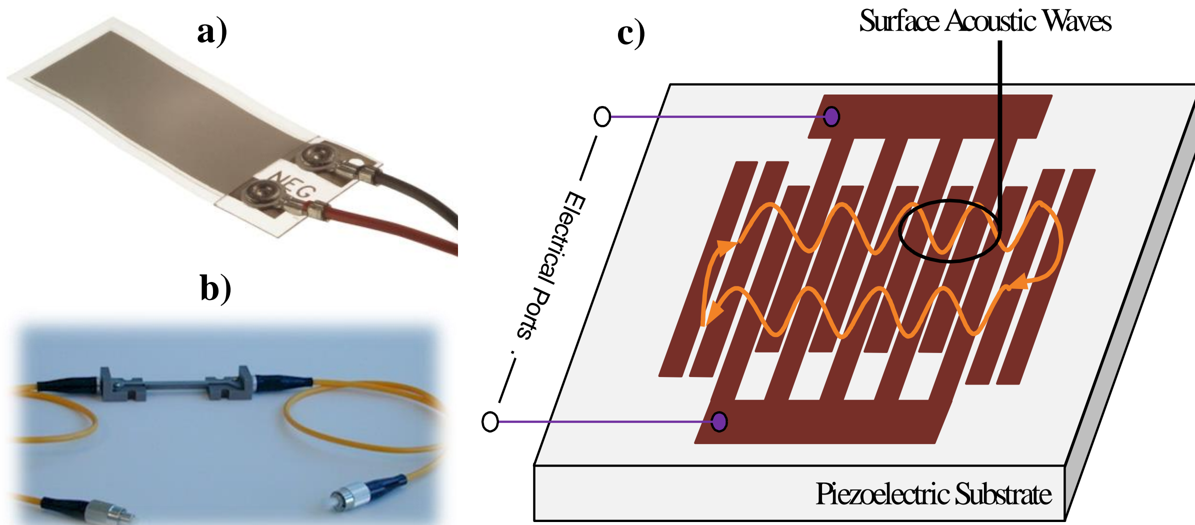

Fig. 2.3: a) Piezoelectric strain sensor [adapted from Ref. [39], b) Fiber optic strain sensor [adapted from Ref. [40], and c) Basic SAW filter.

because of their light weight, being immune to electromagnetic interference, and their lightning safety. Among different types of FO strain sensors, fiber Bragg gratings (FBGs) (See Fig. 2.3b) have the advantage of a direct relation between the measured Bragg wavelength and strain. Developing a network of embedded optical fibers has been focused for measuring strain in composites recently. Plastic optical fibers are attached to the blades to measure loads. Depending on the amount of strain, the optical power reduces when it goes through the fiber. This mechanism can be used to measure the strain. Despite the many advantages, there are certain limitations to this sensor too. In order to create the fiber optic network, a lot of interconnects are required and this poses a challenge to its implementation and probably require surface treatment. Each sensor is wired to a central processing unit and if any path is damaged, the sensor is entirely lost.

There are numerous other methods and devices for strain sensing such as capacitive strain sensors, surface acoustic wave strain sensors, etc. Although there is a large volume of commercialization for strain sensors to increase the reliability of structures; temperature and environmental sensitivity, size, and power requirements are some of the major disadvantages of strain sensors. On the other hand, silicon micromachined MEMS sensing is intrinsically insensitive to temperature fluctuation, capable of performing accurate measurement at low power, and monolithically integrable with CMOS circuits to achieve a smart sensor.

2.4 Silicon Micromachined MEMS Strain Sensing

Most force and torque measurement devices utilize the long and well established resistance strain gauge technology. Unfortunately, the metallic resistance strain gauge is relatively insensitive, their rangeability and overloading capabilities are seriously restricted, and consumes relatively high electrical power. In general, measurement instrumentation now needs smaller sensing devices of lower power consumption, more capabilities, and greater compatibility with digital microelectronics. Noncontact, wireless, and batteryless devices are sometimes desirable.

Furthermore, conventional strain gauges measure strain over a small region of the body along a short line but strain measured in this way is not done at a point as the definition of strain requires. If strain distribution over the body (or strain field) is constant or has a linear function, the measurement will be accurate. However, for the case of quadratic strain fields or any other arbitrary strain fields, the strain measurement made this way will not be exact. So, to reduce the error introduced in certain strain fields, great effort has been done to decrease the gauge length. Discrete sensor network can offer significant advantages which will be discussed later. In this case the strain measurement will be sensitive to the choice of location. Sensors can be even placed in structural damage hot spots to reduce the number of sensors required.

Semiconductor and MEMS technology can be used to fabricate small and sensitive sensors that are able to create such these accurate measurements on stiffer structures such as wind turbine blade at much lower strain levels. However, semiconductor based piezoresistive sensors show high dependence on temperature, and are susceptible to electrical noise. So, their usage is generally limited to applications which involve small strains. Silicon micromachined technology can be used to fabricate strain sensors with dimension of micrometer and at the same time with very high accuracy. MEMS based strain sensors are more attractive among other sensing principles and techniques due to different advantages such as high sensitivity, low noise, better scaling characteristics, low cost and higher potential for monolithic integration with low power CMOS circuits. MEMS strain sensors that are fabricated on a chip can be either bonded to the surface of blade or embedded into the fiber reinforced composite. Although the latter case poses several distinct challenges possibly of poor load/strain transfer; poor adhesion to the surface may cause the same problem.

3. Design and Simulation of MEMS Strain Sensors*

3.1 Introduction

As it was explained in the previous chapter, MEMS based physical sensors have received great attention due to their fast response, high accuracy, stability, and minimal size and weight. They can lead to efficient and reliable monitoring systems due to their low cost and compatibility for integration with CMOS technology. Strain is one of the most fundamental parameters for health monitoring in structures to ensure their proper operation. Sensing high stress fields or early detection of cracks ensure safety and cost-saving [7], [8]. As it is not possible to eliminate stress and strain in structures and machines, reliable monitoring systems with sensors and interface electronics are desirable to prevent catastrophic failures.

Conventional strain sensors based on piezoelectric elements [43] or metal foils are inadequate for high performance and low cost applications due to their large temperature dependence, lower sensitivity, and incompatibility to standard CMOS integration. Fiber optic strain sensors [25] are currently widely used, especially in wind turbine structural monitoring, because of their light weight, immunity to electromagnetic interference, and their lightning safety. Despite these advantages, there are certain limitations to this sensor too. For example, a large number of interconnects are needed in order to create the fiber optic network, probably requiring surface treatments. When each sensor is wired to a central processing unit, damage to any paths would also cause the entire sensor to be lost.

---

* Based on a published manuscript: M. Moradi and S. Sivoththaman, "Design and modelling of a chevron MEMS strain sensor with high linearity and sensitivity," *IEEE Sensors J.*, vol. 15, no. 9, 2015.

And a published manuscript: M. Moradi and S. Sivoththaman, "MEMS strain sensors with high linearity and sensitivity with an enhanced strain transfer mechanism for wind turbine blades," *Proc. Microtech2012*, Santa Clara, CA, June 2012.

And a presented work: M. Moradi and S. Sivoththaman, "Structural health monitoring of wind turbines using a new microelectromechanical based blade strain sensor," *WindPower2012*, Atlanta, GA, June 2012.

Silicon micromachining technology can be used to fabricate MEMS-based strain sensors with micron-scale dimensions which enables point strain measurement with high accuracy. Among the different sensing principles, MEMS capacitive sensors are attractive because of their suitability for integration with low power CMOS circuits [44], low noise, high dynamic range, minimum temperature dependence, and excellent sensitivity. Parallel plate MEMS capacitive sensor operation is generally based on change in spacing or in overlap area.

In this chapter, two strain sensing devices with high sensitivity and linearity for both tensile and compressive cases are presented. The structures utilize differential capacitive strain sensing and mechanical amplification mechanism. An interdigitated comb drive design is used for capacitance changing. Comb drives are widely used for electrostatic actuation and capacitive position sensing, and they are an essential part of MEMS devices such as gyroscopes [45], microscanners [46], and accelerometers [47]. The mechanical amplifier is composed of four bent-beams to enhance the motion of the comb-drive structure. While mechanical motion amplification has been used in various MEMS devices [48–50], there has not been much work published on the application to strain sensors. Chu *et al.* [51] proposed combination of mechanical amplification and comb-drive structure and Senesky *et al.* used it as a MEMS strain sensor for structural health monitoring and harsh environment sensing [52], [53]. In this chapter, a very accurate analytical model is developed considering large displacement of the beams to precisely predict the deflection behavior of the beams is verified by Finite Element Method (FEM) simulations. The concept of using bent-beams and differential capacitive measurements is used in the proposed structure and modified to exhibit high sensitivity.

Furthermore, the proposed designs are not complicated and can be realized using simple surface micromachining MEMS fabrication techniques. At the same time, they present some advantages over existing micromachined MEMS strain sensors. The feasibility of the proposed variable-gap comb drive design to be used as a resonant strain sensor is also reported. Physical resonant sensors [54] are generally based on the resonant frequency change induced by changes in structure stress or mass. FEM simulation performed on the proposed variable gap sensor design shows a sensitivity of 8.6 Hz/$\mu\varepsilon$.

3.2 Capacitive Sensing Modes

One of the most important precision sensing mechanisms is capacitive (or electrostatic). The physical structure of capacitive displacement sensors is simple and the inherent nonlinearity is often dominated by their simplicity and small temperature coefficient. The problem of measuring very small capacitance changes in the presence of large parasitics is mitigated with the possible monolithic integration of signal conditioning circuitry. Various possible capacitive sensing modes are illustrated in Fig. 3.3. In case 1, the distance between the plates is varied, which leads to a nonlinear relationship between spacing and capacitance change if capacitance is measured directly, but the output is linear if capacitive impedance is measured instead. In case 2, an intermediate plate is moved relative to two fixed plates, creating differential measurements. Cases 3 and 4, represent single and differential modes where the overlap area of the plates is varied, providing greater linearity but suffers from higher effects of existing fringing fields. The last case has varying dielectric constant between the plates. Capacitive sensor structures are relatively simple to fabricate and comb-type capacitors are commonly used in surface micromachined devices which is based on varying the overlapping area. However, at such small scales fringing fields can become very significant. Finally, capacitive transduction is less noisy than resistive, but the noise performance of capacitive approach is not always better than resistive. Particularly, surface micromachining results in extremely small (femto or atto farad) capacitances.

MEMS Surface micromachining is a CMOS compatible fabrication technique and provides free-standing structures and allows a higher structure density than bulk- micromachining. The main idea of surface micromachining is the sacrificial layer concept as shown in Fig. 3.2. The structural layer defines the movable part of the device and it is deposited on the sacrificial layer. After patterning the structural layer the sacrificial layer is removed in an isotropic etch process. Variable capacitors can be fabricated by MEMS micromachining technology, either surface- or bulk-micromachining. Surface-micromachined variable capacitors are simpler to fabricate, can be integrated on the same chip as existing circuitry, and use less expensive process steps.

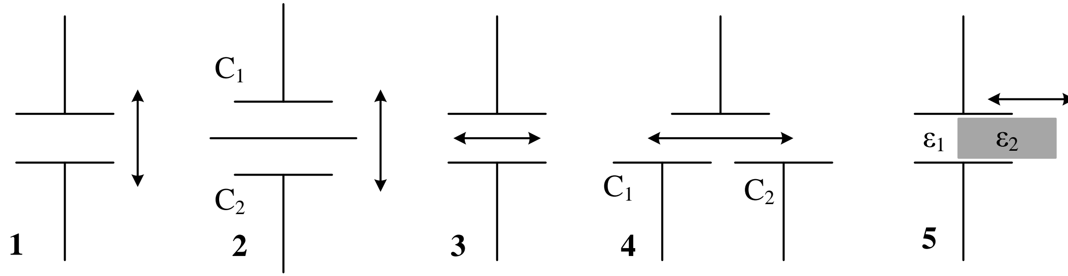

Fig. 3.1: Illustration of five different possible capacitive sensing modes.

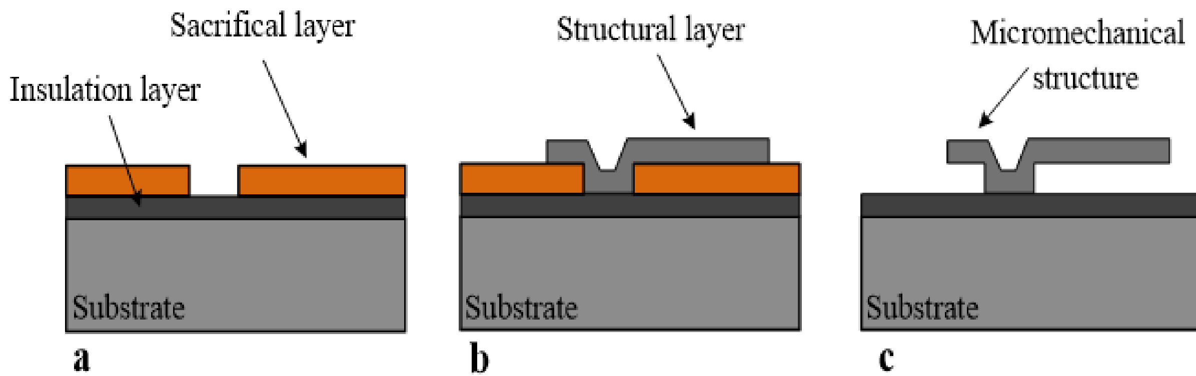

Fig. 3.2: Basic idea of sacrificial layer etching.

3.3 Chevron-based Mechanical Motion Amplification

The operation principle of MEMS capacitive sensors is based on displacement to create an output signal. Depending on the design, the displacement modifies gap distance or area of capacitances. By amplifying the deflection of the sensing elements and hence higher capacitive signal, the sensitivity can be greatly enhanced. As schematically shown in Fig. 3.3, a simple mechanical motion amplifier can be designed by four inclined straight beams, also called Chevron beams [55] or bent beams [56], to convert the strain-induced horizontal displacement into amplified vertical movement. Application of an input force, which is the strain transferred to the sensor substrate from the host structure [57], will generate deformation of a flexure-based mechanism. Then, the input displacement created by this force will be amplified in another direction where comb-drive structured capacitors are placed. The proposed structure converts small amount of applied strain to measurable changes in capacitance. The mechanical motion amplifier based on Chevron beams does not add Brownian noise nor increase the electronic noise level and therefore, the SNR of the sensor [58] is greatly improved.

3.3.1 Theoretical analysis and bending model derivation

The mechanical gain of the compliant mechanism shown in Fig. 3.3 is a function of the beam geometry, mechanical properties, and the original inclination angle. Several modelling techniques have been proposed to predict the performance and to derive an equation for the mechanical gain. Euler-Bernoulli beam equation is one of them but it is not able to precisely predict the deflection particularly in large deflection regimes due to some simplifying assumptions [59]. Other techniques are either too complicated or based on numerical methods, including pseudo rigid body model [60], circle-arc method [61], Adomian decomposition method [62], and finite element methods. In order to achieve an exact analytical solution, this section focuses on the modelling of a fixed-guided beam by employing the schematic shown in Fig. 3.4. A comprehensive elliptic integral [63] solution is used to solve the large deflection of the beam. A novel contribution of this part is the insight achieved by solving the exact behavior of Chevron-beam structures over a large range of deflection instead of using simplifying assumptions and limiting deflection to small values. The bending model developed here presents an exact analytical solution for a fixed-guided end beam which is the case for the mechanical motion amplification microdevice. The model assumes constant moment of inertia and modulus of elasticity. The Bernoulli- Euler equation for the bending moment at an arbitrary point on the beam in Fig. 3.4 is,

$$M = EI\frac{d\theta}{ds} = Fycos\psi_0 - Fxsin\psi_0 \qquad (3\text{-}1)$$

where x and y are the coordinates of the point, EI is the flexural rigidity of the beam, F is the applied force due to the strained substrate and ψ_0 is the inclination angle. We also have,

$$\frac{dy}{ds} = sin\theta , \qquad \frac{dx}{ds} = cos\theta \qquad (3\text{-}2)$$

Differentiating Eq. (3-1) with respect to s gives

$$EI\frac{d^2\theta}{ds^2} = Fsin\theta cos\psi_0 - Fcos\theta sin\psi_0 \qquad (3\text{-}3)$$

Integrating Eq. (3-3) with respect to θ gives,

$$\frac{EI}{2}\left(\frac{d\theta}{ds}\right)^2 = -Fcos\theta cos\psi_0 - Fsin\theta sin\psi_0 + C \quad (3\text{-}4)$$

Eq. (3-4)can be rewritten as,

$$\frac{d\theta}{ds} = \lambda^{-1}\sqrt{C' - cos(\theta - \psi_0)} \ , \qquad \lambda = \sqrt{\frac{2F}{EI}} \qquad (3\text{-}5)$$

Solving for *ds* in Eq. (3-5) and assuming an inextensible beam gives the integrals for displacements,

$$L = \int_0^L ds = \int_0^{\theta_i} \frac{2\lambda}{\sqrt{C' - \cos(\theta - \psi_0)}} d\theta \qquad (3\text{-}6)$$

$$H_y = \int_0^L sin\theta ds = \int_0^{\theta_i} \frac{2\lambda sin\theta}{\sqrt{C' - \cos(\theta - \psi_0)}} d\theta \qquad (3\text{-}7)$$

$$H_x = \int_0^L cos\theta ds = \int_0^{\theta_i} \frac{2\lambda cos\theta}{\sqrt{C' - \cos(\theta - \psi_0)}} d\theta \qquad (3\text{-}8)$$

In order to bring the integrals to the standard form of elliptic integrals, a new variable, φ, is introduced to satisfy the following equations;

$$C' = 2k^2 - 1 \ , \qquad \cos(\theta - \psi_0) = 2k^2 sin^2\varphi - 1 \qquad (3\text{-}9)$$

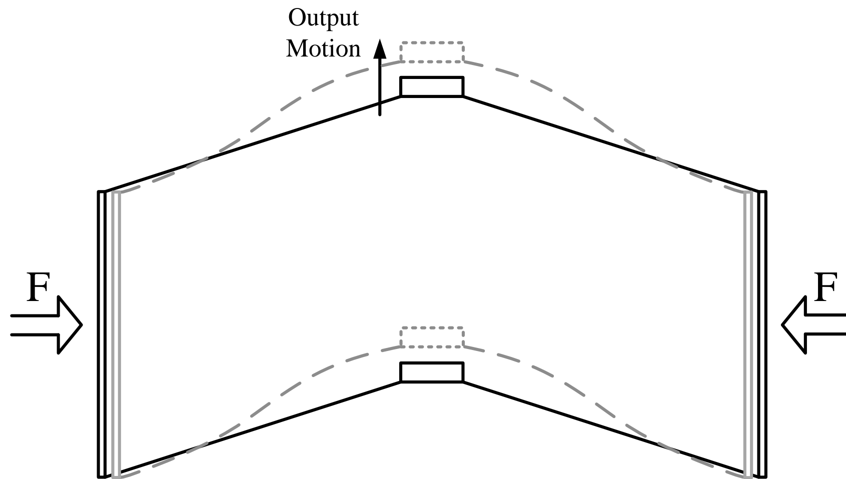

Fig. 3.3: Displacement amplification microdevice with four bent-beams. The gray dashed line shows the deflection of the structure after applying forces.

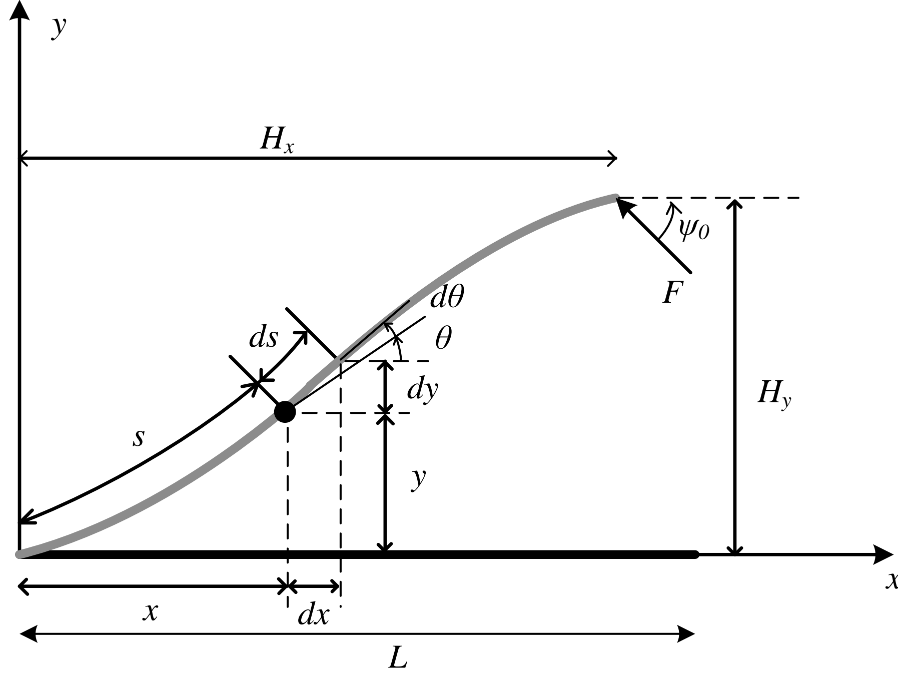

Fig. 3.4: The fixed-guided schematic and the variables used in the solution.

which using trigonometric identities and substituting Eq. (3-9) into Eq. (3-6) gives

$$L = 2\sqrt{2}\lambda \int_{\varphi_1}^{\varphi_2} \frac{d\varphi}{\sqrt{1 - k^2 sin^2\varphi}} \tag{3-10}$$

Using the definition of the incomplete elliptic integral of first kind [64],

$$L = 2\sqrt{2}\lambda \, [F(k, \varphi_2) - F(k, \varphi_1)] \tag{3-11}$$

And similarly,

$$\begin{gathered} H_y = 2\sqrt{2}\lambda \, [\, 2kcos\psi_0(cos\varphi_2 - cos\varphi_1) \\ -sin\psi_0\big(2E(k, \varphi_2) - 2E(k, \varphi_1) + F(k, \varphi_1) - F(k, \varphi_2)\big) \,] \end{gathered} \tag{3-12}$$

$$\begin{gathered} H_x = 2\sqrt{2}\lambda[\, -2ksin\psi_0(cos\varphi_2 - cos\varphi_1) \\ -cos\psi_0\big(2E(k, \varphi_2) - 2E(k, \varphi_1) + F(k, \varphi_1) - F(k, \varphi_2)\big) \,] \end{gathered} \tag{3-13}$$

where H_y and H_x are the vertical and horizontal positions at the end of the beam, $E(k,\varphi)$ is the incomplete integral of the second kind. k, φ_1 and φ_2 can be obtained by using trigonometric identities and boundary conditions.

3.3.2 Finite element modeling

A Chevron-beam structure with fixed-guided boundary condition is modeled using COMSOL Multiphysics® FEM simulations. The dimensions and material properties used in the simulations are given in Table 3.1. Predictions from the analytical solution developed in previous section are compared to the FEM simulations in Fig. 3.5. The two models agree to 98.5%, proving the validity of the analytical model for the whole range of stress. The small disagreement between the two methods stems mainly from the non-incorporation of the axial strain of the beam in the bending model. The mechanical gain and overall device performance can be modified by changing the geometry of the Chevron-beams. As shown in Fig. 3.6, lower angles yield to higher gains but it will lower the range of the measurements. Therefore, the angle of 0.10 rad is selected for our proposed designs. According to the outcome of the analytical solutions shown in Fig. 3.6, increasing beams length also increases the mechanical gain but longer beams will add non-linearity to the bent-beam shape too. Hence, beam length of 260 μm is selected. The width and thickness of the beam also proportionately increase the gain. It should also be noted that since beams thickness and electrodes thickness are equal, higher thickness will result in higher total capacitance of the sensor. However, 3μm is selected in the design because it is an achievable thickness using regular plasma etching machines in a surface micromachining process. Beam's width must be also selected to be smaller than their thickness to avoid buckling up when they are under strained. In addition to altering the Chevron-beam geometry, higher gain can be obtained by creating cascaded structure [45] which is not considered in this work. The obtained result is used to select the optimum geometry and inclination angle for the MEMS sensors that are described in the next section.

Table 3.1: chevron beams FEM simulation physical characteristics

Beam Length	260 μm
Beam Thickness	3 μm
Beam Width	2 μm
Polysilicon Young's Modulus	160 GPa
Polysilicon Poisson's Ratio	0.22

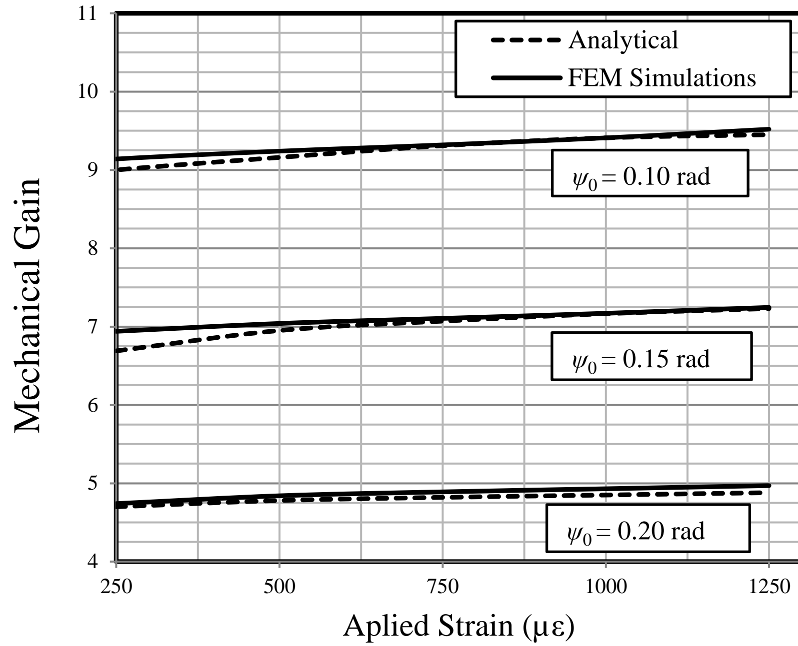

Fig. 3.5: Comparison of mechanical gain obtained analytically and by FEM simulation using COMSOL Multiphysics® at different inclination angles.

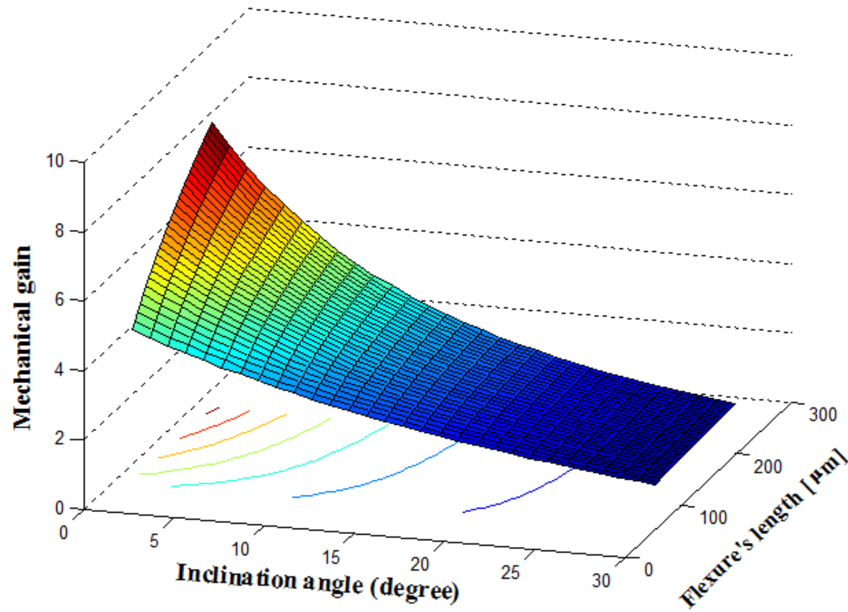

Fig. 3.6: Effect of both bent-beams length and inclination angle on mechanical gain obtained analytically at different points.

3.4 Motion Amplified Capacitive Strain Sensors

The basic topologies of the proposed variable-gap and variable-area comb-drive capacitive sensors are shown in Fig. 3.7 and Fig. 3.8 respectively. The structures have two amplifying bent beams to enhance device sensitivity, with interdigitated comb fingers at the center. Any small displacement caused by external strain is enhanced along the vertical axis and moves the fingers. Result from the FEM simulation of the beams and electrodes displaced from their original positions due to the applied strain is shown in Fig. 3.9. Capacitance change takes place by varying the gap distance in design (a) and overlap area in design (b) between electrodes. Each design has its own advantages. For example, the variable gap design has higher sensitivity but due to the pull-in effect between the plates, it has lower operation dynamic range. On the other hand, the variable area design provides more linearity and higher operating range but less sensitivity. These are discussed in the following sub-sections.

3.4.1 Variable-gap design

As depicted in Fig. 3.7, there are two sets of stationary electrodes forming a set of differential sensing capacitors, $C_1(y)$ and $C_2(y)$. This differential sensing produces a more stable output signal with higher sensitivity. Another advantage is that no absolute capacitance reference is needed and also the output signal would be insensitive to external variations such as circuit and system. The capacitance is approximately,

$$C(y) = N\varepsilon_0 \frac{tL_0}{g \pm y} + C_p \qquad (3\text{-}14)$$

Here, N is number of air gaps, L_0 the overlap between the fixed and moving electrodes, g the air gap between electrodes when $y = 0$, t the electrode thickness, and C_p is the parasitic capacitance. The nonlinear relationship could be a drawback if capacitance is measured directly, but the output would be more linear if capacitance impedance is measured instead. Another drawback with the variable-gap configuration is the limited range of motion, because the structure is prone to pull-in failure. This problem can be easily avoided by predicting mechanical stops that prevent the gap from decreasing below the pull-in spacing. Fig. 3.10 shows a possible sensor chip designs with the interconnections composed of four comb-drive structures to increase the overall sensitivity of the

sensor. Each of the comb-drive structures is designed with 260 μm length, 2 μm width, 3 μm thickness and original inclination angle of 0.10 rad. Finger electrodes are 100 μm long, 4 μm wide and 3 μm thick. The air gap between the finger and fixed electrodes is initially 8 μm.

3.4.2 Variable-area design

Interdigitated electrodes can also have transverse motion which varies the overlap area and keep a constant spacing (Fig. 3.8). In this configuration, motion and capacitance are linearly related and a longer range of motion can be measured. However, the sensitivity is less and the sensor may also show unwanted sensitivity to spacing. A possible sensor chip design with the interconnections composed of four variable-area comb-drives to increase the overall sensitivity is shown in Fig. 3.10. It must be noted that another important consideration in the design of both sensor structures has been easy fabrication by surface micromachining. The thickness of the fingers and electrodes could be higher than 3 μm for higher resolution and sensitivity and can be achieved by deep RIE.

3.5 FEM Simulation Results

The FEM simulation was carried out on single structures of the both the proposed sensors using COMSOL Multiphysics®. The results are shown in Fig. 3.11. The obtained sensitivity, defined as the differential capacitance change per unit input strain, was 13 aF and 2.7 aF per microstrain (με) for the variable-gap and variable-area designs respectively. The maximum strain ranges for the respective designs were ±1000 με and ±1800 με, and the strain measurement resolutions were 82 με/fF and 380 με/fF. For the geometry explained in the previous section the sensors achieve a nominal capacitance of about 25 fF. Despite this seemingly small value, such MEMS devices can operate effectively using circuits with a sensitivity of less than 0.1 fF.

3.6 Resonant Strain Sensor

The resonant frequency (natural frequency) of stress-free structures changes when they undergo compression or tension. This is the basis for the design of resonant sensors such as accelerometers [65], gyroscopes [66] etc. The variable-gap comb drive structure introduced in previous section can also be used as a high resolution resonant strain sensor. When the substrate is subjected to a

strain force, the Chevron-beams undergo tensile or compressive strain and the resonant frequency of the comb drive structure varies. The natural frequency of the comb drive structure is given by:

$$f_n = \frac{1}{2\pi}\sqrt{\frac{k_y}{m_t}} \qquad (3\text{-}15)$$

k_y can be obtained by calculations derived in Section II, by dividing F_y by vertical displacement, H_y. m_t is the total mass given by,

$$m_t = m + 4m_e = m + \frac{52}{35}m_b \qquad (3\text{-}16)$$

Where m is the mass of comb drive, m_e is the effective mas of the Chevron-beam given by m_e = 13/35 m_b [28], with m_b being the mass of the Chevron-beam.

Fig. 3.12 shows the device structure and the shape change on its first mode at 24kHz. FEM simulation was carried out to characterize the strain sensitivity of the resonator structure, and the resonant frequency change rate as a function of applied strain. The result is shown in Fig. 3.13. This structure exhibits a sensitivity of about 8.6 Hz/με, which is quite sensitive for this range of measurement.

3.7 Conclusions

Two new designs of linear and sensitive MEMS strain sensors have been presented. The structures use two pairs of Chevron beams to achieve higher resolution and sensitivity by mechanically amplifying the displacement created by the applied strain. An analytical model has been developed to predict the deflection behavior of Chevron-beams by using elliptic integrals, and its accuracy was verified by FEM simulations which showed excellent agreement. The model can be used as a reliable analysis tool when designing any MEMS structures using Chevron beams and also the solution allows quick optimization of the geometry to achieve best results. The effects of inclination angle of the beams were studied for designing structures with highest mechanical gain. FEM analysis of the comb-drive based designs of variable-gap and variable-area sensor structures showed a capability of measuring strain with resolution of 82 με/fF and 380 με/fF, while demonstrating a maximum strain range of ±1000 με and ±1800 με, respectively.

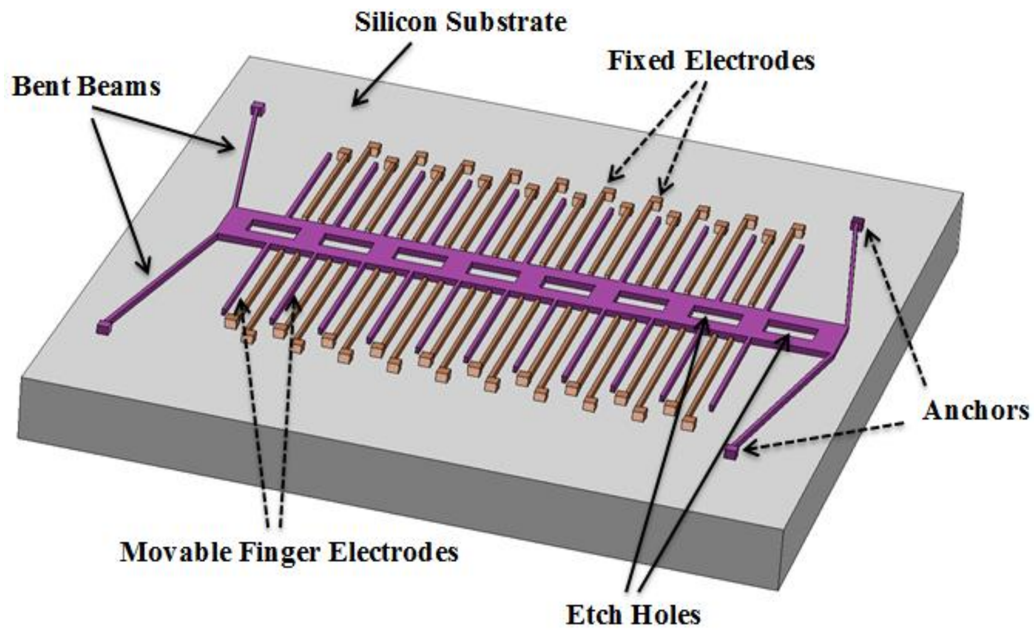

Fig. 3.7: Variable-gap comb-drive capacitive sensor consisting of interdigitated fixed and movable electrodes. The movable electrodes are attached to the displacement amplification microdevice.

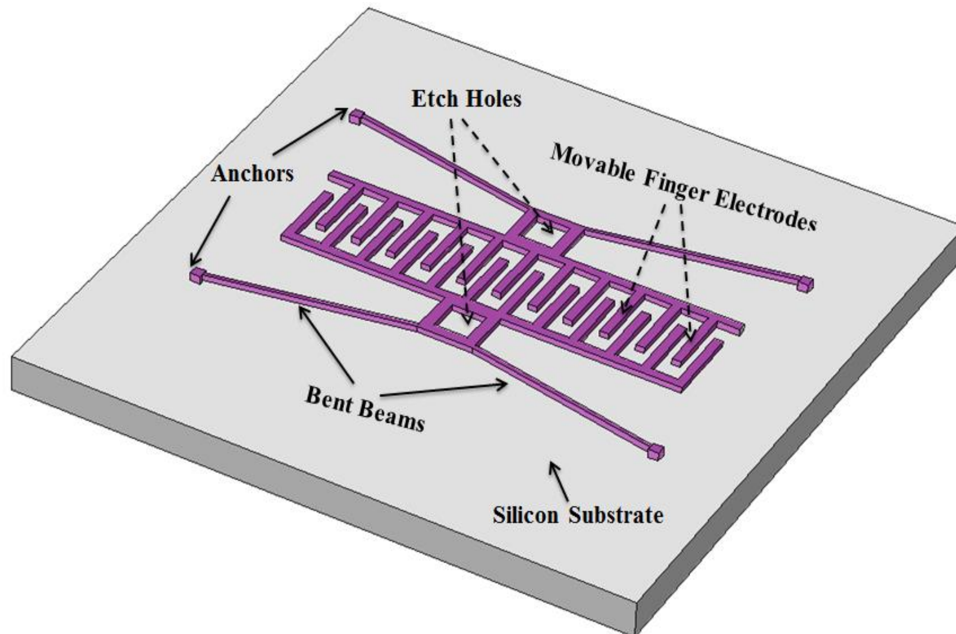

Fig. 3.8: Variable-area comb-drive capacitive sensor consisting of interdigitated movable electrodes. Electrodes are attached to the displacement amplification microdevice with four Chevron-beams which moves in the y direction when the substrate is strained.

COMSOL MULTIPHYSICS®

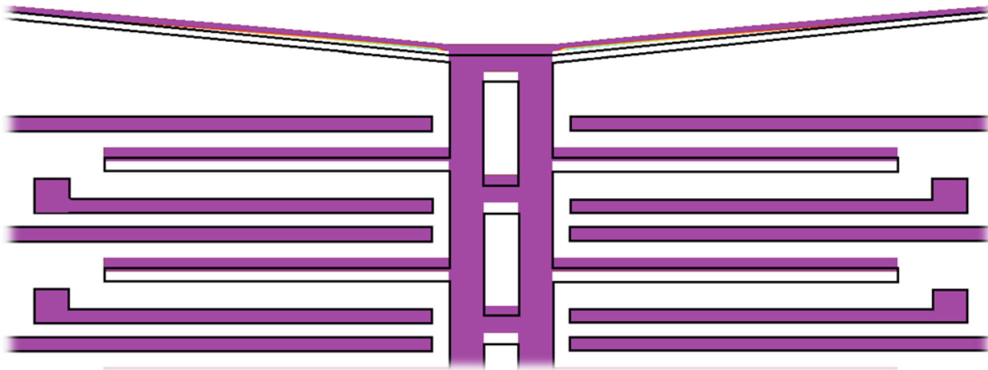

Fig. 3.9: A zoom view showing electrodes displaced from their original positions due to the applied strain.

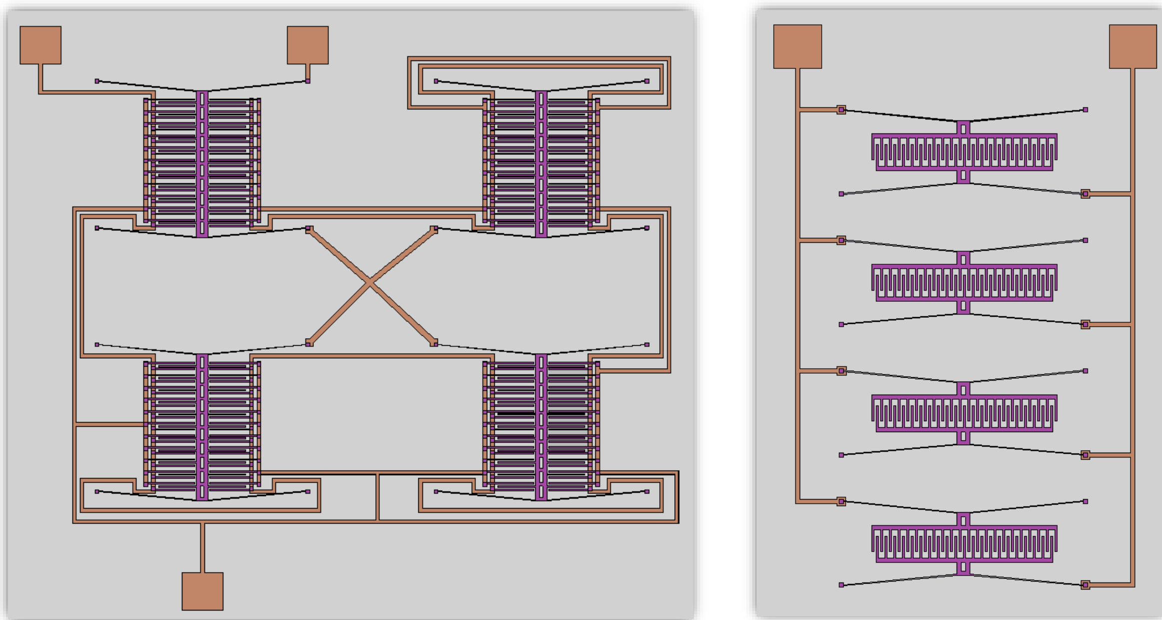

Fig. 3.10: Complete design of the variable-gap and variable-area design sensors simulated in COMSOL Multiphysics® with the mechanical and electrical interconnections between four comb-drive structures.

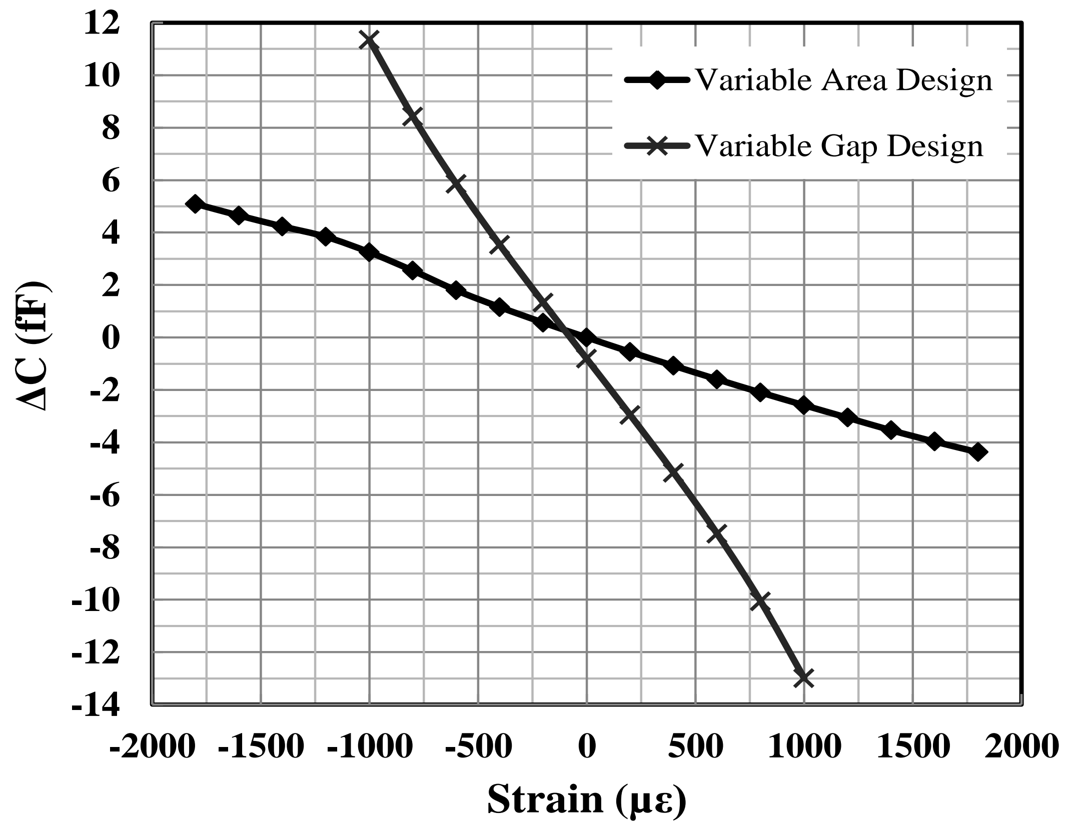

Fig. 3.11: Simulation results of the MEMS strain sensors performance characteristics. As it can be seen in the graph, the variable-gap design shows higher sensitivity but less operation range. On the other hand, the variable-area design is less sensitive but with higher range.

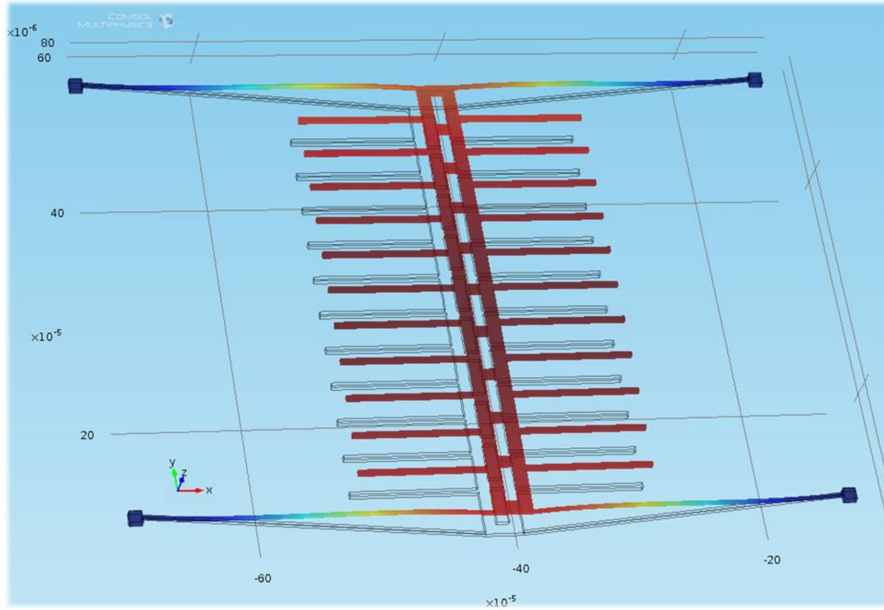

Fig. 3.12: Device structure and its shape change on its first mode at 24kHz.

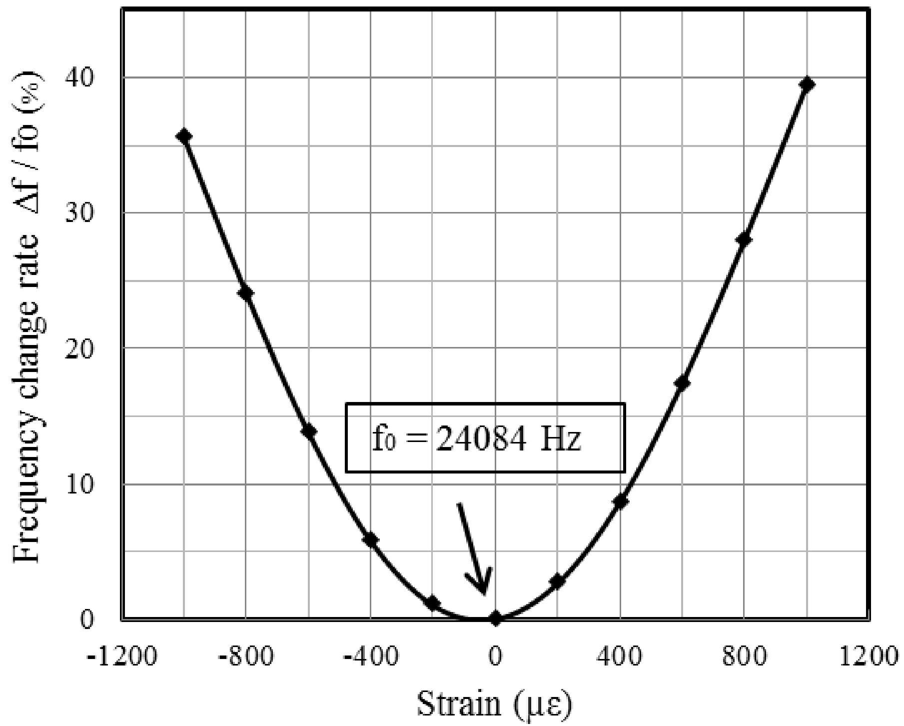

Fig. 3.13: The COMSOL Multiphysics® FEM simulation result showing the resonant frequency change rate for the applied strains. This structure exhibits a sensitivity of about 8.6 Hz/με.

4. Modeling and Analysis of Strain Transfer of the Designed MEMS Sensors*

4.1 Introduction

Strain is an important parameter in structural health monitoring (SHM) of mechanical systems. High and/or lasting strain can lead to crack formation, yielding, or fatigue in the structure material. Strain measurement systems with high sensitivity are desirable for early failure prediction and preventive maintenance. Piezoresistive [67], piezoelectric [68], inductive [69], and fiber Bragg grating (FBG) [70] sensors have been used for strain gauges. While there is a need to overcome some uncertainties associated with conventional strain gauges [71], it is also desirable to have compact sensing devices with lower power consumption, more capabilities, and compatibility to digital circuit integration. Sensors and devices entirely based on microelectromechanical systems (MEMS) are receiving serious consideration due to their miniaturization, low power, stability, high performance and accuracy [72], [73], [53]. The high potential of MEMS sensors for CMOS integration is an added advantage.

With the sensors becoming more miniaturized and high in accuracy, the properties of the medium that bonds the sensor to the host structure (e.g. wind turbine blade) become critical. The comprehensive sensor design should also include the bonding layers, taking into account their geometric dimensions and mechanical properties such as Young's modulus, Poisson's ratio, strain distribution etc., in order to understand the strain transmission mechanism and finally achieve a near-unity strain transfer ratio.

---

* Based on a published manuscript: M. Moradi and S. Sivoththaman, "Strain transfer analysis of surface-bonded MEMS strain sensors," *IEEE Sensors Journal*, vol. 13, no. 2, Jan 2013.

Previous studies on bonded strain sensors include modeling the sensing and actuation of a beam by adhesively bonded piezoelectric patches [74], [43], and investigation of strain transfer mechanism of FBG sensors bonded to substrates using adhesive layer [75]. The studies showed that the strain transfer from the host structure to the bonded sensor depends on the adhesive layer and adherend properties. In practice, the strain measured by the sensor must be corrected by a factor to reflect the original strain of the host structure. To be able to accurately model the strain transfer the mechanics dictating the stress and strain within the bonded joint must be understood.

Adhesive joints are three-dimensional structures in reality, but 3D solutions are difficult when using analytical approaches and computationally intensive when using numerical solution methods. However, many adhesive bond problems can be reasonably treated 2D or even 1D, by proper model theories. Considering the relative deformation parallel to the bond plane, the shear lag theory [76] can be used for the 1D treatment. The term "shear lag" dates back to bending analysis of "I" and "T" beams with wide flanges [77]. According to Beam Theory, the axial displacements in the flange are a function of the distance from the neutral axis and independent of the distance from the web, and the shear stress and strain of the flange is also zero. However, in reality, the axial displacements lag behind the beam theory prediction because of the load diffusion due to non-zero shear stresses in the flange. The shear lag method, first presented by Cox [78] and Volkersen [79], and modified later by others [80], [81], is the fundamental concept about load transfer between two members joined by a continuous adhesive layer.

In this work, the shear lag theory is shown to adequately predict the stress transfer between the sensor and the host structure for MEMS strain sensors. Consideration is given to the load transfer from one adherend to another through an adhesive medium. First, a realistic and accurate analytical model is proposed for a MEMS strain sensor fabricated on a silicon substrate attached to a host structure using an adhesive layer, with the host structure subjected to a uniform axial stress. The model is also applicable for bonding piezoelectric patches and FBGs. Second, the model prediction is validated by using finite element method (FEM) simulations. Third, the effects of adhesive layer, substrate geometry, and mechanical properties on sensor gauge factor are investigated. Finally, some techniques for improving the strain transfer are proposed based on the modeling results. The presented analysis can also be used to calibrate strain sensors.

4.2 Strain Analysis and Model Development

Consider a silicon MEMS strain sensor chip of thickness δ_1 and Young's modulus E_1 bonded to the surface of a host structure with thickness δ_2 and Young's modulus E_2, using an adhesive layer with thickness δ_3 and Young's modulus E_3 as shown in Fig. 4.1. The load is transferred through the adhesive layer by shear stresses distributed along the bond.

Fig. 4.2 shows the displacement equilibrium diagram of the structure. The shear lag analysis used to determine the stress distributions is based on the following assumptions: (i) the shear modulus of the adherend is much greater than that of the adhesive, so the adherend does not deform in shear; (ii) out-of-plane normal stresses are ignored in both the adhesive and adherend; (iii) the effect of the load coupling and bending of the adherend is ignored; (iv) adhesive and adherend are linearly elastic; (v) interfaces at both bond planes are free of strain discontinuities; (vi) the effect of coefficient of thermal expansion (CTE) mismatch is ignored; and, (vii) effects of different Poisson contractions in the bonded regions are ignored. The governing equations are derived for the 1D case with a bonding layer of total length l. The displacements of the upper and lower adherends are represented by U, the axial and shear stresses by σ and τ, and the axial and shear strain on the layers by ε and γ respectively.

This model can be easily extended to 2D by considering the Poisson effect. However, since motion in y direction due to any transverse strain will not considerably affect the strain in the x direction, it is neglected without much error. Moreover, the finite element analysis which is explained later takes into account the strain three dimensionally. Based on the 1D constitutive Hooke's law, the strain-stress relationships are:

$$\sigma_1 = E_1 \varepsilon_1 \quad (4\text{-}1)$$

$$\tau = G_3 \gamma \quad (4\text{-}2)$$

$$\sigma_2 = E_2 \varepsilon_2 \quad (4\text{-}3)$$

where E_1 and E_2 are the Young's moduli of sensor substrate and the host structure respectively and $G_3 = E_3/[2(1 + v_3)]$ is the shear modulus and v_3 is also the Poisson's ratio of the adhesive layer. From compatibility and equilibrium considerations in x direction pertaining to the adhesive layer of Fig. 4.2, we have:

$$\frac{\delta_3 \partial \gamma_{3x}}{\partial x} + \frac{\partial U_{1x}}{\partial x} + \frac{\partial U_{2x}}{\partial x} = \varepsilon_{2x} - \varepsilon_{1x} \tag{4-4}$$

$$\frac{\delta_1 \partial \sigma_{1x}}{\partial x} = -\tau_{3x} \tag{4-5}$$

$$\frac{\delta_2 \partial \sigma_{2x}}{\partial x} = \tau_{3x} \tag{4-6}$$

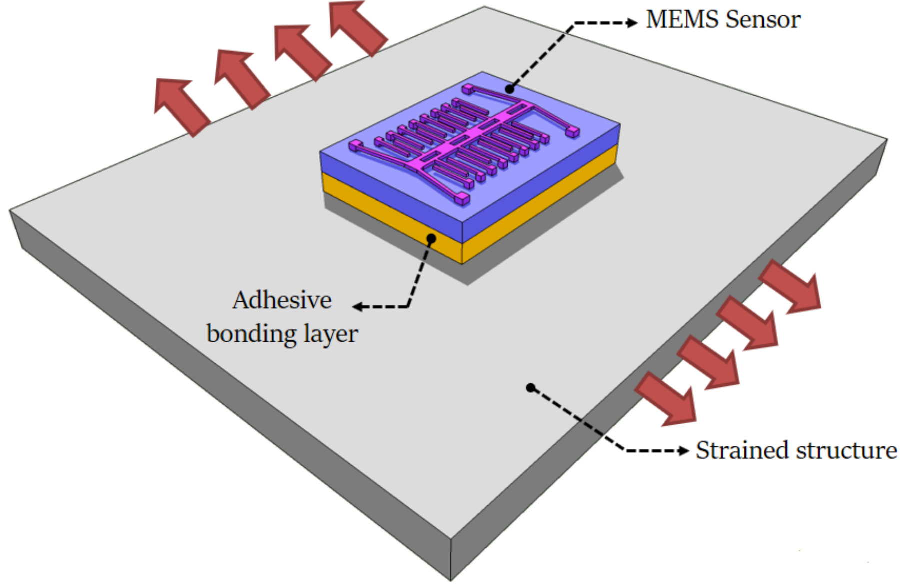

Fig. 4.1: 3D schematic of the strained host structure, bonding layer and the sensor substrate.

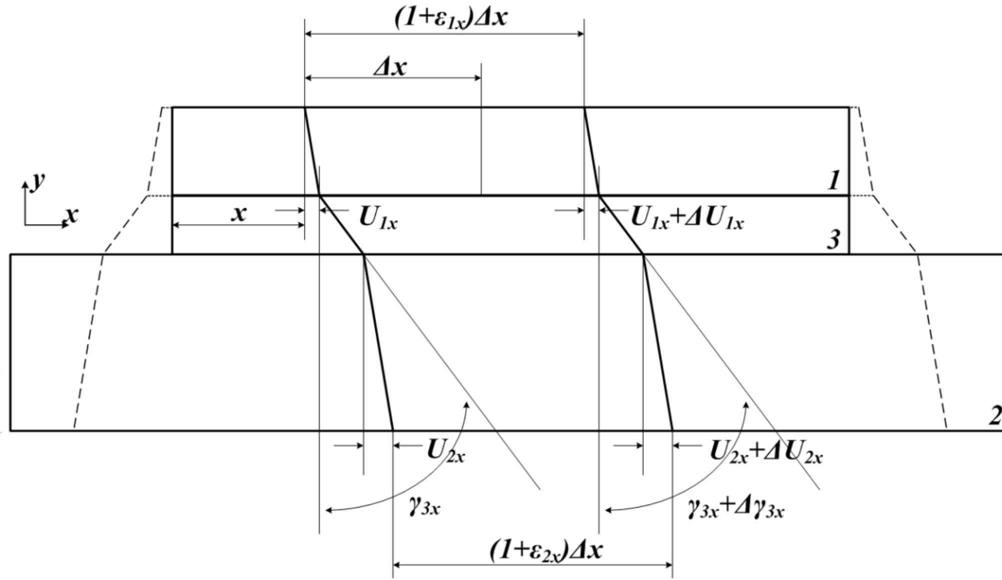

Fig. 4.2: Displacement equilibrium diagram of the investigated adhesive bonded structure.

The shear displacements of the adherends, U_{1x} and U_{2x}, can be found using the method of Adams and Peppiatt [80]:

$$\tau_{1x} = \tau_{3x}\left(1 - \frac{y}{\delta_1}\right) \tag{4-7}$$

$$\tau_{2x} = \tau_{3x}\left(1 - \frac{y}{\delta_2}\right) \tag{4-8}$$

Thus:

$$U_{1x} = \frac{\tau_{3x}\delta_1}{2G_1}\ , \qquad U_{2x} = \frac{\tau_{3x}\delta_2}{2G_2} \tag{4-9}$$

By substituting equations (4-5) up to (4-9) in Eq. (4-4), differentiating, and ignoring the transverse and residual stresses, one gets the following governing differential equations:

$$\frac{\partial^2 \tau_{3x}}{\partial x^2} - \Gamma^2 \tau_{3x} = 0 \tag{4-10}$$

$$\frac{\partial^3 \varepsilon_{1x}}{\partial x^3} - \Gamma^2 \frac{\partial \varepsilon_{1x}}{\partial x} = 0 \tag{4-11}$$

$$\frac{\partial^3 \varepsilon_{2x}}{\partial x^3} - \Gamma^2 \frac{\partial \varepsilon_{2x}}{\partial x} = 0 \tag{4-12}$$

where Γ is,

$$\Gamma^2 = \frac{\frac{1}{E_1\delta_1} + \frac{1}{E_2\delta_2}}{\frac{\delta_1}{2G_1} + \frac{\delta_2}{2G_2} + \frac{\delta_3}{G_3}} \tag{4-13}$$

The general solutions to above second-order differential equations take the following forms:

$$\tau_{3x} = A cosh\Gamma x + B sinh\Gamma x \tag{4-14}$$

$$\varepsilon_{1x} = A' cosh\Gamma x + B' sinh\Gamma x + C' \tag{4-15}$$

$$\varepsilon_{2x} = A'' cosh\Gamma x + B'' sinh\Gamma x + C'' \tag{4-16}$$

The unknown coefficients of the general solutions are obtained by applying the boundary conditions at $x = 0$ and at $x = l$. Assuming a uniform strain of ε_0 on the host structure with no sensors bonded, one gets:

$$A'' = \frac{\varepsilon_0}{1 + \frac{E_2\delta_2}{E_1\delta_1}}, \ B'' = A''\frac{1 - cosh\Gamma l}{sinh\Gamma l}, \ \ C'' = \varepsilon_0 - A'' \qquad (4\text{-}17)$$

$$A' = A'' - \varepsilon_0, \ B' = A'\frac{1 - cosh\Gamma l}{sinh\Gamma l}, \ \ C' = A' \qquad (4\text{-}18)$$

$$A = A'\delta_1 E_1 \Gamma \frac{sinh\frac{\Gamma l}{2}}{cosh\frac{\Gamma l}{2}} \ , \qquad B = -A\frac{cosh\frac{\Gamma l}{2}}{sinh\frac{\Gamma l}{2}} \qquad (4\text{-}19)$$

From the above governing equations, we observe that the strain sensed by the sensor is different from that on the host structure. The difference, due to the shear lag effect, depends on geometry of the bonding structure and Young's moduli. The parameter Γ (m^{-1}) is the "shear lag parameter".

For different values of the shear lag parameter, the strain distributions have been computed using the properties listed in Table 4.1. Fig. 4.3 shows the strain distribution on the sensor substrate (ε_1) for different values of Γ. The maximum strain transfer occurs at the midpoint, indicating that the MEMS sensor element must be placed at the middle of the substrate. Fig. 4.4 shows the strain distribution of the host structure (ε_2) along the bonding layer for different values of Γ. It is observed that the original strain distribution on the host structure is altered in proximity of the bonding area. As much as this strain distribution differs from ε_0, the strain transferred to the sensing element will deviate from the actual strain experienced by the host structure. The results demonstrate that the ratio of transferred strain to the sensor substrate decreases at lower Γ values. Moreover, we observe that higher values of Γ are desirable to achieve a perfect bonding and that the amount of the strain transfer and the uniformity in strain distribution are substantially reduced at lower values of Γ, which Γ is defined by the geometry and material properties of the bonding elements (Eq. (4-13)). The strain transmission can be quantified by defining a transmission ratio or gauge factor (α), as the ratio of maximum sensor substrate strain (at midpoint, $x = l/2$) to the actual host structure strain (ε_0):

$$\alpha = \frac{\varepsilon_{1x}(x = l/2)}{\varepsilon_0} \qquad (6\text{-}20)$$

The strain transmission ratio obtained from Eq. (4-20) can be used for calibration of a bonded

sensor. The effects of the bonding layer properties and MEMS sensor substrate on the gauge factor are discussed in detail in section 4.4.

Table 4.1: Dimensions and mechanical properties used in the analytical solution and finite element analysis [82], [83].

Symbol	Quantity	Value
E_1	Young's modulus of the sensor substrate	170 GPa
E_2	Young's modulus of the host structure	170 GPa
E_3	Young's modulus of the adhesive layer	3.3 GPa
υ_1	Poisson's ratio of the sensor substrate	0.28
υ_2	Poisson's ratio of the host structure	0.20
υ_3	Poisson's ratio of the adhesive layer	0.20
δ_1	Sensor substrate thickness	400 μm
δ_2	Host structure thickness	5000 μm
δ_3	Adhesive layer thickness	100 μm
ε_0	Strain applied on the host structure	1000 με

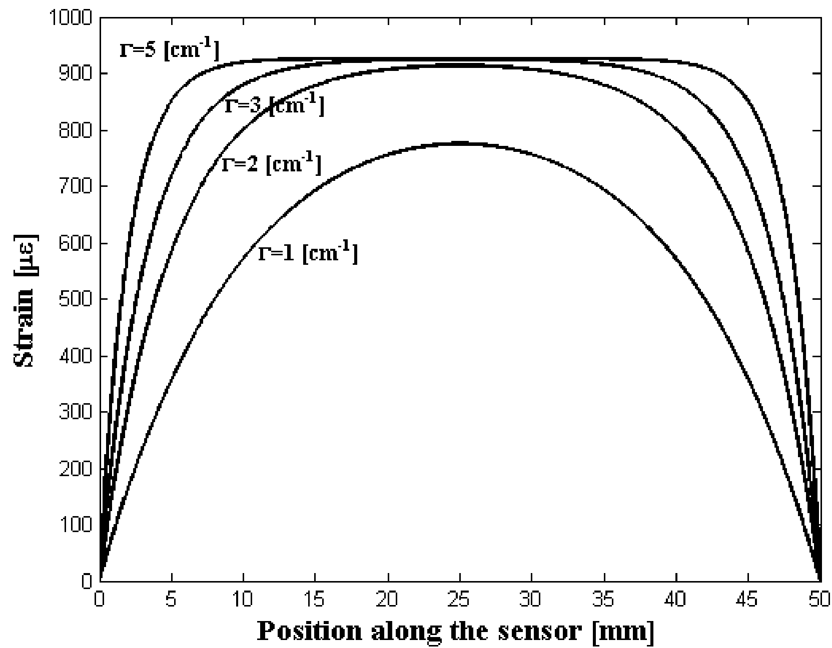

Fig. 4.3: Strain distribution in the sensor substrate along the length of the bonding layer for various values of Γ.

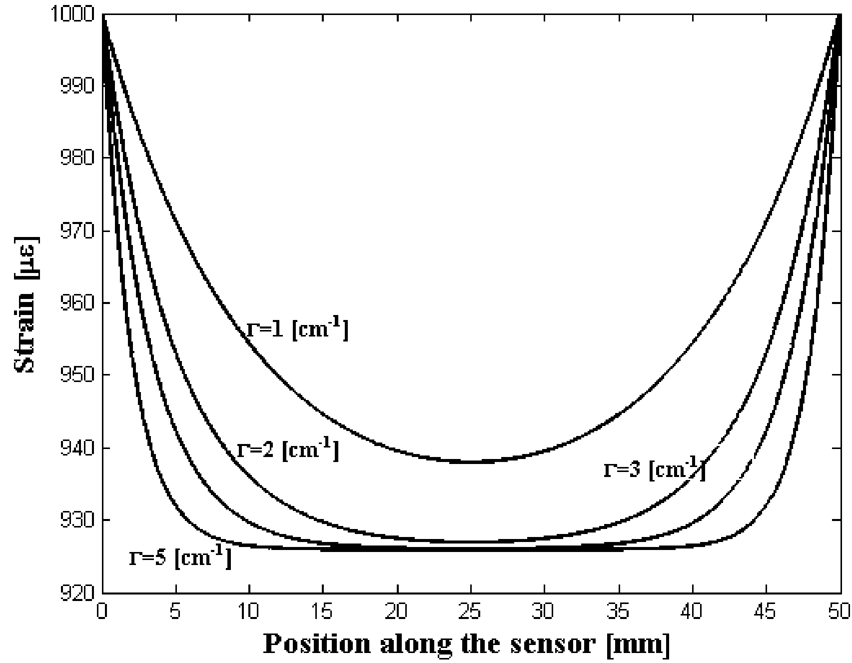

Fig. 4.4: Strain distribution of the host structure along the length of the bonding layer for various values of Γ.

4.3 Finite Element Analysis

In this section, finite element method (FEM) simulation using COMSOL Multiphysics® is carried out to validate the proposed analytical model. The FEM simulation yields a 3D numerical solution somewhat relieved from the limitation of the aforementioned assumptions. Fig. 4.5 shows the 3D elemental model and the mesh construction used in the FEM analysis. The parameters used for the FEM simulation were exactly the same as those listed in Table I and are edited in the COMSOL material library.

A good agreement between the analytical solution and the FEM simulation is obtained as shown in Fig. 4.6 and Fig. 4.7. Strain distributions in the host structure and the sensor substrate obtained by FEM simulations and the analytical solutions are shown in Fig. 4.6. The small discrepancies between the two methods could be attributed to the simplifying assumptions explained in section 4.2. The little drop in the upper right side of the figure is due to using reduced mesh density at the extremity of the structure in the finite element model to reduce the computing time. Shear stress distribution in the adhesive layer obtained by finite element analysis and

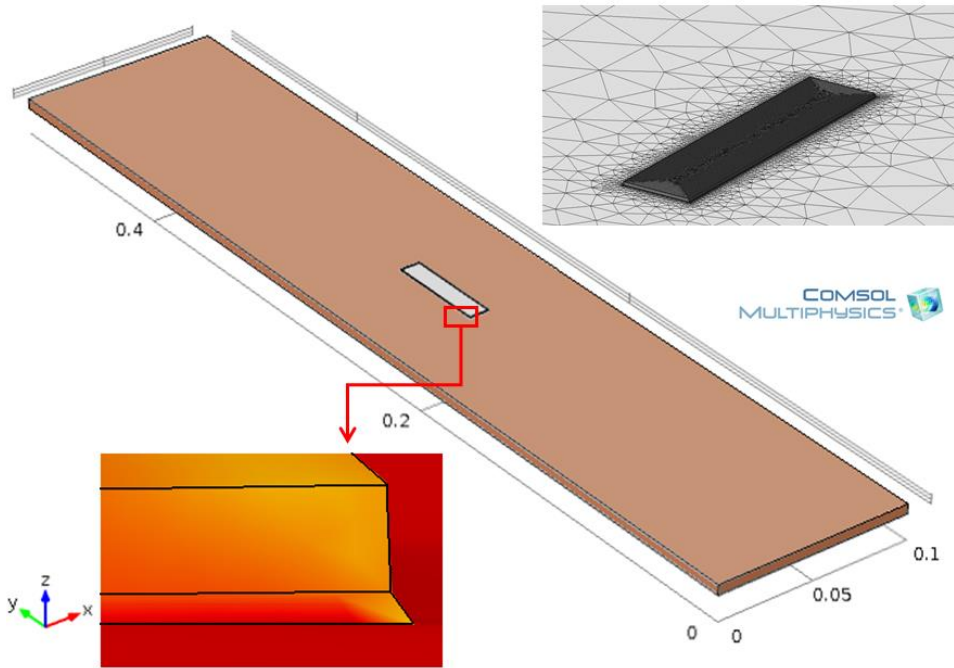

Fig. 4.5: Finite element model of the investigated adhesive bonded structure. Bottom left inset is showing that how the strain from the host structure surface causes deformation of adhesive layer and consequently sensor's silicon substrate. Top right inset is showing the constructed mesh for the finite element simulation.

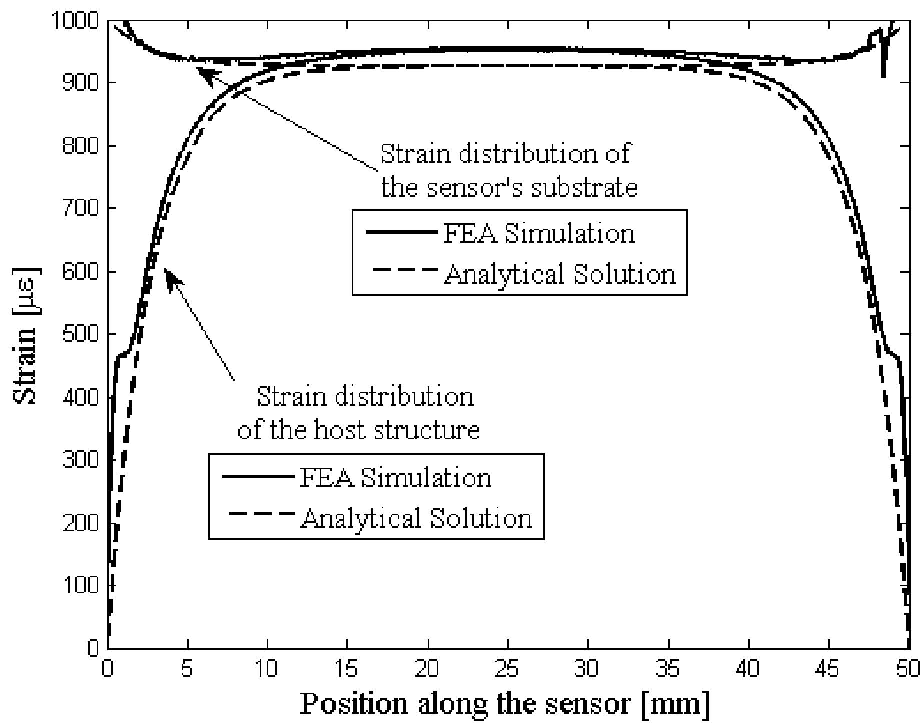

Fig. 4.6: The close agreement of the FEA simulation results and the analytical solutions.

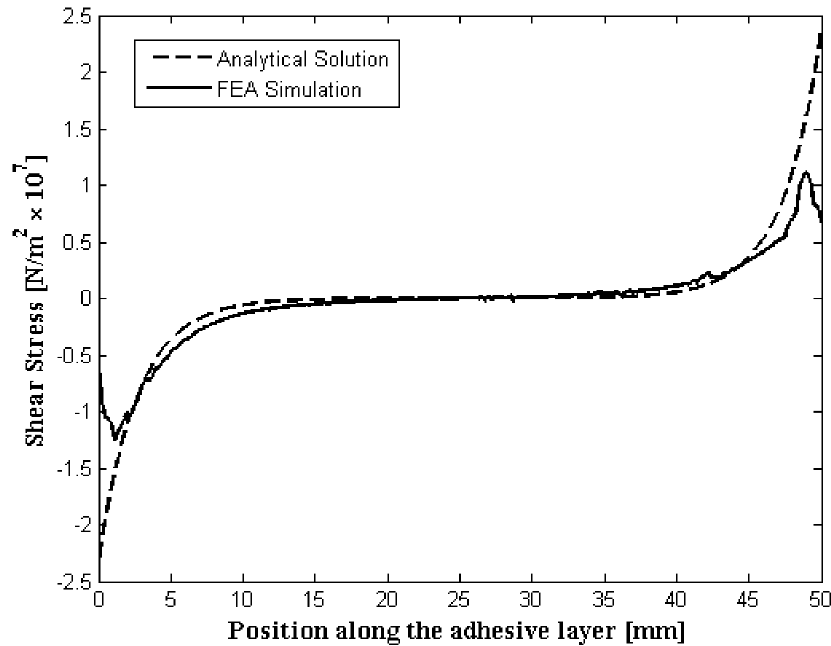

Fig. 4.7: Shear stress distribution in the adhesive layer.

analytical solution is also shown in Fig. 4.7. A relatively uniform shear stress distribution is observed with no shear stress in the midpoint due to the symmetric nature of the structure. Peaks appear in the shear stress wherever there are relative changes in the stiffness of the adherends. Thus near joint ends, large shear stress peaks are to be expected. It is interesting to note that there is a downturn at the shear stress graph in the FEM result at the two ends. This effect can be attributed to the fact that the transverse strain [84] was neglected in the analytical model.

4.4 Results and Discussions

4.4.1 Effects of adhesive layer's geometry and mechanical properties

The variation of the sensor gauge factor (α) with adhesive layer thickness for different values of sensor length is shown in Fig. 4.8. It is observed that thinner adhesive layers lead to higher α. The figure demonstrates that α is sensitive to adhesive layer thickness for smaller sensor substrate lengths, but this sensitivity almost drops for larger sensor lengths, above 50mm in this case. Fig. 4.9 describes the variation of the gauge factor (α) for different Young's moduli and thicknesses of

the adhesive layer (δ_3). It shows that higher α values are achievable by employing adhesive materials with higher moduli. The dependence on Young's modulus variation is substantial for thicker bonding layers, above 100 μm in this case. The results from Fig. 4.8 and Fig. 4.9 indicate thinner and stiffer adhesive layers as well as having longer sensor substrates are desirable to achieve higher sensor gauge factors.

4.4.2 Effects of sensor substrate

Fig. 4.10 depicts the simulation results describing the effect of sensor substrate thickness and also its Young's modulus on sensor gauge factor for two different sensor lengths. The gauge factor decreases when the substrate gets thicker and when higher modulus materials are used. Moreover, it was also observed that the gauge factor is more sensitive to the adhesive layer properties when the sensor is fabricated using a stiffer substrate. However, MEMS fabrication restrictions on the substrate type, thickness, and flexibility limit the ability to choose these parameters based on the gauge factor analysis alone.

4.5 Strain Transmission Enhancement

The FEA simulation results that are discussed above can be exploited to enhance the strain transmission ratio by introducing non-planar geometric features in the design of bonding structure. First, since the shear stress is reduced near the side ends of the substrate, we find that by tapering the substrate on the sides better strain uniformity can be achieved. Fig. 4.11 illustrates the improvement in strain uniformity with the tapered design. While this might be subject to fabrication constraints it is still an interesting consideration. We have also analyzed two proposed architectures, shown in Fig. 4.12 and Fig. 4.13, with etched surface trenches on the silicon chip around the MEMS sensor element to maximize the strain transfer. The result of the FEA simulations of the proposed structures demonstrate a strain transfer enhancement of up to 30% compared to the flat chip reference model. However, packaging and mounting challenge will need to be addressed in the case of trench-etched substrate (Fig. 4.12).

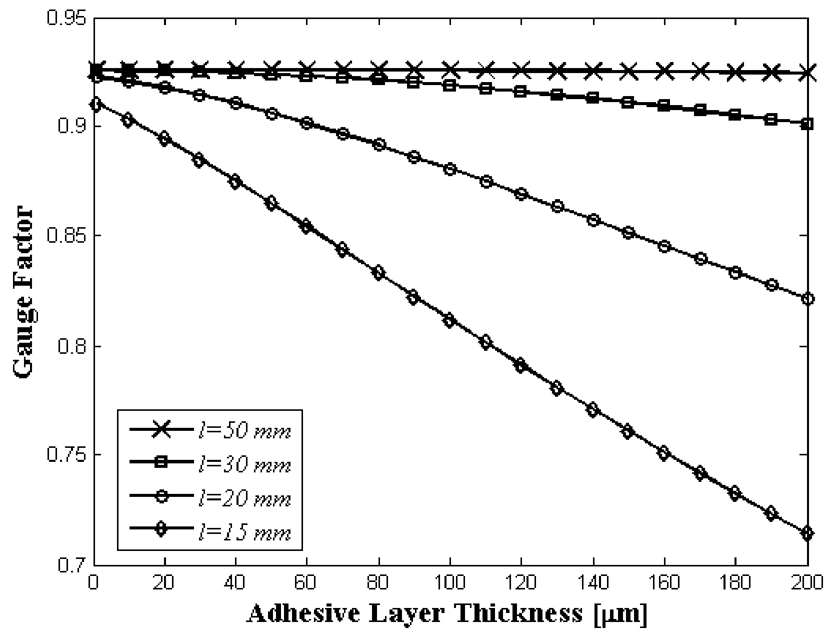

Fig. 4.8: Simulation results describing the influence of adhesive layer thickness on sensor gauge factor at different values of sensor length.

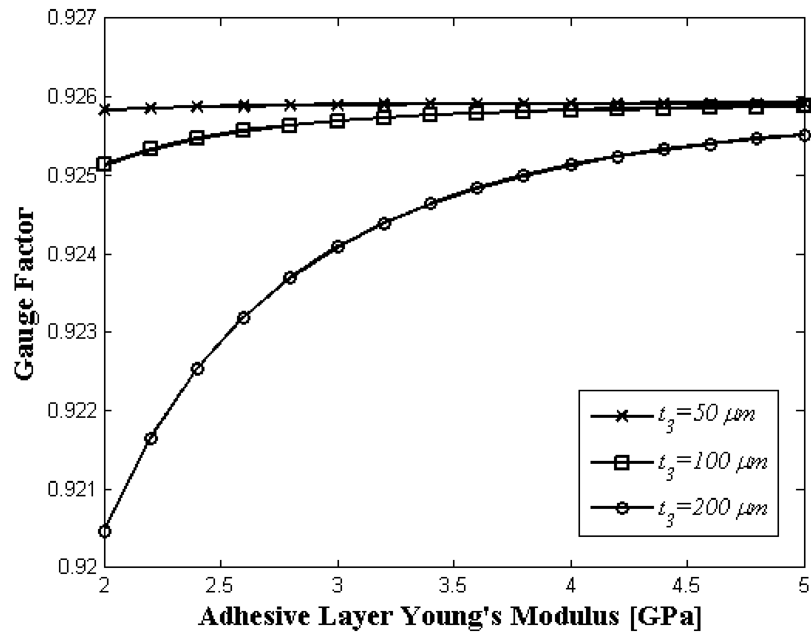

Fig. 4.9: Simulation results describing the effect of mechanical properties (Young's Modulus) of the bonding adhesive layer on sensor gauge factor at different values of thicknesses.

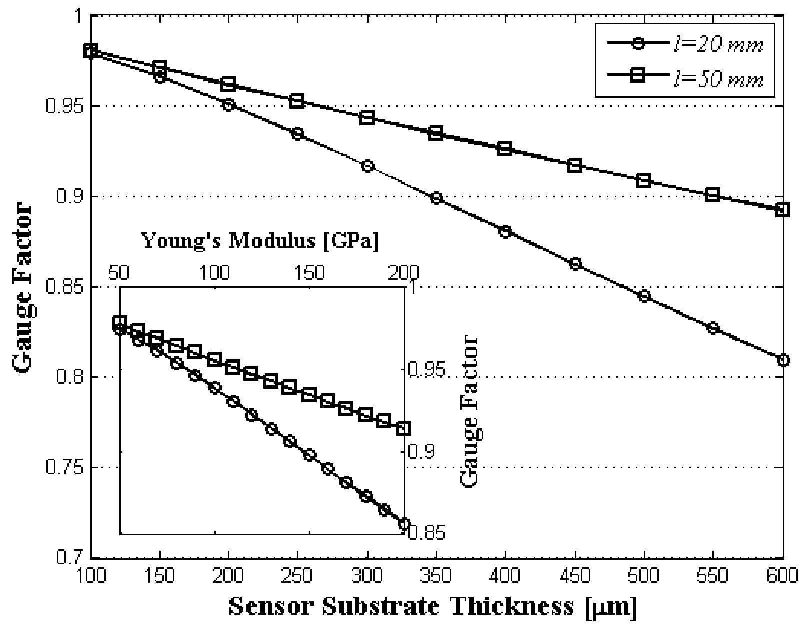

Fig. 4.10: : Simulation results describing the effect of sensor substrate thickness and also its mechanical properties (Young's Modulus) on sensor gauge factor at different values of sensor length.

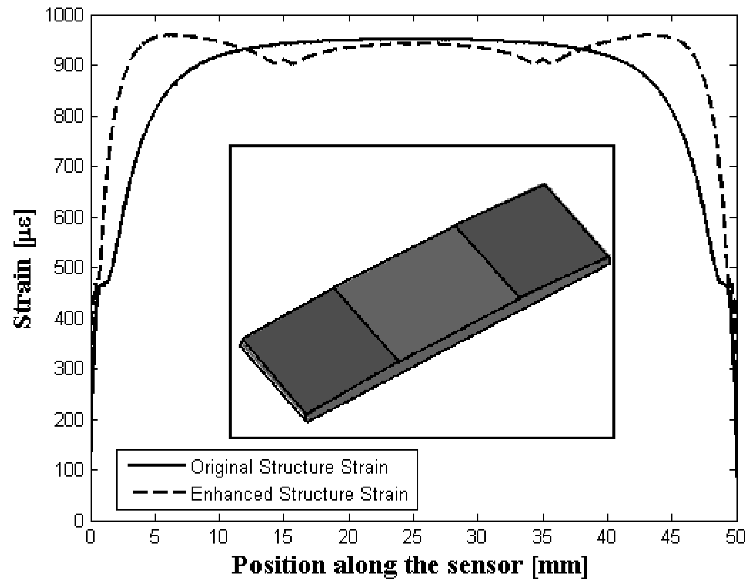

Fig. 4.11: Tapered structure to achieve higher uniformity. The dashed line displays the strain distribution of the substrate. The increase in uniformity is discernible comparing to the original strain distribution (solid line).

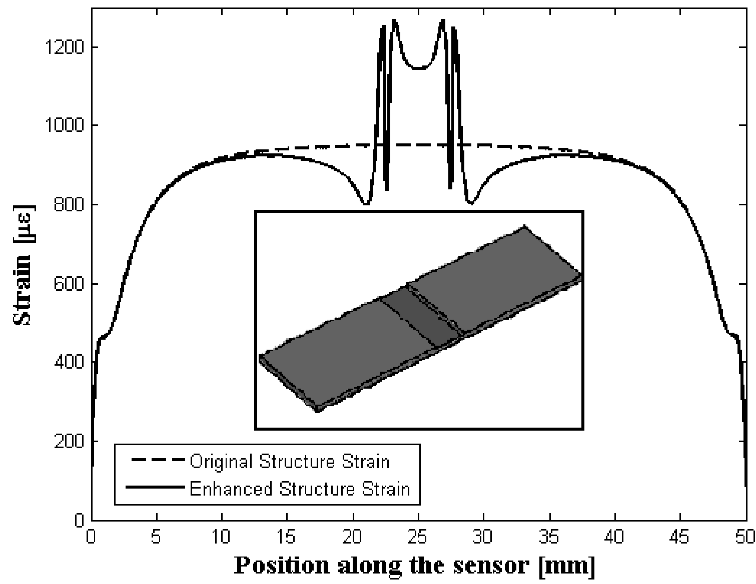

Fig. 4.12: Etched surface trench on the silicon chip is made where the sensing MEMS element is going to be placed. This technique enhances the transferred strain up to 30%.

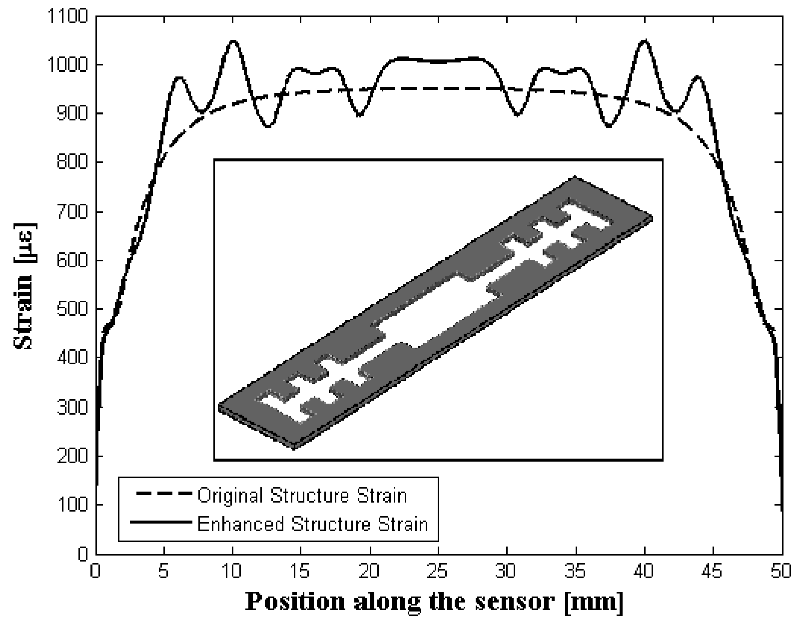

Fig. 4.13: Another proposed model with geometrical features in substrate to enhance the strain transmission ratio. The complete etched away feature reduces the stiffness of the substrate and increases the overall gauge factor.

4.6 Conclusions

In this chapter, a simple formulation is proposed for determining the transmission of strain fields from the host structure to the bonded strain sensor. A verified with FEM analytical model was created to quantify the strain transmission loss due to the interfacial adhesive layer. The model solves the governing differential equations and introduces a shear-lag parameter including the effects of geometry and properties of the components. The solution quantifies the influence of the material parameters on the overall strain transmission ratio and can be used for calibration and evaluation of the sensors even at the design level. The sensitivity of the gauge factor on the adhesive layer thickness has been established, and it is found that smaller sensor dimensions (< 50mm in the study case) lead to increased sensitivity. Flexibility and thickness effects of the sensor substrate have also been studied. Finally, strain transmission enhancement techniques are proposed by introduction of geometrical features to the substrate by tapered edges and trench etching. It is found that the latter technique enhances the strain transfer by up to 30%.

5. Material and Technology Development for MEMS Sensor Fabrication

5.1 Introduction

Integrated circuit (IC) is a mature technology for fabrication and has been the basis for steady advances in MEMS fabrication, and microfabrication process technology has been inherited from that. In this chapter, basic fabrication steps required to realize the comb-drive structures, proposed in the previous chapter, are described. This chapter begins with explaining the materials and then the layers deposition processes and conditions, patterning and photolithography, and finally annealing and releasing the structure.

5.2 Process Design and Material Selections

Material selection is a critical part of the design. The criteria used for the choice of materials were mechanical properties, electrical properties, material availability and fabrication ease. There are three important classes of materials in MEMS fabrication, Dielectric layers, Polycrystalline silicon (Polysilicon), and Metal films. The dielectric layers include silicon dioxide (SiO_2) and silicon nitride (Si_3N_4). These dielectrics are mostly used as a sacrificial layer, insulation between conducting layer, or as a hard mask. Although, SiO_2 is the most common sacrificial material when polysilicon is the structural layer, but silicon nitride is used in this research work for the sake of fabrication ease and our lab gas pipelines availability. Polysilicon is often used as the conductive structural material in MEMS. It is the most popular materials for this purpose due to relatively simple fabrication methods. The technology described in this thesis is based on low-pressure chemical vapor deposited polycrystalline silicon as the preferred mechanical material in the

MEMS sensor due to its compatibility with standard planar integrated circuit processing, desirable mechanical properties, and controllable residual stress and resistivity. Metal films are used to form low resistance connection pads in this work. Traditionally silicon is mostly used as the substrate for MEMS devices. Therefore, 4-inch silicon wafers are used in this research work as the substrate of the MEMS sensor devices. However, for more efficient transfer of strain and other mechanical properties from the host structure a wide range of polymers can also be used as a flexible substrate, such as Parylene, PDMS, Polyimide and etc.

An important aspect to be considered is the selection of fabrication processes among large variety of MEMS processes available. There are several criteria that should be applied in this selection. For example, the compatibility of the process with previous and post processes. There are practical constraints too that are imposed when selection the processes such as their availability in the lab. Fig. 5.1 shows the process flow and fabrication steps for realization of the proposed MEMS structures.

Fabrication process starts with a silicon wafer which is a substrate on which the MEMS elements are built. Preparation of the wafers is required and is usually performed by an RCA cleaning process. Then, it follows by four categories of steps: the deposition of layers of materials, patterning the films by photolithography, selective etching of the films, and finally releasing the structure. This process has the general features of a standard surface micromachining process. First layer is silicon nitride 1 which is used as electrical isolation between the polysilicon and the substrate. The deposition condition of this layer is carefully selected to suit for an acceptable isolation layer. Second layer is polysilicon 1 which is used as the interconnection layer. Third layer is silicon nitride 2 which is used as the sacrificial layer, and again the properties of this layer is carefully selected to suit best for a good sacrificial layer. Forth layer is polysilicon 2 which is used as the structural material and fifth and last layer is the metal for the contacts. It must be noted that the process is different from most customized surface micromachining processes in that it is designed to be as general as possible, and to be capable of supporting many different designs on a single silicon wafer.

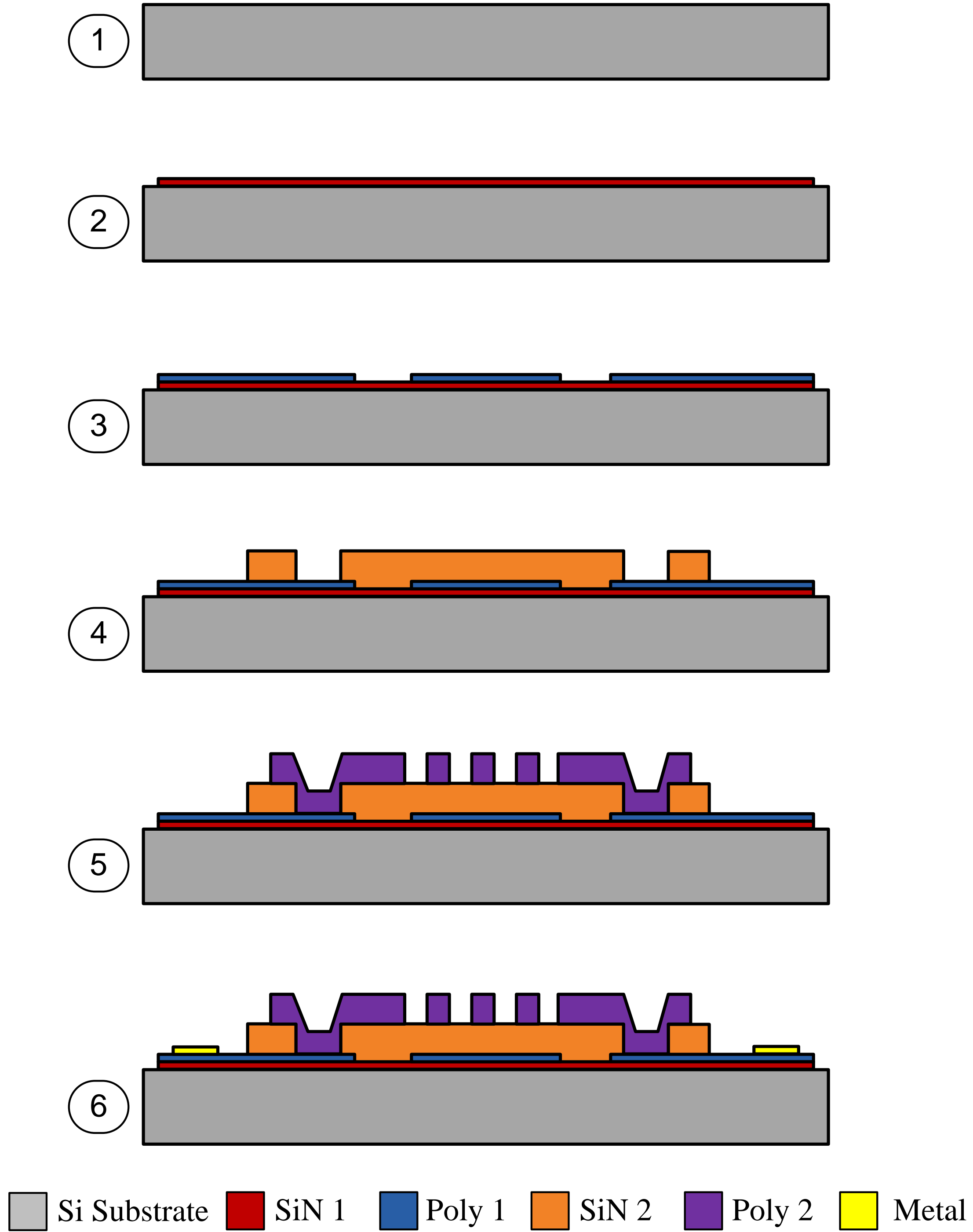

Fig. 5.1: Cross sectional view showing all 5 layers of the process flow (not to scale).

5.3 Process Development of PECVD Silicon Nitride

5.3.1 Introduction

Silicon nitride (Si_xN_y) is a commonly used material in microelectromechanical systems (MEMS) and integrated circuits (IC) fabrications. It has several advantages in chemical, electrical, mechanical, and optical properties. Silicon nitride is deposited by different chemical vapor deposition (CVD) techniques but usually by low-pressure chemical vapor deposition (LPCVD) [85] and plasma enhanced chemical vapor deposition (PECVD) [86]. In LPCVD, nitride is often deposited from dichlorosilane ($SiCl_2H_2$) or silane (SiH_4), and ammonia (NH_3) in temperatures around 800°C. The stoichiometry of the resulting nitride can be changed toward a silicon-rich composition by increasing silane or dichlorosilane flow rate compared with ammonia [87–93]. In PECVD, silicon nitride films are deposited by reacting silane and ammonia and/or nitrogen in plasma. PECVD offers the advantage of depositing the film at lower temperatures (below 300°C) which is very beneficial in temperature sensitive processes [94–96]. However, PECVD silicon nitride (Si_xN_y:H) is generally nonstoichiometric and may contain significant concentrations of hydrogen (10-30%). Nevertheless, PECVD offers the ability to deposit low stress SiN films at temperatures lower than LPCVD which is an attractive property, specifically where stoichiometry is not critical.

Silicon nitride has various applications in microelectronics technology such as a dielectric layer, passivation layer, mechanical protective layer, hard mask for KOH etching and oxidation process, and as a CMP stop layer in shallow trench isolation [97]. SiN films have been used in MEMS devices too. They are used as isolation layer, as structural layer such as static membranes [98], and tunable MEMS Fabry–Perot (FP) optical filters [99], where both the mechanical and the optical properties are important.

LPCVD and PECVD SiN material properties for different applications have been studied extensively before. In this article, we investigate the feasibility of using PECVD silicon nitride layer as the sacrificial layer in fabrication of micromachined MEMS devices through studying the influence of process parameters in PECVD on the properties of the resulting films. LPCVD silicon dioxide (SiO_2) is the most widely used sacrificial material in polysilicon surface micromachining [100], because it can be easily dissolved using etchants that do not attack polysilicon. However,

plasma deposited SiN has a number of advantages that can make it another attractive option for sacrificial layers. For example, the high temperature process of SiO_2 layers deposited from a tetraethoxysilane (TEOS) precludes their use in low thermal budget cases such as in the presence of aluminum metallization or shallow implants. PECVD silicon nitride film is conformal and has excellent step coverage and unlike oxide does not undergo excessive shrinkage during later high temperature cycle that causes stress, crack or delamination of the underlying MEMS structure [95].

The physical and chemical properties of SiN are variable and depend on deposition conditions of the films. However, the required properties of SiN film in IC fabrication technology and those of structural or sacrificial layer in MEMS surface micromachining do not necessarily overlap. For a suitable silicon nitride sacrificial layer, low residual stress, high and selective etch rate during the final release etch, acceptable thickness uniformity, no indications of mechanical failure such as crack, delamination, or pinhole at thickness of about 2μm, low thermal budget, and tolerance of later high temperature processes such as polycrystalline silicon deposition in LPCVD, are the crucial properties.

Silicon nitride film deposited on silicon substrate deals with the residual stress. High stress will cause mechanical failure of the film, and this has limited the applicable thickness of SiN layers to only a few hundreds of nanometers. Therefore, minimizing stress in PECVD silicon nitride is the key to achieve higher thickness. In order to obtain low stress SiN film, other than adjusting the deposition conditions, different process recipes have been developed by others. Mixing high and low plasma frequencies [99], addition of He to gas mixture of SiH_4, NH_3, and N_2 [101], and introduction of Ar as a diluting gas into the process [102] are some examples of these works. The total stress of SiN film is composed of two components, thermal stress and intrinsic stress, and it is important to understand and separate these two stress components. The former source of stress is generated by the coefficient of thermal expansion (CTE) mismatch between the deposited SiN layer and the substrate induced due to the cooling after deposition and this leads to compressive stress. Substrate constraints and film modulus also effect on development of thermal stress. This stress can also build up in the next high temperature process. The generation mechanism of the other source of stress, which is mostly tensile in PECVD SiN and can be stronger than the thermal expansion, is very complicated but related to all displacement constraints occurring during thin film growth. There are several explanations and models with limited applicability to explain the

features of intrinsic stress [103]. One of these explanations for intrinsic stress of SiN film is densification occurring inside the film as volatile species are eliminated due to the thermal energy input. The voids left in the film create stretched Si–N bonds which cannot relax as they would at the surface, so the stress stays in [86].

The main parameters that control the growth of SiN films in PECVD are temperature, gasses flow rates, plasma power and pressure. A wide range of experiments are carried out in this study to assess individual and cooperative effects of different process conditions on deposition rate, film stress, etch rate, and refractive index of deposited films. The influence magnitudes of process conditions are evaluated to achieve optimal process conditions for deposition of PECVD silicon nitride used as the sacrificial layer in MEMS device fabrications.

5.3.2 Experimental procedure

A) PECVD equipment and deposition processes

Silicon nitride films were deposited on 4-inch diameter <100> p-type Si wafers using mixture of SiH_4 and NH_3, under a range of conditions using Oxford Plasmalab 80plus PECVD system. Films of varying compositions were deposited by changing deposition conditions with thickness of about 500 nm. Fig. 5.2 shows schematic presentation of the system chamber used in this study, and Fig. 5.3 shows the actual system in our lab.

B) Measurements and material characterization

Semiconductor and MEMS device fabrications consist of a series of sequential process steps in which layers of materials are deposited on substrates. Process monitoring using characterization techniques enables us to achieve the target properties of the film and to detect problems early on to minimize their impacts. Based on observations obtained using our lab's metrology equipment, appropriate actions are taken in order to guide the process to some desirable state. The following techniques were used to characterize the SiN film and obtain the desired process conditions.

Similar to other properties, optical properties of SiN film vary considerably with deposition conditions. Ellipsometry is a common measurement technique based on the polarization changes that occur when light is reflected from or transmitted through a medium. Spectroscopic ellipsometry is a simple and nondestructive diagnostic technique for this purpose. Measurements were performed in the wavelength range of 300 nm to 800 nm using a JA Woollam Ellipsometer.

The model used to fit the spectroscopic ellipsometry data was surface roughness / SiN / c-Si. The surface roughness was modelled using a Bruggeman effective medium approximation [104] consisting of 50% voids and 50% SiN with the thickness of 2nm to 4 nm. SiN film was modelled using Cauchy dispersion equation [105].

Film thickness was measured using a Dektak profilometer on a patterned SiN film using photolithography and wet etching. Profilometry is a common method of film thickness measurement. In this technique, a step feature is first created, either by masking during deposition or by photolithography and then etching afterward. Profilometry was used for residual stress measurements too. The residual stress was calculated using the Stoney equation [106]. The radius of curvature of the wafer was measured using the Dektak profilometer prior to deposition, and then once the film is deposited, the wafer bow is measured again and the resultant change in curvature radius is used to calculate the residual stress. The value of $E_s / (1 - \upsilon_s)$ was taken as 181 GPa [107]. Silicon nitride wet etchants include the family of silicon dioxide with slower rates, and heated phosphoric acid with good selectivity to oxide. Diluted solutions of hydrofluoric acid are extensively used for etching PECVD SiN. Also, buffered HF (ammonium fluoride is added) is widely used to obtain lower etching and higher stability of photoresist layer. In this study, the etch rates of different SiN layers were determined by measuring the film thickness on a half-covered wafer after it was kept immersed in the 5% HF solution for a given time.

Infrared (IR) spectroscopy is a widely-used method for identifying bonds based on the absorption of infrared radiation by molecules at characteristic wavelengths. Radiation causes various bonds to vibrate and the frequency of vibration is dependent on the nature of the chemical bonds present. The intensity of the absorption peaks is also proportional to the amount of material present. FTIR spectroscopy measurements in this study were done using a Bruker Vertex 70 FTIR spectrometer, averaged over 32 scans at a resolution of 2 cm^{-1}.

5.3.3 Results and discussions

With the goal of producing a silicon nitride film with low residual stress, good thickness uniformity, and acceptable etch rate, the experiments carried out in this research work utilized the chamber pressure varied from 400 mTorr to 700 mTorr, the temperature was varied from 200°C to 375°C and plasma power was in the range of 20 to 50W. The total gas flow of the process gases

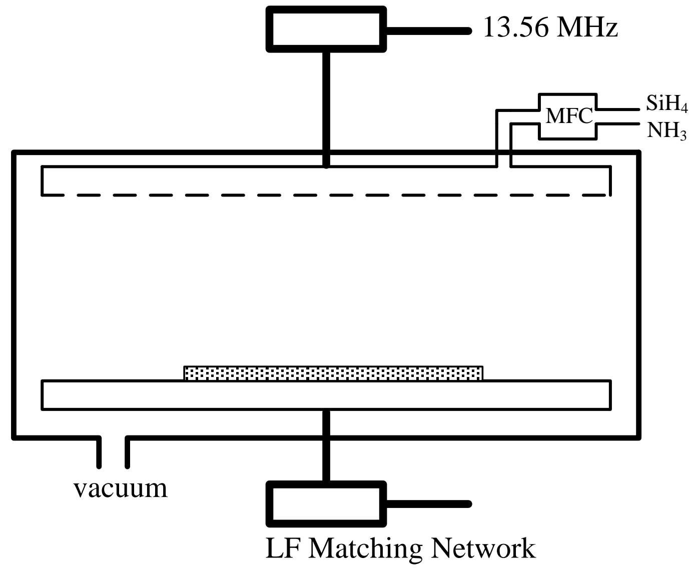

Fig. 5.2: Schematic diagram of Plasmalab Oxford PECVD chamber used for SiN deposition in this study.

Fig. 5.3: Plasmalab Oxford PECVD in our lab used for SiN deposition.

was kept constant at 50 sccm and the SiH_4/NH_3 ratio ranged from 0.3 to 0.1. Table 1 shows a list of performed experiments. Existing work reported in the technical literature was used as the basis for selection of the range of process conditions. Throughout these experiments, while studying the effect of one variable, others were kept constant. The stress in silicon nitride film is the most important consideration if it would be used as the sacrificial layer in MEMS fabrication. The reliability of MEMS devices could be compromised by the stress. Tensile stress may cause cracks and compressive stress may buckle and delaminate the film from the substrate in order to relieve the strain mismatch. It is also shown that that excessive strain may increase leakage if SiN layer is used as the isolation layer [108]. Other than film stress, three film properties of interest in this research were deposition rate, etch rate, and refractive index. Fig. 5.4 up to Fig. 5.11 show the dependences of the SiN film's deposition rate, total stress, etch rate, and refractive index on deposition conditions. Lines with circle markers are related to bottom axes and those with square markers to top axes.

A) Effect of temperature

Effects of temperature on different properties of SiN layer are measured and shown in Fig. 5.4 to Fig. 5.7. Fig. 5.4 shows the deposition rate versus temperature as calculated from the actual thickness of SiN layer and deposition time. There is almost a monotonic decrease with increasing temperature. In order to figure out the reason we should first study Fig. 3 which is showing the FTIR measurements of infrared transmittance spectra of four films grown at different temperatures. Peak assignments were taken from Ref. [109]. The main absorption peaks are due

Table 5.1: Summary of performed recipes.

Exp.	Temp. (°C)	Pressure (mTorr)	Plasma Power (W)	Gas Ratio (SiH_4 / NH_3)
1	250	600	35	0.2
2	300	600	35	0.2
3	350	600	35	0.2
4	375	600	35	0.2
5	350	400	35	0.2
6	350	500	35	0.2
7	350	700	35	0.2
8	350	600	25	0.2
9	350	600	50	0.2
10	350	600	35	0.1
11	350	600	35	0.3

to Si–N bonds at 880 cm^{-1}, Si–H bonds at 2150 cm^{-1}, and N–H bonds at 3340 cm^{-1}. The absorptions from Si–H, N–H, and N–H_2 all decrease with increasing deposition temperature. This means that H content decreases or less hydrogen trapping rate with increasing temperature. Therefore, this causes increase in mass density. Density increase is partly responsible for the decrease in deposition rate [94]. Reduction of precursor sticking coefficient by increasing temperature causes the deposition rate to drop too [86]. As shown in Fig. 5.5, film total stress is always tensile and increases with deposition temperature. As mentioned before, the total stress of SiN film is composed of thermal and intrinsic stress. The increase in total film stress with increasing deposition temperature is due to the effect of both sources. As it was explained above higher deposition temperature causes higher density and this densification occurs inside the film as volatile species are eliminated below the surface due to the thermal energy input. The voids left in the film create stretched Si–N bonds. The relative local atomic strain can be also observed by analyzing the shifts in the Si–N stretching mode [93], [110]. The Si–N peak in Fig. 5.12 changes from 884 cm^{-1} to 873 cm^{-1} by increasing the deposition temperature from 250°C to 375°C. Thermal stress which is due to CTE mismatch between deposited SiN layer and Si substrate leads to relatively small compressive stress (around 80 MPa [94]) because the Si_xN_y:H film has a smaller CTE than the substrate and upon cooling to room temperature, this stress grows. The compressive stress due to CTE mismatch slightly reduces the tensile intrinsic stress, but the intrinsic stress is greater and the net residual stress stays tensile. As the deposition temperature increases, SiN layer gets denser and CTE difference decreases [95]. Therefore, this makes the canceling effect of thermal stress smaller and the total film stress more tensile. Etch rate in an HF solution (5 wt.% in DI water) decreases sharply with increasing temperature due to the increased density and also reduction of H and N contents of the film. Specifically, amino (NH_2) groups, which are base and are readily attacked by acids. Refractive index obviously increases with increasing temperature because of denser film and less hydrogen content.

B) Effect of pressure

Chamber pressure is another parameter which was varied while keeping other conditions constant. Fig. 5.4 to Fig. 5.7 show how film properties change with pressure. Higher pressure at fixed gas flow provides more residence time for amination reaction in plasma to proceed and also more deposition time before the radicals and products are gone. Therefore, this increases the deposition

rate [94]. High pressure also causes higher hydrogen trapping by further deposition before dissociating and therefore reduces the density of the film. Higher pressure decreases the effect of plasma by decreasing energy of bombarding ions, too. Therefore, the effect of increasing pressure would be roughly in opposite direction of the effect of plasma power which is explained in the following section. Furthermore, pressure has a great effect on plasma stabilization and this caused the non-uniformity of the film to increase beyond the acceptable limit at lower pressure values. Therefore, a pressure value of around 600 mTorr would be optimal in our PECVD chamber.

C) Effect of plasma power

Plasma power is another critical deposition condition that greatly influences the characteristics of the SiN film. Effects of plasma on different properties of the SiN film are shown in Fig. 5.8 up to Fig. 5.11, while other parameters were kept constant. These effects include lower deposition rate, hydrogen content, total stress, and etch rate, and higher refractive index with increasing the plasma power in the film deposition. Increasing plasma power raises bombardment by accelerated ions which causes densification of the layer and also enhancement of surface reaction during film growth [111]. As mentioned before, density increase is partly responsible for the decrease in deposition rate. Higher plasma power assists surface condensation as opposed to condensation occurring below the surface due to thermal energy. Therefore, this condensation reaction during the film growth on the film surface can account for lower tensile stress [86]. At higher gas flow rates, the deposition rate will probably increase with plasma power because the dissociation of gases increases until dissociation of all the molecules is complete. It should be also mentioned that increasing power more than 50 W reduced the uniformity of the film below the acceptable range.

D) Effect of gas flow rate ratio

In order to study the effect of gas flow ratio on the film properties, the SiH_4/NH_3 ratio ranged from 0.1 to 0.3. The total gas flow of the process was kept constant at 50 sccm. Deposition gas ratio had a considerable effect on refractive index as it is shown in Fig. 4d. As the material becomes silicon rich with increased silane flow, it increases and approaches to silicon's. With an increase in the gas ratio density increases [112] and CTE mismatch decreases and this reduces the canceling effect of compressive thermal stress. If we continue increasing gas ratio, stress will decrease. This compositionally induced stress relaxation occurs because of the molecular level strain relief due to the replacement of Si for N in the tetrahedral unit [113].

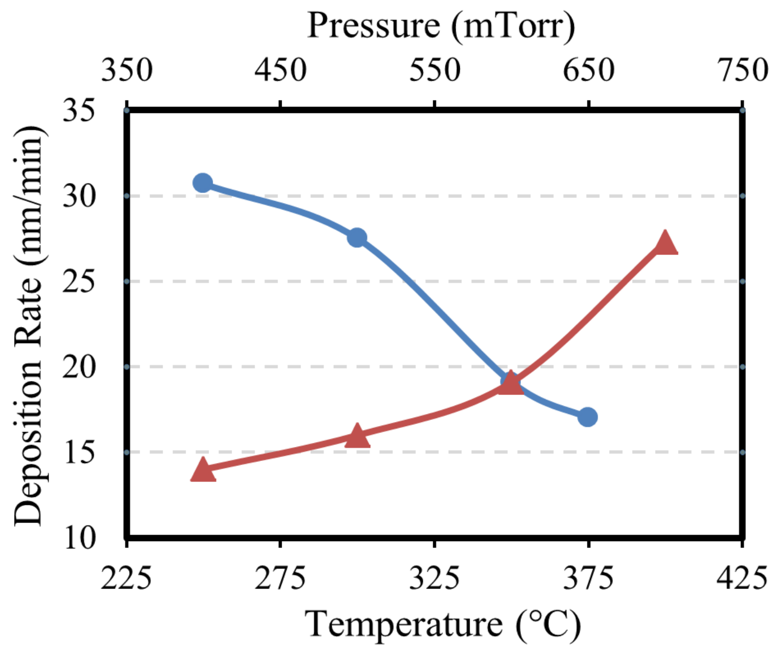

Fig. 5.4: SiN film's deposition rate versus temperature (circle markers) and pressure (triangle markers).

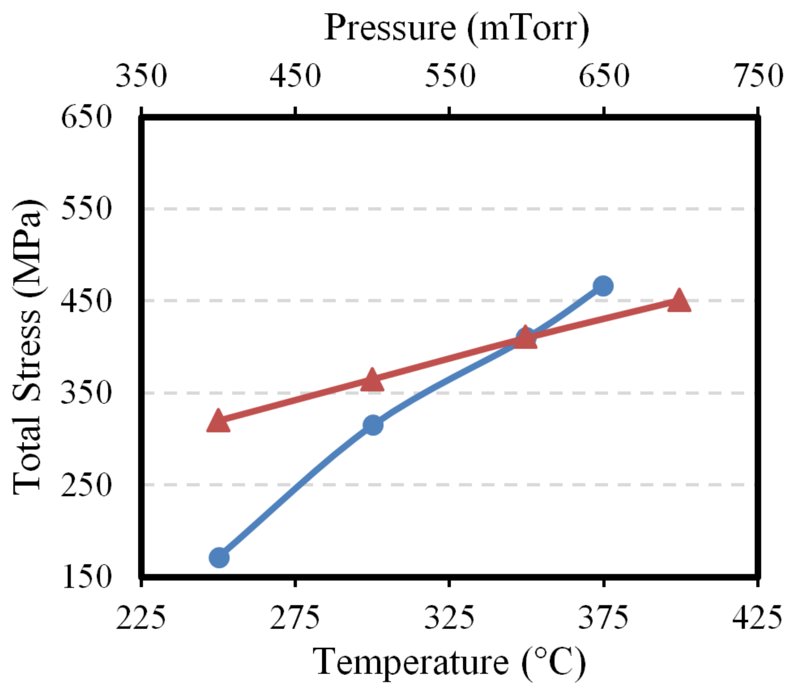

Fig. 5.5: SiN film's total stress versus temperature (circle markers) and pressure (triangle markers).

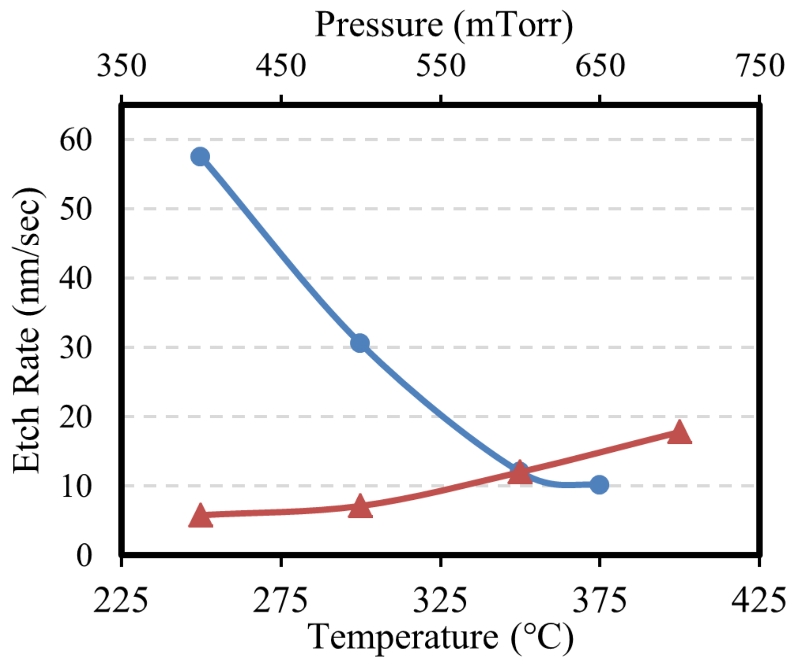

Fig. 5.6: SiN film's etch rate versus temperature (circle markers) and pressure (triangle markers).

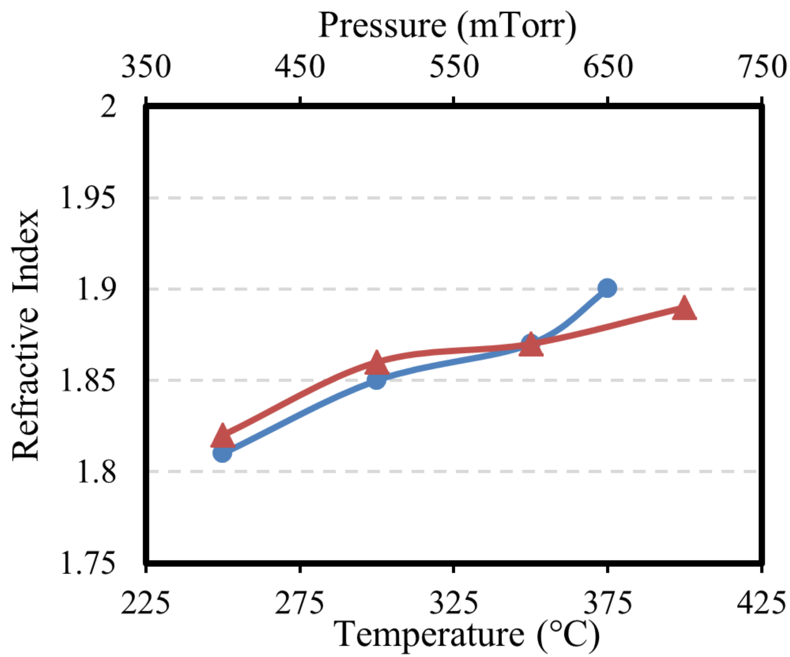

Fig. 5.7: SiN film's refractive index versus temperature (circle markers) and pressure (triangle markers).

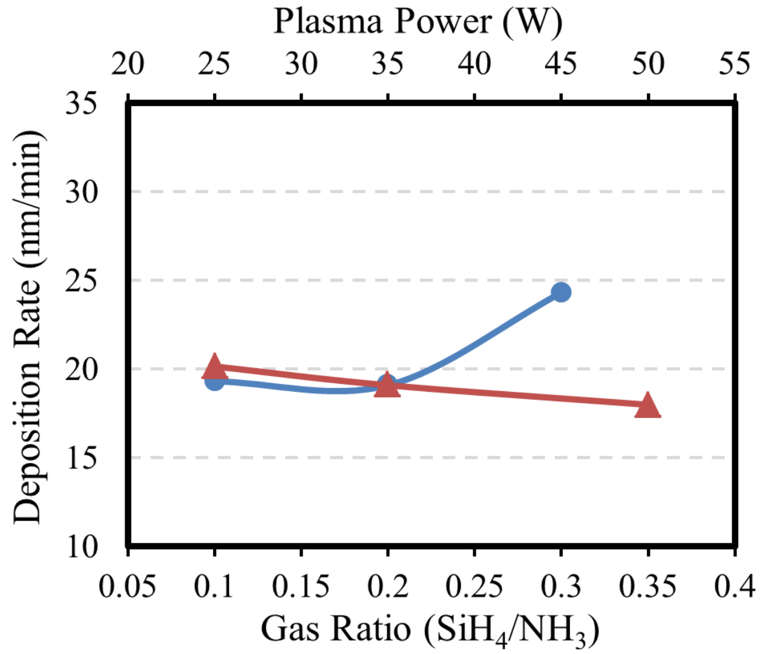

Fig. 5.8: SiN film's deposition rate versus gas ratio (circle markers) and plasma power (triangle markers).

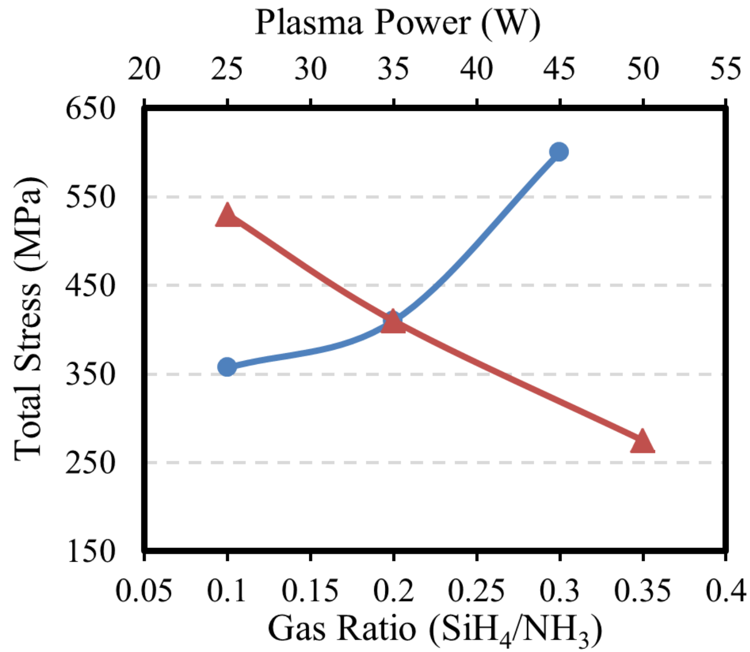

Fig. 5.9: SiN film's total stress versus gas ratio (circle markers) and plasma power (triangle markers).

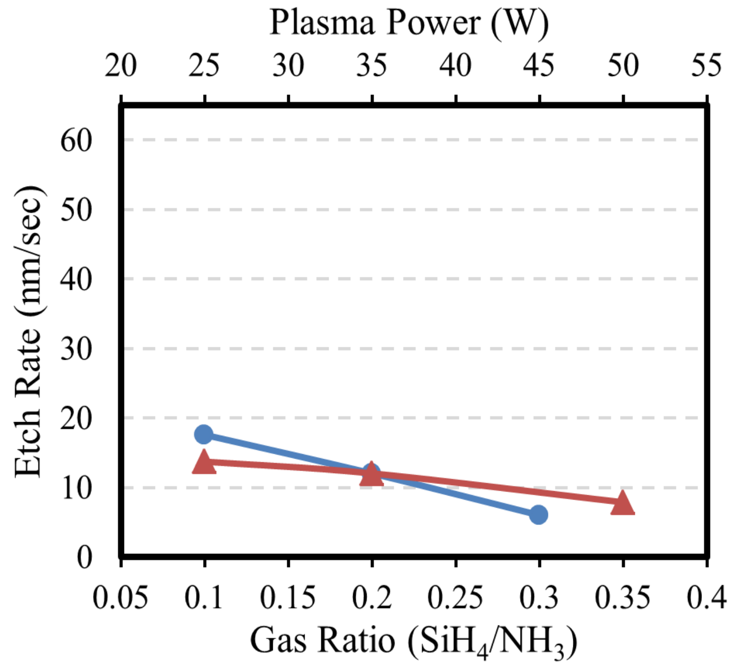

Fig. 5.10: SiN film's etch rate versus gas ratio (circle markers) and plasma power (triangle markers).

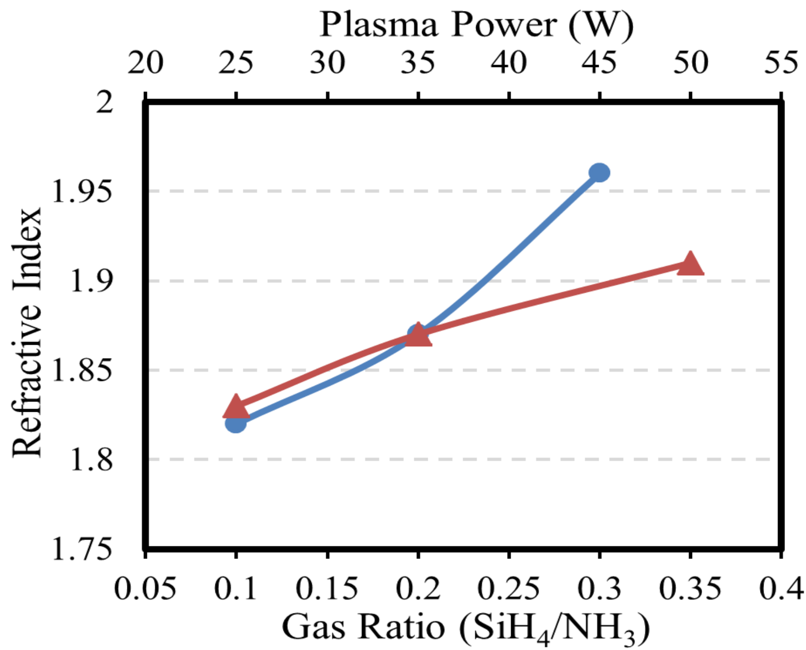

Fig. 5.11: SiN film's refractive index versus gas ratio (circle markers) and plasma power (triangle markers).

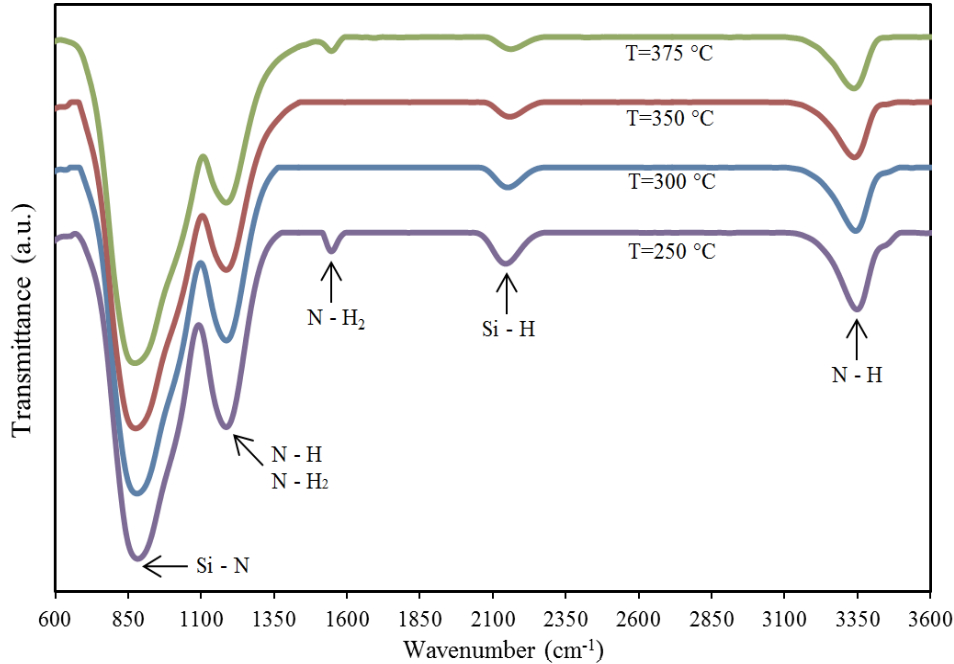

Fig. 5.12: The infrared transmission spectra of SiN film deposited at different measurement temperatures.

5.3.4 Selection of the optimal process conditions

Selection of the optimal process conditions must be done based on application characteristics. For example, if the SiN film is intended to be used as a masking layer for etching of silicon in KOH solution, low content silicon is desired and low residual stress is not critical. In our application of using the SiN film as sacrificial layer, as mentioned before, the goal is minimizing residual stress while maximizing the etch rate, deposition rate and thickness uniformity as much as possible. The residual stress of SiN film may cause mechanical failure. Compressive stress causes delamination, but we found out that it can be highly avoided by having a stable native oxide layer on a cleaned substrate and deposition temperatures above 200 °C. Silicon nitride film under tensile stress relieves its stress by cracking. Cracking often occurs at a critical film thickness or when temperature is exceeded over the deposition temperature due to thermal stress built up. As it was explained before, thermal stress is the second source of stress and upon heating; above the deposition temperature, stress will get more tensile, because the SiN film has a smaller CTE than the Si substrate. Therefore, application of SiN layer would be limited to a few hundreds of nanometer and further high temperature processing (> 450˚C) is also avoided. Fig. 4 shows an optical micrograph of cracked SiN film occurred in LPCVD chamber at a temperature around 600 °C before the start of polysilicon deposition.

The cumulative influence of process values based on the results shown before are assessed and summarized in Table 5.2. Therefore, the optimal process condition is suggested to be T=250°C, PP=45W, P=600mTorr, and GR=0.15. However, these process conditions do not necessarily guarantee a crack resistant layer. The cracking resistance will be improved by reducing the stress, increasing the film density, and reducing the CTE mismatch between the film and substrate [114]. Film density can be an indicator of strength of the film. Factors which decrease the film density can also create microscopic flaws which will cause mechanical failure of the film under stress. Density can be increased by raising temperature, plasma power, gas ratio, and by reducing pressure. CTE mismatch between SiN film and Si substrate develops high tensile stress during heating in high temperature process. It has been reported that higher deposition temperature and plasma power will reduce the mismatch [92], [112]. Hence, finding the least CTE mismatch is important in achieving lowest thermal stress.

Table 5.2: Responses of film properties to variation of process conditions. "+ +" represents very high, "+" represents high, "–" represents low, and "– –" represents very low influence.

	Gas Ratio (SiH_4 / NH_3)	Temperature	Plasma Power	Pressure
Deposition rate	+	– –	–	+ +
Residual stress	+ +	+ +	– –	+
Etch rate	–	– –	–	+
Refractive index	+ +	+	+	+

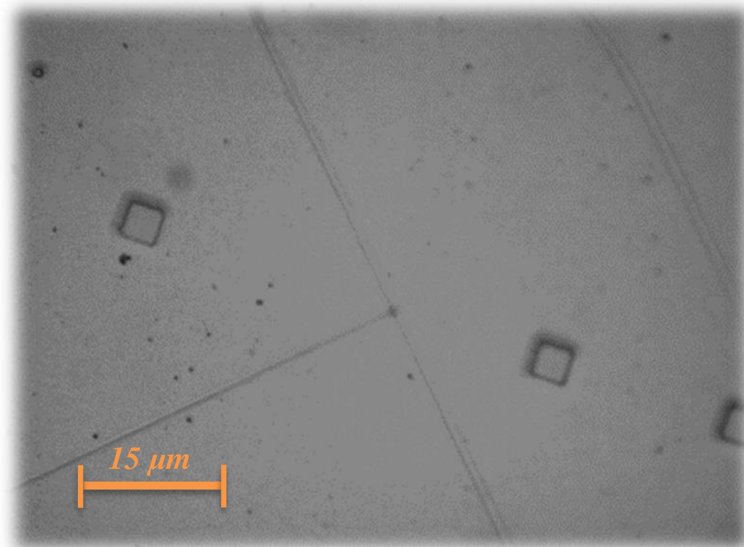

Fig. 5.13: Optical micrograph of the cracked SiN film surface.

5.4 Process Development of LPCVD Polycrystalline Silicon

5.4.1 Introduction

One of the key factors in fabrication of dense CMOS chips is the use of polycrystalline silicon (polysilicon) as the gate-electrode material. The use of polysilicon allows self-aligned structure formation, improves device characteristics and makes the device compatible with subsequent high temperature processing. These factors permit polysilicon to be used for trench isolation, in bipolar circuits, in DRAM storage capacitors, and as the channel of thin-film transistors for switching pixels of LCDs. Furthermore, a considerable research on the properties of polysilicon has been motivated by solar-cell applications. Polysilicon can also form mechanical elements of a MEMS device, especially microsensors and microactuators. Integrated circuit is a mature technology for fabrication and has been the basis for steady advances in MEMS fabrication technology and microfabrication process technology has been inherited from that. In MEMS devices, mechanical properties, especially stress in the film, are important in successful device fabrication. The microstructure of polysilicon thin films consists of grain like structures separated by grain boundaries. The grains are mini-crystalline that their orientation varies with respect to each other. The presence of grain boundaries in polysilicon introduces a variety of electrical and mechanical properties in polysilicon. For example, the young's modulus depends on crystal structure and orientation which is highly dependent on deposition conditions. The fracture strength is also dependent on grain size and fracture surface energy. The energy needed to fracture a grain surface also increases with grain size.

5.4.2 Deposition process

MEMS polysilicon films are commonly deposited by CVD. Typical processes are performed in horizontal furnaces at temperatures ranging from 580 to 650 ˚C and pressures from 100 to 400 mTorr. The most commonly used source gas is silane (SiH_4). First, silane is adsorbed on the surface and then decomposes to form SiH_2 and hydrogen. The SiH_2 further decomposes to form polysilicon. The chemical reaction is expressed as

$$SiH_4\,(g) \longrightarrow Si\,(s) + 2H_2\,(g)$$

The overall deposition process is the sum of a series of steps. First, silane gas enters the chamber

by forced convection and flows to near the wafer. It adsorbs to the wafer by diffusing through a boundary layer and then decomposes to silicon and hydrogen. Finally, silicon atoms diffuse to stable sites and hydrogen atoms or molecules desorb from the surface.

A) Convection

The high pressure gas may be forced through the reactor chamber at atmospheric pressure or in a low pressure chamber the gas may flow resulting from pumping at the exhaust. At low gas velocities, free convection is established by temperature gradients, and obtaining uniform deposition with irregular and spiral gas flow of free convection is very difficult. At higher gas velocities, forced convection will be established inside the chamber, and the gas flows mostly parallel to the chamber walls. By using an LPCVD machine that the walls are uniformly heated (hot-wall reactor) and can work at low pressure, little thermal gradient exists and forced convection is created at even low gas velocities [115], [116].

B) The boundary layer

The reduced velocity of molecules near the chamber walls or the wafer slows down the nearby molecules too by momentum transfer. Therefore, a low-velocity boundary layer is created that separates forced convection region from the surfaces. The thickness of this boundary layer (δ) depends on velocity, density and viscosity of the gas [117] and the reactant gas molecules can reach the wafer by diffusing through this layer. The reactant concentration across the layer creates the driving force for this diffusion flux (F_1).

C) Decomposition of silane

Silane decomposes in two possible ways, on the surface, which is called heterogeneous decomposition, or in the gas phase, which is called homogeneous decomposition. In order to form a dense and low defect layer, heterogeneous decomposition should dominate [118]. In certain deposition conditions, partial decomposition of silane in the gas phase to form intermediate gas silylene (SiH_2) is possible [119]. Thermodynamic data show that at low pressure, this partial decomposition decreases several orders of magnitude [120]. That is another reason to use LPCVD machine to deposit good quality polysilicon.

D) Reaction and steady state

On the surface of the wafer, there is another flux (F_2) of reactants entering into the chemical reaction. When $F_1 >> F_2$, the deposition process is called reaction-rate limited and the deposition

rate is a strong function of temperature. By increasing temperature, reaction rate increases very fast but diffusion coefficient increases slowly, and in this region, both diffusion and reaction affect the deposition rate. If we continue increasing the temperature, reaction rate increases more up to a point where the overall deposition process is then limited by the transport rate of reactants to the wafer surface. In this region, the process is said to be mass-transport limited.

E) Surface diffusion and nucleation

The polysilicon structure is formed by nucleation on the substrate first and then then the structure continues to develop as the film becomes thicker. When the silane and intermediate reactants reach the wafer surface, they adsorb and may be able to diffuse on the surface before decomposing to silicon and hydrogen. After decomposition, silicon atoms can diffuse to stable sites and subsequently arriving silicon atoms complete bonds. Hydrogen atoms liberated by decomposition can simultaneously diffuse on the surface and find another hydrogen atoms, combine, and then desorb as a hydrogen molecule. Therefore, the number of formed nuclei depends on surface diffusion of silicon atoms. At higher diffusion, fewer but larger nuclei will be formed.

Deposition conditions which allow farther diffusion on the surface before being immobilized by arriving silicon atoms form larger grains and better defined structure. Surface migration can be increased at higher surface temperature, and can be decreased when many of adsorption sites are filled by other non-silicon atoms which occurs at higher pressures or when contaminants are present. Also at higher arrival rate of silicon atoms, the diffusion time before being immobilized is shorter, which limits the amount of migration possible [121].

F) Effect of dopants

Although polysilicon can be doped by diffusion, in situ doping during the LPCVD process is an effective means of modifying the electrical properties of the film. In situ doping of polysilicon can be done by simply including a dopant gas, usually diborane (B_2H_6) or phosphine (PH_3), in the CVD process. In situ doping is used to produce conductive films for electrostatic devices, but has also been used to create polysilicon-based piezoresistive strain gauges. Adding phosphine decreases deposition rate significantly, while diborane increases the rate [122]. The changes in rates are more pronounced at lower temperatures where the process is dominated by surface reactions, as opposed to high temperatures that diffusion through boundary layer limits the rate [123]. Phosphorous and its precursors are adsorbed 40 times more strongly than silane and block

adsorption of silane by occupying the sites. Diborane increases the deposition rate by the addition of a parallel deposition mechanism where boron surface atoms act as a catalyst and decompose silane at a lower activation energy [124].

G) Effects of annealing

Annealing recrystallizes the film, grows grains and also reduces defects. During the annealing, vacancies move and condense into dislocation. Dislocations move through creep and glide and disappear in the surface. As vacancies and dislocations are reduced, the entire film is densified. Grain growth happens by small size grains getting consumed by the larger neighbors.

5.4.3 Deposition of polysilicon by LPCVD in our lab

Polysilicon films were deposited by CVD Equipment's LPCVD furnace on 4 inch, p-type, and [100] oriented silicon wafers. As it is shown in Fig. 5.14 the furnace is based on a hot-wall, three-zone resistance-heated, horizontal, fused-silica tube design. Wafers are placed on a quartz boat with 1-inch spacing. In order to obtain uniform deposition, process must be performed in the reaction-limited regime. In the reaction-limited deposition regime, the deposition rate is determined by the reaction rate of the reacting species on the substrate surface, as opposed to the arrival rate of the reacting species to the surface (mass-transport regime or diffusion-controlled regime). For typical LPCVD processes (e.g., 200~400 mtorr), the amorphous-to-polycrystalline

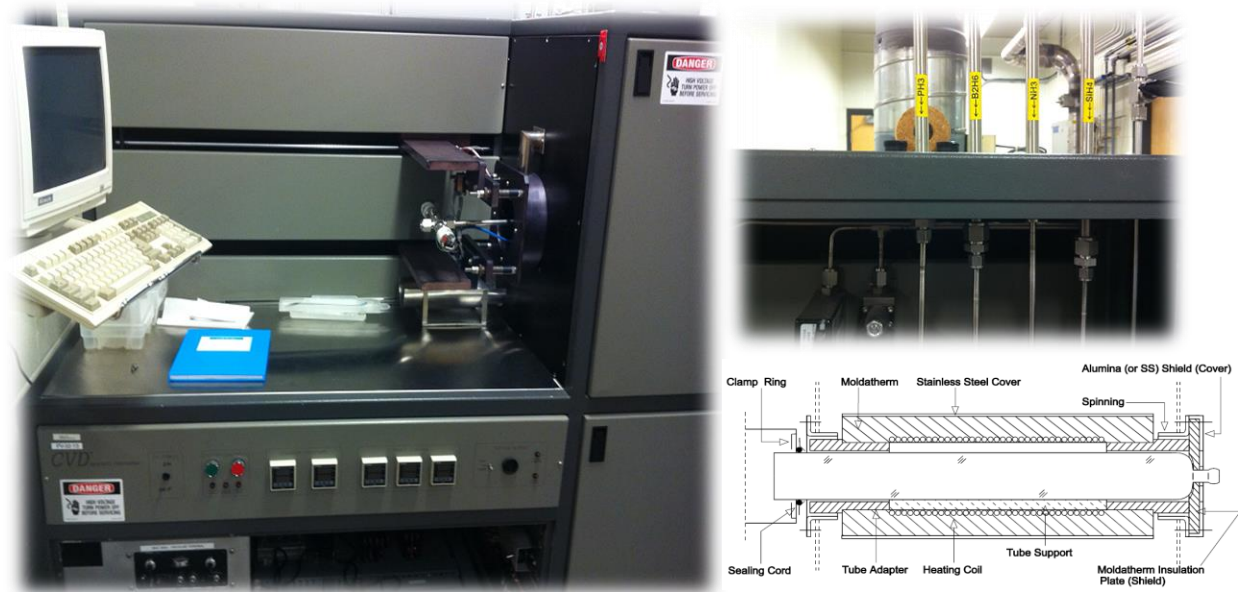

Fig. 5.14: LPCVD machine in our lab with gas connections and the schematic of the tube.

transition temperature is about 570°C, with polycrystalline films deposited above the transition temperature. Gas flow rates depend on the tube diameter and other conditions. Practical deposition rate is in the range of 10 to 20 nm/min. The properties of the polysilicon film are determined by deposition temperature, pressure, silane flow rate, and dopant content.

5.4.4 Characterization methods

A) Raman spectroscopy

Raman spectroscopy is an effective technique for characterization studies on silicon films. Raman spectroscopy is employed in this work for the purpose of determining the amorphous versus crystalline volume of the polysilicon films, and approximately residual stress and doping level of the film. To perform the Raman measurements, Raman microscope manufactured by Renishaw was utilized. The system's excitation laser operated at a wavelength of 632 nm. Raman spectroscopy is based on inelastic scattering. Photons impinge on atoms in the film and are either absorbed, reflected elastically, or interact inelastically by being absorbed and promoting atoms in the material to a raised state. Phonon interactions can either shift the energy of the emitted photons down (Stokes scattering) or up (anti-Stokes scattering). In crystalline silicon, this interaction manifests as a Lorentzian peak sharply centered around 521 cm^{-1}. Amorphous silicon is not as an efficient Raman scatterer and exhibits a broad Gaussian peak at around 480 cm^{-1}. The Raman spectra of mixed-phased silicon is therefore a convolution of both of these modes.

B) Dektak profilometer and wafer curvature

Film thickness was measured using a Dektak profilometer on a patterned SiN film using photolithography and wet etching. Profilometry is a common method of film thickness measurement. In this technique, a step feature is first created, either by masking during deposition or by photolithography and then etching afterward. Profilometry was used for residual stress measurements too. The residual stress was calculated using the Stoney equation [106]. The radius of curvature of the wafer was measured using the Dektak profilometer prior to deposition, and then once the film is deposited, the wafer bow is measured again and the resultant change in curvature radius is used to calculate the residual stress. The value of $E_s / (1 - \upsilon_s)$ was taken as 160 GPa [107].

C) Four-point probe measurement

A four-point probe instrument was used to measure polysilicon thin film resistivity. It consists of

four in-line sharp probes spaced 0.5cm apart which are pressed into the surface. A current passes through the outer probes while the inner ones measure the voltage drop.

5.4.5 Results and discussions

Numerous deposition conditions are studied to deposit polysilicon films (as deposited and n-doped) with LPCVD in our lab. These studies have examined the influence of reactor parameters such as temperature, gas flow rates, and pressure on crystallinity, stress and resistivity of the films. Fig. 5.15 shows the effect of silane flow rate and the deposition temperature on deposition rate based on our lab's LPCVD measurements. At low input silane, the deposition rate increases linearly by increasing silane flow rate, until most adsorption sites are filled by unreacted SiH_4 and adsorbed H, the deposition rate starts to saturate.

When the temperature increases, the surface reaction rate becomes higher than the arrival rate of silane. In this regime of mass-transport limited, deposition depends on gas flow and tube geometry. At low temperature, the surface reaction rate is smaller than the arrival rate of silane. So, the deposition is surface reaction limited and temperature is the critical variable. Generally, and as shown, the deposition rate is correlated to the square root of the silane flow rate and

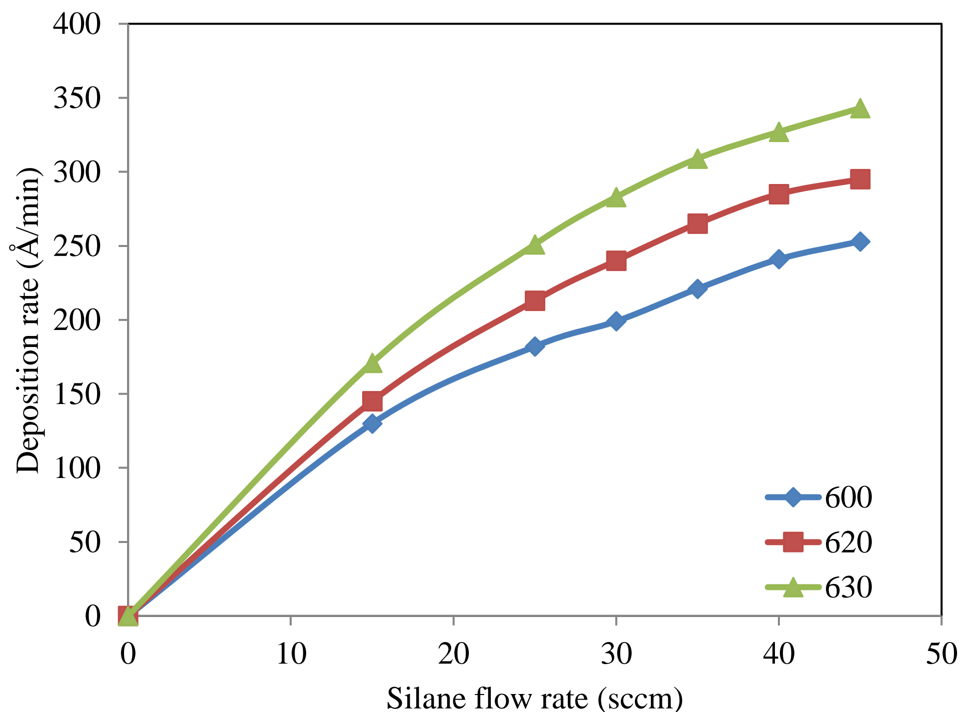

Fig. 5.15: Effect of silane flow rate and deposition temperature on deposition rate polysilicon.

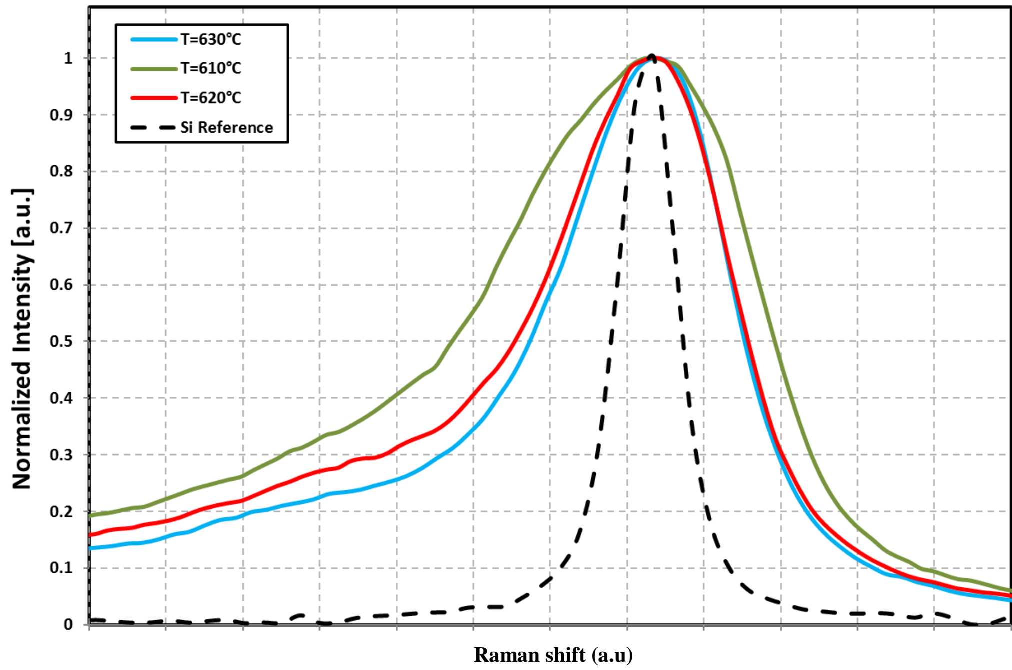

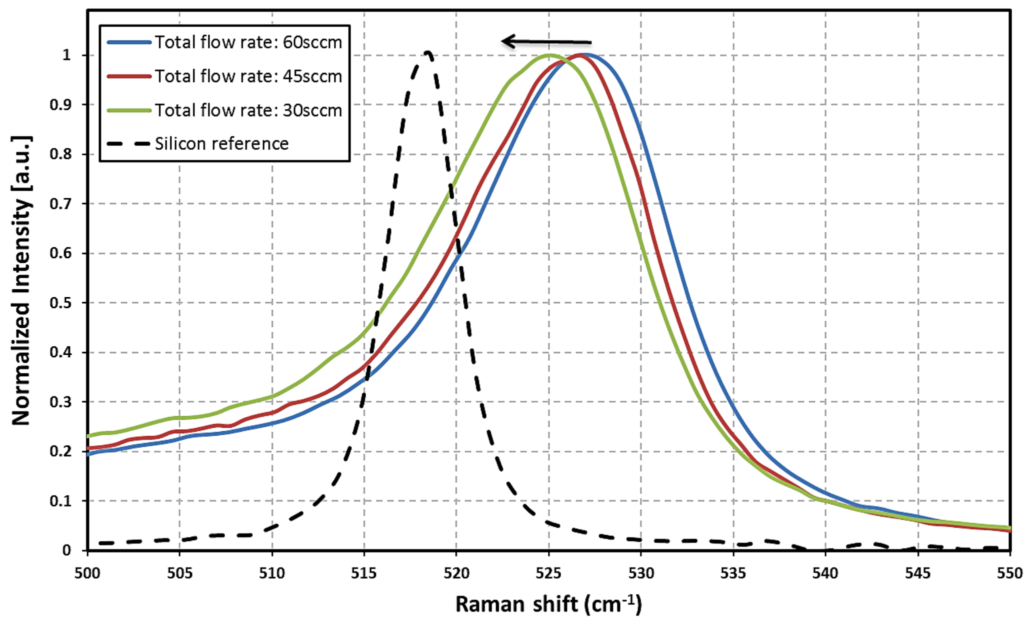

Fig. 5.16: Top: Raman measurement of three different deposition temperature showing the better crystallinity at higher temperatures. Bottom: Different gas flow rates deposited at 630°C showing that lower flow rate causes less residual stress of the polysilicon film.

exponentially dependent on the temperature. The film deposited below 600˚C will show amorphous or microcrystalline structure. Silicon films deposited above 600˚C possess polycrystalline structure. This transition temperature is not constant and depends on pressure, deposition rate and dopant concentration. The polysilicon will have columnar grains with sizes about 0.1 μm and {110} preferred orientation. At temperatures above 650˚C, {100} orientation will increase.

Raman measurement results shows better crystallinity for the films deposited at higher deposition temperature, which was expected. Also, Raman measurement results of three different gas flow rates deposited at 630°C show that lower flow rate causes less residual stress of the polysilicon film. Finally, Raman measurements show that higher ratio of PH_3 to silane and also lower gas flow rate will decrease the crystallinity.

5.4.6 Optimum deposition conditions

Mechanical properties of polysilicon are important particularly in MEMS applications which rely on it as a mechanical element. Polysilicon contains grains of different crystal orientation, and since mechanical properties of silicon depend on its crystallographic orientation, mechanical properties of polysilicon are roughly an average over the dominant grain orientations. Elastic constants of polysilicon are not dominated by grain boundaries. For example, Young's modulus of polysilicon is about 160 GPa, where single-crystal silicon's is about 190 GPa [125]. For MEMS application the choice of optimum deposition condition is governed film stress, particularly when it is used as the structural layer. Polysilicon films are generally under high compressional stress and will cause cracking the underlying films or in released structures will show deformation. The later issue can be fixed by subsequent high temperature annealing. Therefore, the optimum LPCVD polysilicon deposition condition for this research is chosen to be T=630°C, P=300mTorr, SiH_4=20sccm, and PH_3(2%)=10sccm. The resistivity of this layer was measured to be ρ=3.85mohm.cm, and deposition rate to be 15 nm/min, and residual stress of 150 MPa. Also, as it is shown in Fig. 5.17 polysilicon layer suffers from compressive residual stress that causes the beams to curve up. In order to fix that annealing of the polysilicon was performed in Rapid Thermal Processing (RTP) furnace at 950 °C for 5 minutes under N_2 ambient. Annealing also activates the dopants and lower the sheet resistance up to 10 times.

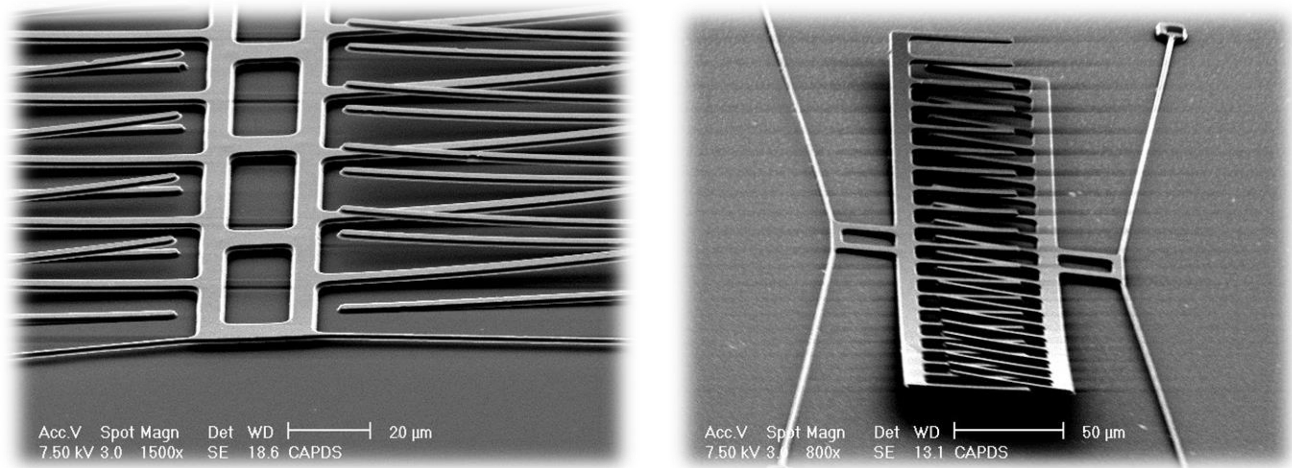

Fig. 5.17: Effect of residual stress on free standing structure. The structure is buckled up due to the compressive residual stress before annealing.

5.5 Photolithography, Pattern Transfer, and Plasma Etching

The concept behind photolithography is quite simple. The process uses a patterned mask made of transparent and opaque regions. Using an optical projection system, this pattern is illuminated onto a photosensitive film called a photoresist. When light strikes the photoresist, it causes a chemical change in the photoresist film which in turn changes the ability of the photoresist to be dissolved by various solvents. This allows specific areas of the photoresist layer to be removed, which exposes the underlying substrate surface for further processing.

Traditionally, wet etching has been used since the inception of the microelectronics industry. Wet etching is often fast, selective, and low damage; however, it is non-directional, i.e. etching proceeds laterally into the etched profile, and is therefore unacceptable [126]. On the other hand, ion beam etching technique employs a collimated beam of high energy ions to physically displace atoms. This technique can be highly anisotropic, but has poor selectivity, and the level of damage may become undesirable [127]. Plasma etching is in the compromise regime, where chemical etching components and the physical component are combined. Silicon etching in halogen plasmas is one of the earliest etch processes. Carbon tetrafluoride (CF_4) gas is dissociated and ionized to produce F atoms and charged ions, which diffuse to the substrate, react, and produce the etch effluent product SiF_4. Ion bombardment, if available, can significantly increase the plasma etch

rate and enhance anisotropy. In the above case, ion bombardment enhances adsorption of reactive neutral by clearing the fluorinated surface film and exposing reactive surface sites. The chemistry of plasma etching can be partially controlled by adding Oxygen or Hydrogen gas. The etch rate of Si in CF_4 can be increased by adding O_2 to the chamber. Atomic Oxygen from dissociated Oxygen molecules reacts with gas phase Carbon fragments to form CO or CO_2, freeing atomic fluorine. 10-15% of O_2 with respect to CF_4 results the highest etch rate and acceptable selectivity over photoresist which I use as the mask in this process. Hydrogen, on the other hand, slows the silicon etch rate because it combines with F atoms and forms HF. However, Hydrogen does not affect the SiO_2 etch rate, therefore H addition can be used to enhance the etch selectivity [128].

The biggest challenge in this part of the research was achieving an acceptable etching aspect ratio profile, i.e. the ratio of etched depth to width, using our lab's RIE (Reactive Ion Etching) machine with gas connectivity of SF_6, CF_4, H_2, and O_2. Specifically, in the comb-drive design's fingers which narrow features are supposed to be deeply etched, I was dealing with several problems such as loosing anisotropic etching, aspect ratio dependent etch rate, microtrenching and notching. It should be also noted that aspect ratio dependent etch rate, or sometimes called 'microloading' happens when aspect ratio increase causes the angular restriction of the etchant flux. A more difficult problem occurred when I was trying to etch the bent-beams, which are very narrow features next to an open field.

Since I was using AZ3312 photoresist as the mask, a careful process recipe must be developed to obtain a thick enough mask layer that could stay the whole etch process. The hardest step was plasma etching of the polysilicon structural layer where somewhat high aspect ratio was required. The remedy that I found useful in our lab was first to start the plasma etch process with lower bias voltage and higher pressure. The beginning of the etch process does not necessarily requires longer mean free path of etching species, and higher bias voltage will attack and etch the photoresist mask faster. Later on, to avoid the undercutting, pressure of the chamber is lowered and bias voltage is increased gradually. However, since chemical etching is the only mechanism of material removal, lowering the pressure would slow the etching in constant proportion.

Second, CF_4 was selected over SF_6 as the main etching gas because it showed less etch rate of photoresist. Also although addition of 10% O_2 increases the etch rate of silicon but it lowers the selectivity of the etch process and attacks photoresist faster. On the other hand, addition of H_2

decreases the etch rate of silicon but causes more anisotropy and also due to the polymerization it slightly passivates the side walls. Therefore, a combination of these two processes has been used sequentially to obtain anisotropic high aspect ratio etching profile.

5.6 Process Integration for MEMS Device Fabrication

The overall process is a two-layer polysilicon surface micromachining process and begins with a 4-inch p-type (100) silicon wafer. Prior to layer depositions the silicon wafer is cleaned using a standard RCA cleaning procedure to remove both ionic and organic contaminants: Immersion in $H_2O/NH_4OH/H_2O_2$ bath, then de-ionized (DI) water rinse followed by a second immersion in a $H_2O/H_2O_2/HCL$ bath. Next, a 300 nm low stress, high density, low etch rate PECVD silicon nitride (SiN 1) layer is deposited on the wafer as an electrical isolation layer. This is followed directly by the deposition of a 300 nm LPCVD n-doped polysilicon film, Poly 1. Poly 1 is then patterned (Fig. 5.18) by photolithography which includes the coating of the wafer with photoresist on spinner, exposure of the photoresist with the appropriate mask under mask aligner and developing the exposed photoresist in developer solution to create the desired etch mask for subsequent pattern transfer into the underlying layer (Fig. 5.19). After patterning the photoresist, the Poly 1 layer is then etched in a plasma etch (RIE) system. Next, a 2.0 µm low stress, high etch rate, and mechanically strong silicon nitride (SiN 2) is then deposited by PECVD. This layer of silicon nitride, known as sacrificial layer, is removed at the end of the process to free the structural layer of polysilicon (Poly 2). The sacrificial layer is lithographically patterned with the anchors mask and then transferred into the layer by plasma etching. Anchor holes are etched down to the Poly 1 layer to provide a mechanical and electrical connection between the Poly 1 and Poly 2 layers. Then the structural layer of polysilicon (Poly 2) is deposited at a thickness of 3.0 µm. Then wafer is annealed at 950°C for 5 min in RTP. The anneal significantly reduces the residual stress, grows grain sizes and activates dopants in the Poly 2 layer. The polysilicon is lithographically patterned using fouth mask designed to form the structural layer (Fig. 5.20) and anisotropically etched according to the developed recipe explained in Section 5.5. Photoresist is stripped at the end and the wafer is cleaned by O_2 plasma. The final deposited layer in the process is a 0.5 µm metal layer using e-beam evaporation system that provides contact pads for probing. The metal layer is patterned using lift-off process. The unreleased structures on the wafer are diced and finally the

sacrificial layer is removed in BHF and the structure is releases (Fig. 5-20). This is followed by several minutes in DI water and then alcohol to reduce stiction. Fig. 5.21 and 5.22 show the device after release.

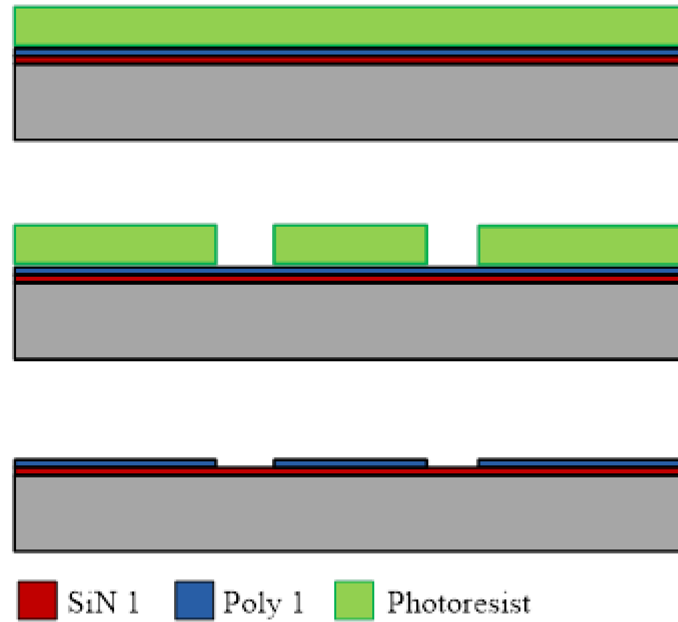

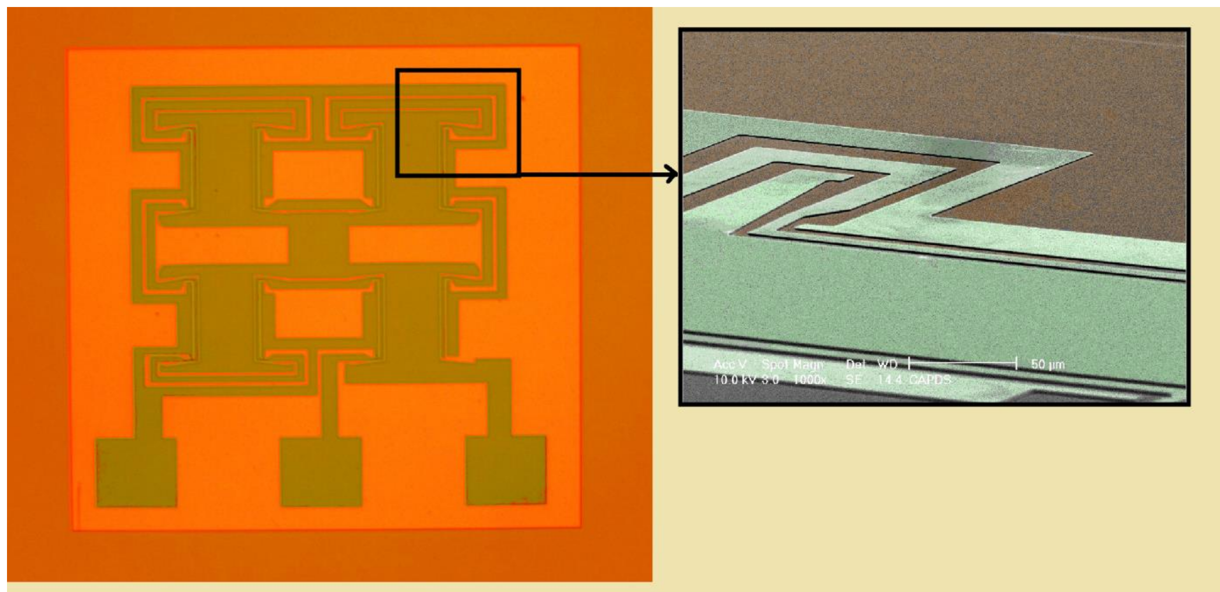

Fig. 5.18: The starting wafer is RCA cleaned, followed by a 300 nm layer of SiN 1 followed by a layer of 300 nm of Poly 1. The wafer is then coated with photoresist. The photoresist is patterned by exposing it to UV light through the first level mask and then dev eloping it. The photoresist in exposed areas is removed leaving behind a patterned photoresist mask for etching. Plasma etching is used to remove the unwanted polysilicon. After etch, the photoresist is stripped. This method of patterning the wafers with photoresist, etching and stripping the remaining photoresist is used repeatedly in the process.

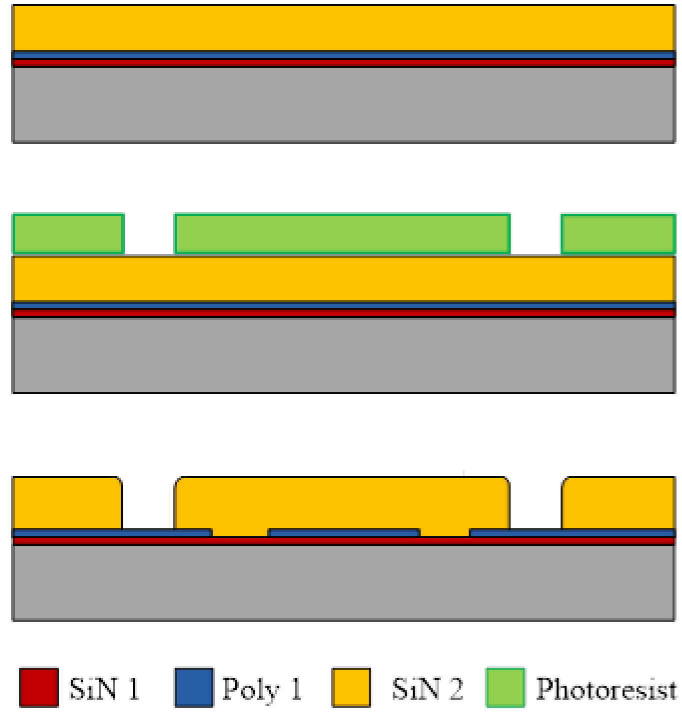

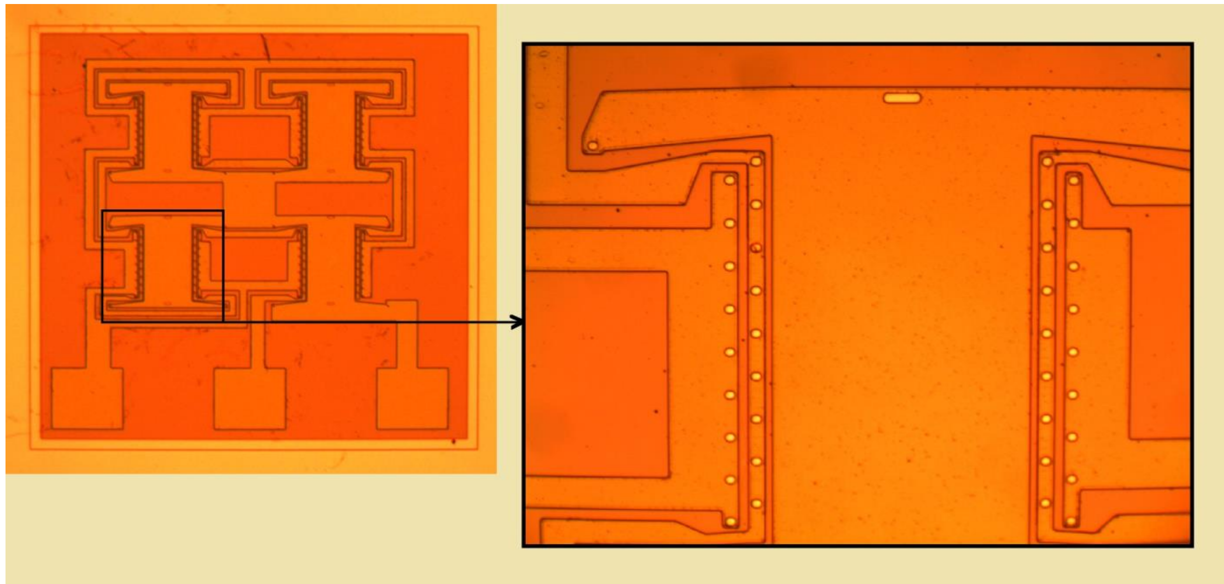

Fig. 5.19: A 2.0 µm layer of SiN 2 is deposited on the wafers by PECVD to serve as the sacrificial layer. Then the wafer is coated with photoresist and the anchors are patterned and then plasma etched.

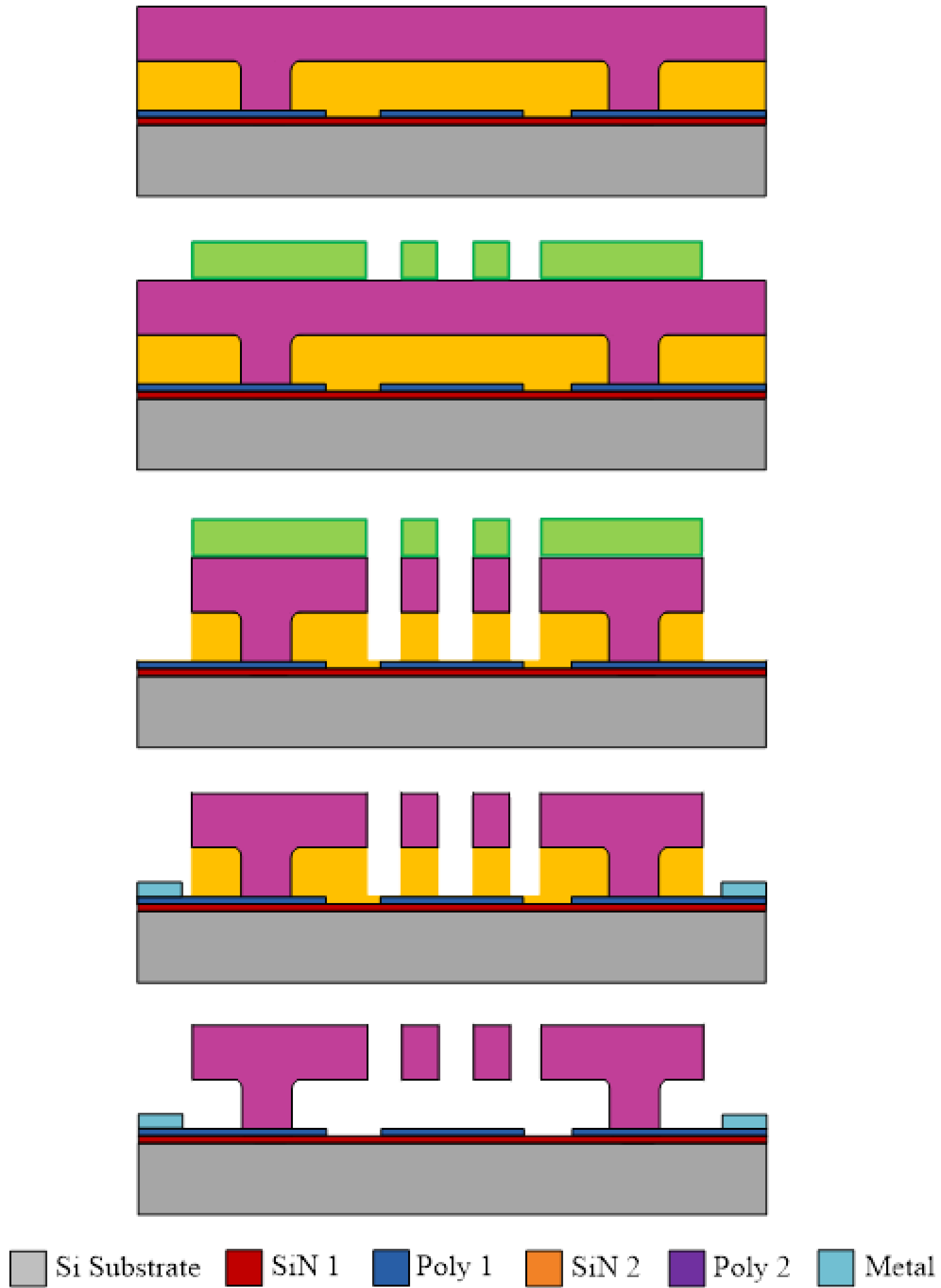

Fig. 5.20: A 3.0 µm layer of n-doped polysilicon is deposited by LPCVD followed by a 950°C / 5 min anneal. The anneal serves to activate dopants, grow grain sizes and reduce the residual stress. Then the wafer is coated with photoresist and the fourth mask level is patterned. Then Poly 2 is etched by plasma processing. After the etch is completed, the photoresist is removed and next the metal layer is deposited by lift-off patterning which does not require etching. Finally, the structure is released by immersion in BHF solution.

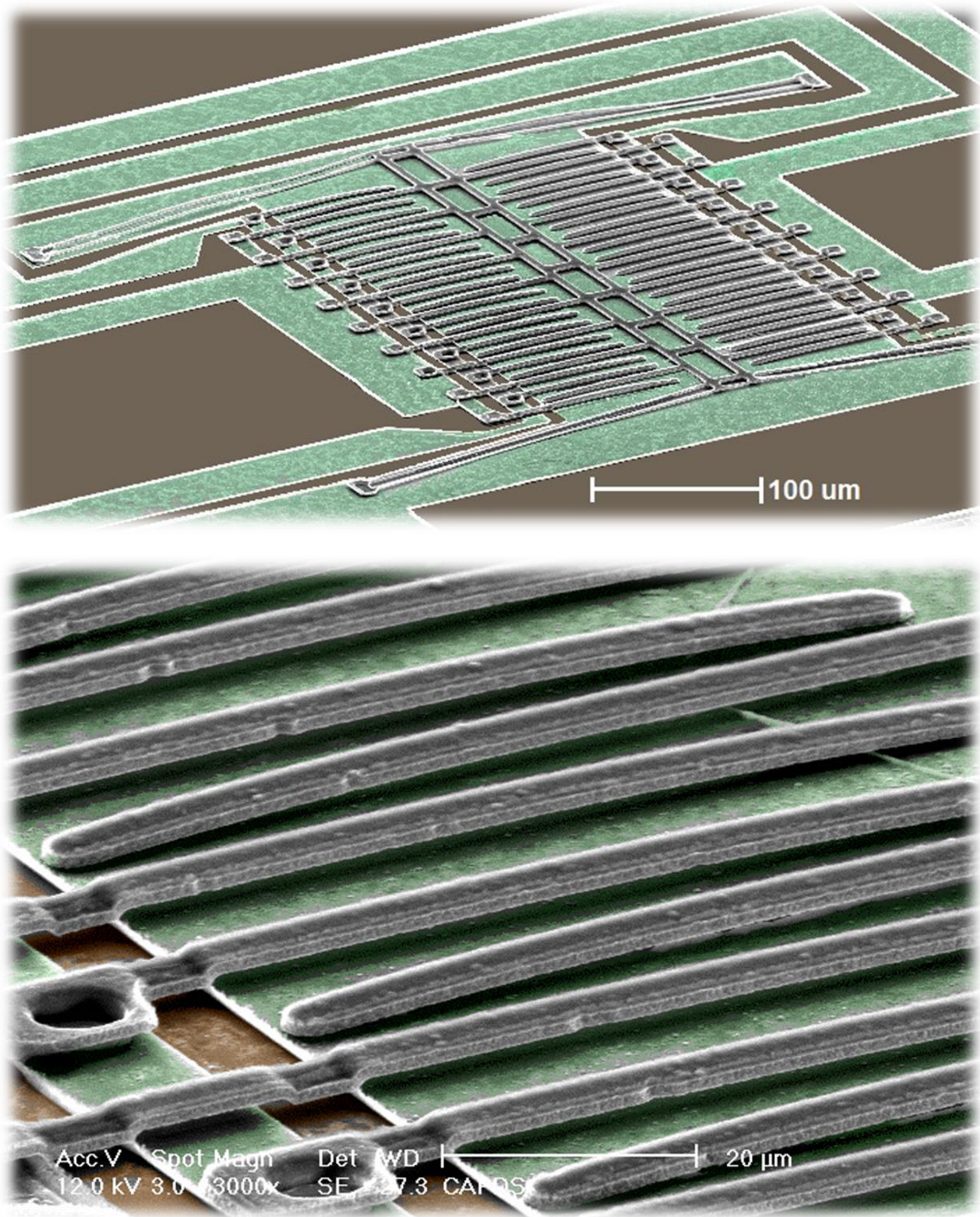

Fig. 5.21: Scanning electron micrographs of the final device (design 1)

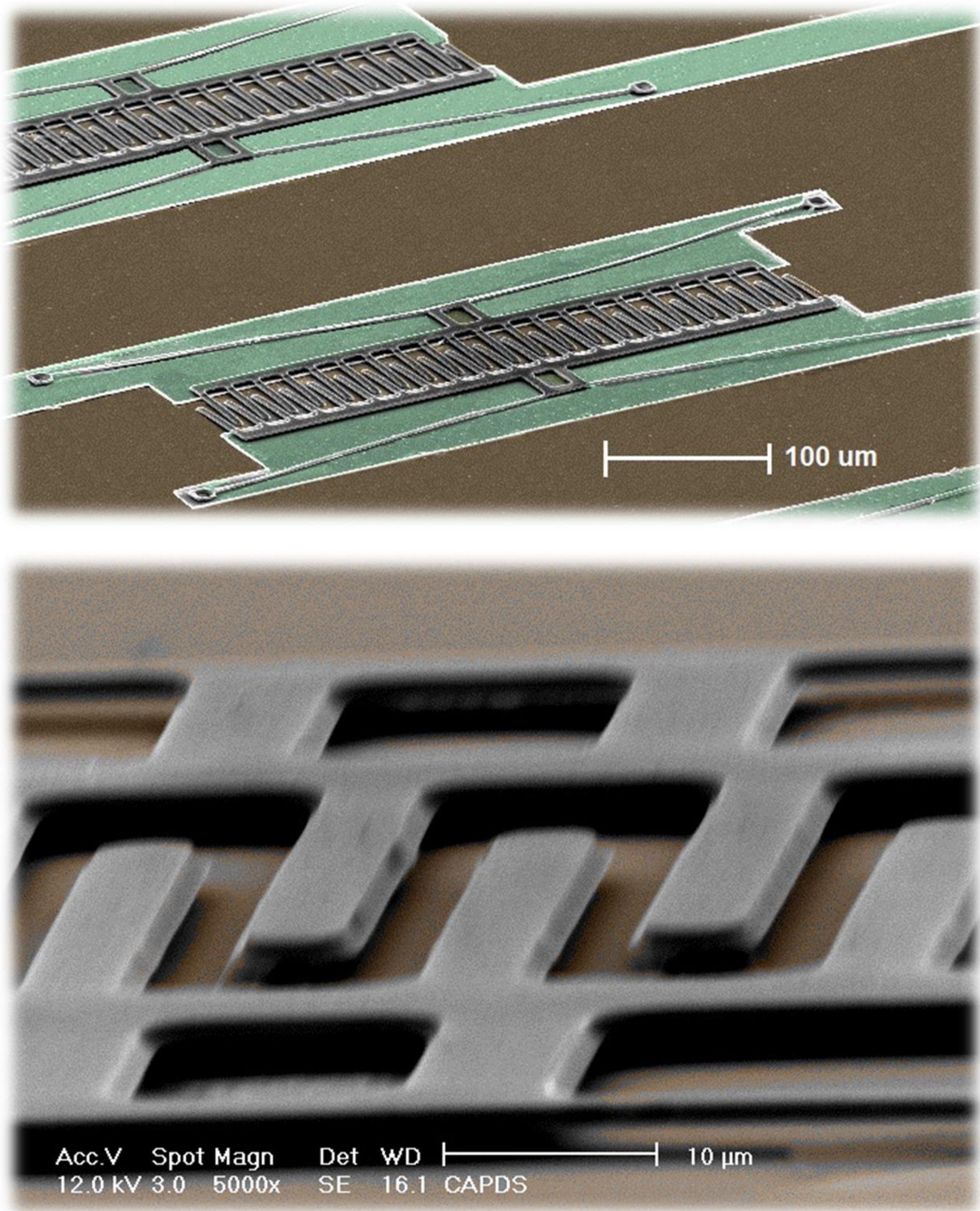

Fig. 5.22: Scanning electron micrographs of the final device (design 2)

6. Measurement and Characterization of Fabricated MEMS Sensors

6.1 Bent Cantilever Beam Test Setup

The bent cantilever beam test fixture is a standard method determining the material flexural properties, and can be used here for the strain sensor evaluation. As it is shown in Fig. 6.1, the bent beam fixture consists of a Plexiglas or silicon cantilever fixed at one end using a clamp. The beam is with length of l, width of w, and thickness of t, and a controlled displacement δ is applied at the free end using a micrometer. When a displacement is applied, the cantilever bends, thus resulting in a strain generated on the surface where the sensor is located. The MEMS sensor is bonded on the cantilever through an adhesive layer; the strain generated on the test strip surface can be efficiently transferred to the sensor with negligible loss as explained in Chapter 4. The device was firstly tested by observing the fingers movements under an optical microscope and then by capacitance measurements.

The strain generated on the beam because of tip displacement is given by [129]:

$$\varepsilon = \frac{3h(l-x)}{2L^3}\delta$$

In order to be more accurate an FEM Simulation has been also done using Comsol Multiphysics® and it was found out that sensors should not be bonded close to the clamped edge because as it shown in Fig. 6.2 the generated strain is not linear and has a distortion. Therefore, the sensor is mounted a little bit further away.

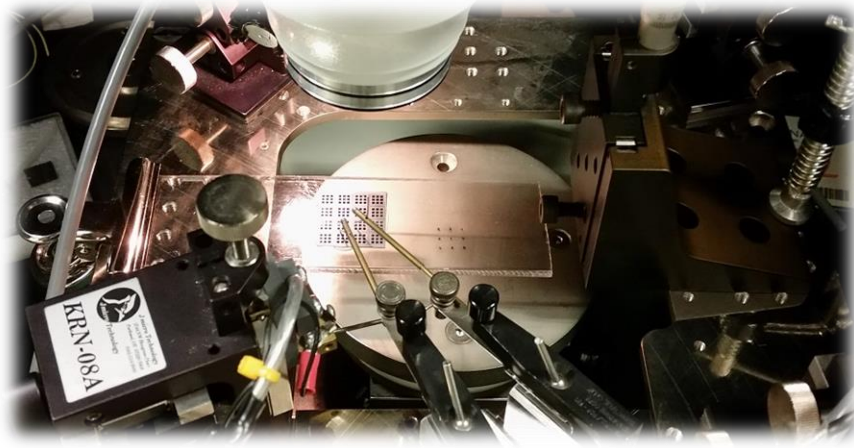

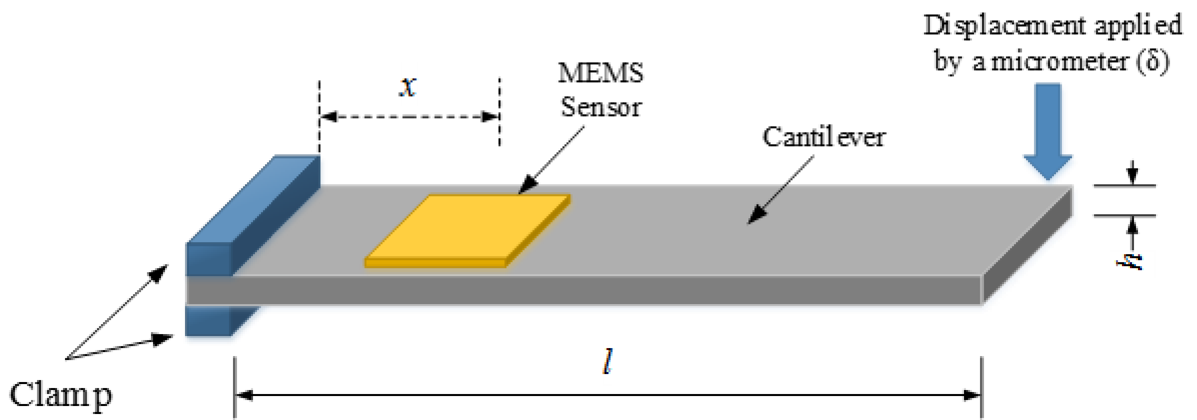

Fig. 6.1: Pictures of MEMS sensors bonded to Plexiglas and Silicon substrate in the text setup under probe station and also schematics of bent cantilever test setup.

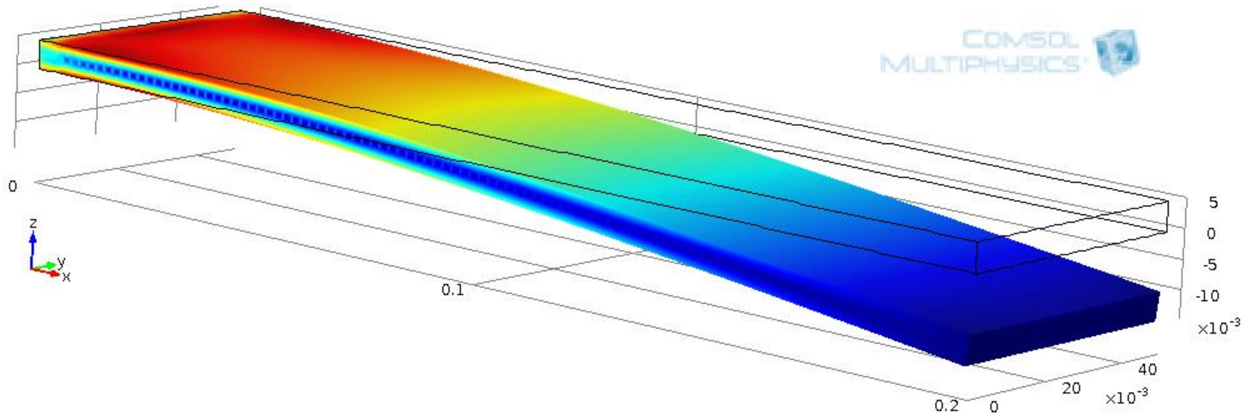

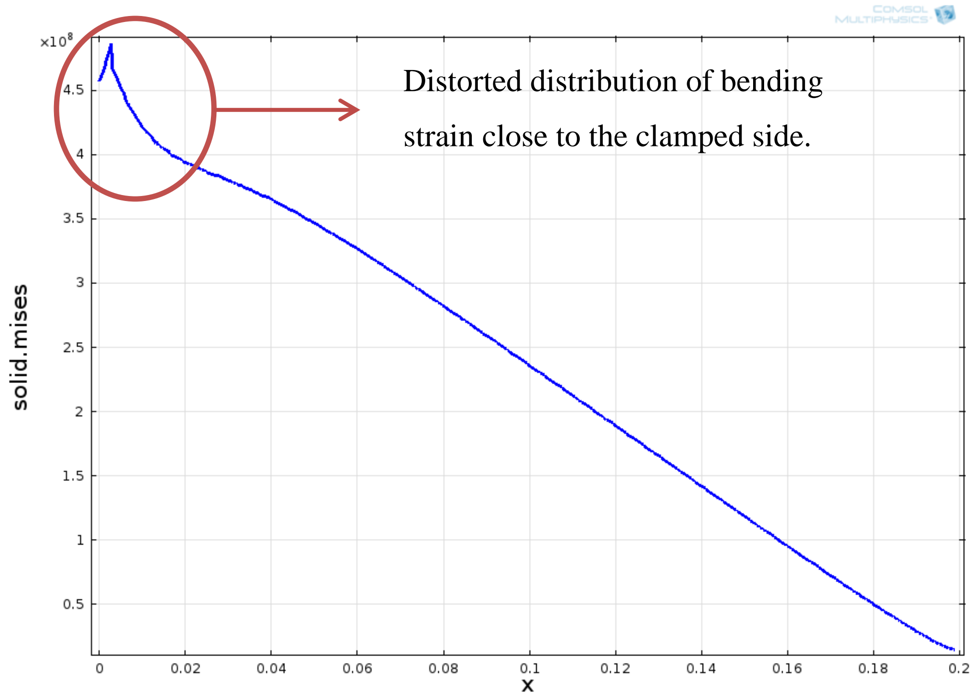

Fig. 6.2: FEM analysis of strain distribution on a cantilever beam showing the distorted distribution close to the clamped side of the beam.

6.2 Displacement Under Microscope

The same setup is installed under the optical microscope to observe the displacements of fingers.

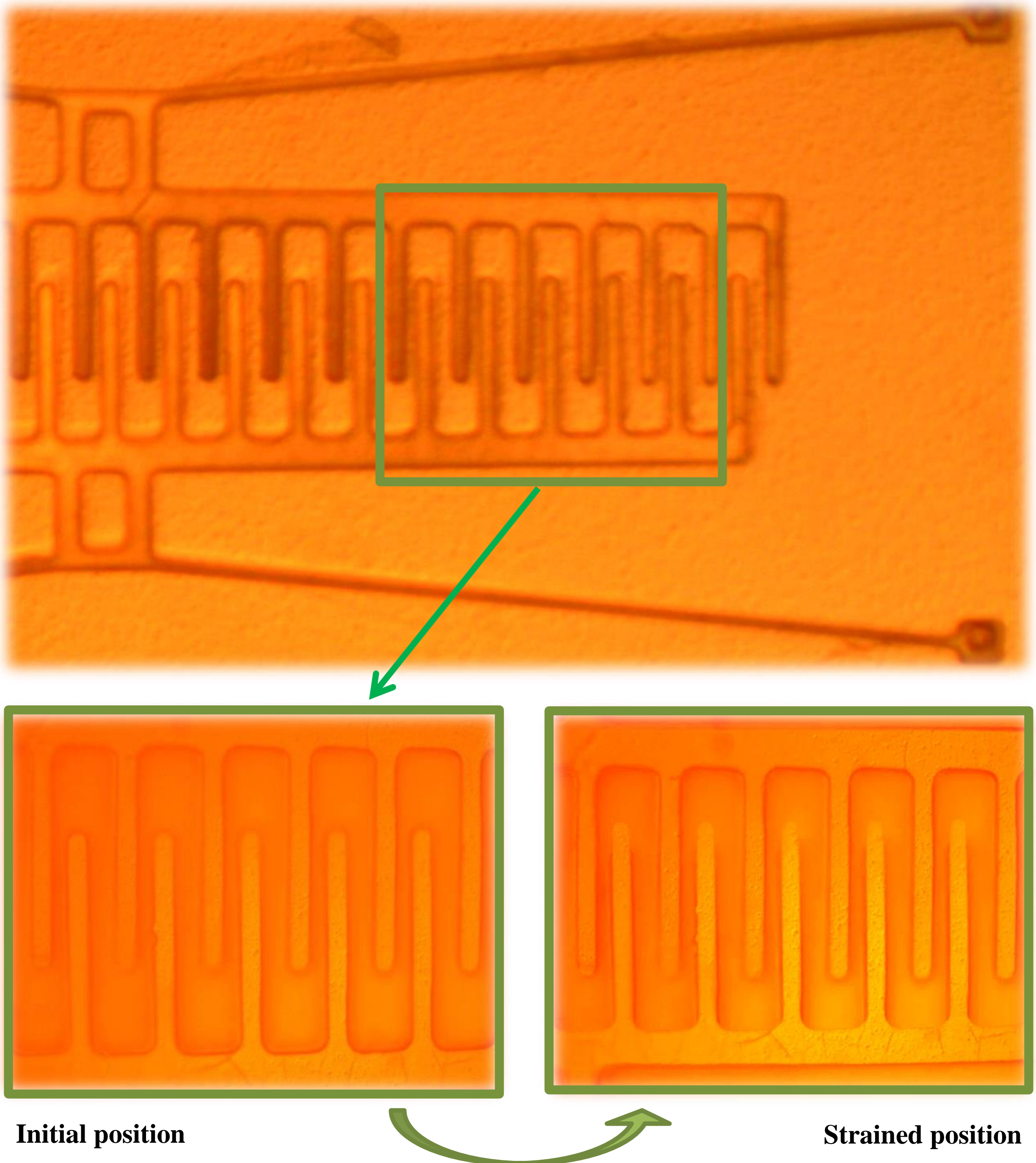

Fig. 6.3: Displacement of fingers after application of 500με of tensile strain.

6.3 Evaluation of MEMS Sensors

Fabricated MEMS sensors are bonded to a silicon cantilever using two different adhesive materials as it was shown in Fig. 6.1 and fixed on the strain measurement test setup under the probe station. Capacitance values are measured by Agilent 4279A C-V meter.

6.3.1 Strain sensors bonding and adhesive materials

Adhesive materials should be used for fixing the strain sensor to the measurement object. The bonding of the strain sensor itself is a task that requires extreme care. Only correctly mounted strain sensors can operate properly. The bonding materials hold the MEMS strain sensor firmly to the surface of the host structure and of transferring its deformation without loss to the strain gage. Various conditions and influencing variables were studied in Chapter 4. The use of adhesive materials is not the method that can be employed, spot welding and fixing with ceramic materials are also used in industry. As the results in Chapter 4 showed us, using soft adhesives and thick layers results in the strain on the strain sensor side of the layer being smaller than that on the side in contact with the host structure. However, if hard adhesives are used, i.e. adhesives with a high Young's modulus, together with a thin adhesive layer then the distortions within the layer are much smaller and are mainly restricted to the outside sections. In this case the transition distances are small and the strain transfer is correct. Strain transition occurs in three steps: from the host structure to the adhesive layer, from adhesive layer to the sensor substrate, and from the sensor substrate to the MEMS elements. Adhesion arises chiefly due to attraction forces between neighboring molecules. Therefore, increase in bonding strength was observed with moderate roughening of the surfaces. This happens because of the increase in contact area.

After cleaning the bonding surfaces and treatments, sensors are bonded to silicon cantilever beams using two different adhesive materials, wax and epoxy resin with a thickness of approximately 300 μm. Samples were left overnight to be cured. Epoxy resin is a mixture of Resin and hardener with 26 parts by weight of resin with 1 part by weight of hardener. They are mixed carefully for a few minutes and then poured on the cantilever’s surface so that no air bubbles are caught.

6.3.2 Measurement results of variable-gap design sensor

Fig. 6.4 presents the measured capacitance output versus an applied input strain of variable-gap design MEMS sensor for both adhesive materials, wax and epoxy resin. Capacitance measurements showed a small difference with the FEM simulation results due to the curvature of the electrode fingers because of residual stress and also due to non-ideal strain transfer ratio of adhesive bonding materials.

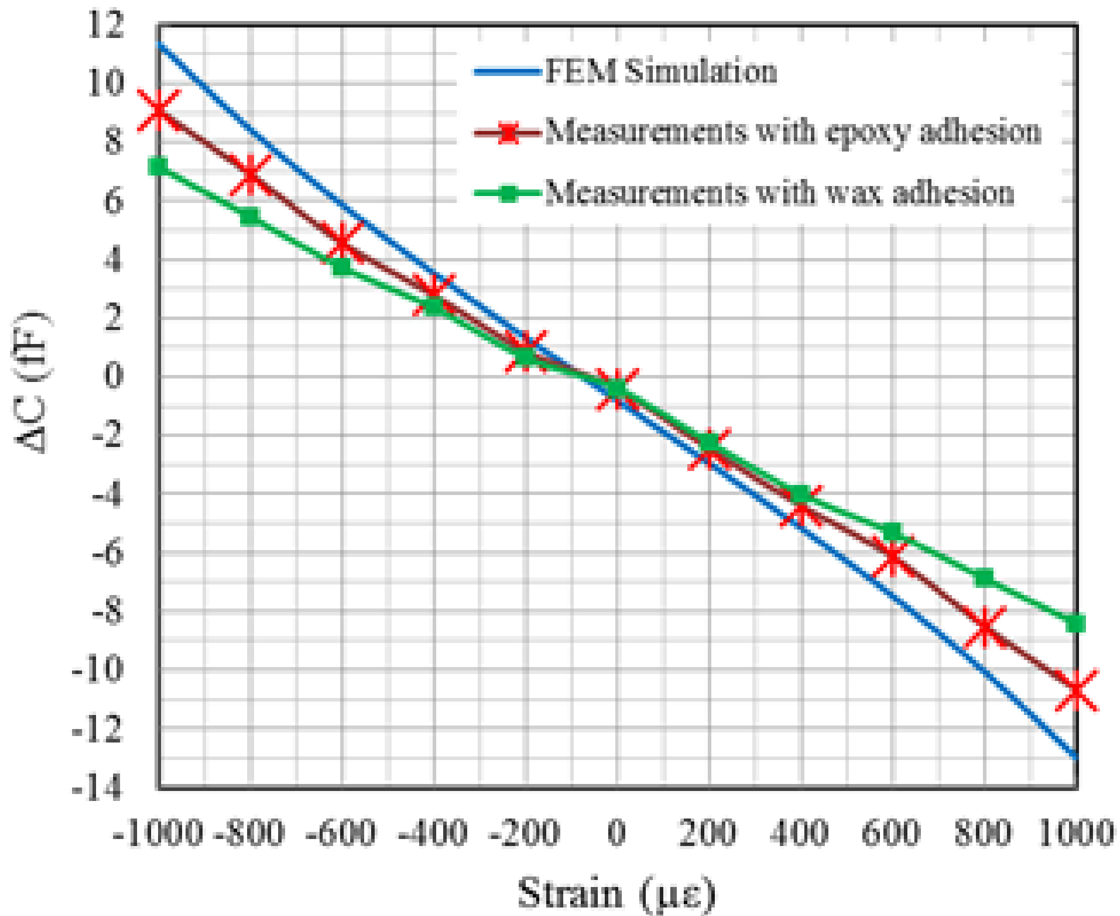

Fig. 6.4: Measured capacitance output characteristic of variable gap design sensor, bonded to the substrate using wax and epoxy adhesives.

6.3.3 Measurement results of variable-area design sensor

Fig. 6.5 presents the measured capacitance output versus an applied input strain of variable-area design MEMS sensor for both adhesive materials, wax and epoxy resin. Similar to previous case, capacitance measurements showed a small difference with the FEM simulation results due to the curvature of the electrode fingers because of residual stress and also due to non-ideal strain transfer ratio of adhesive bonding materials.

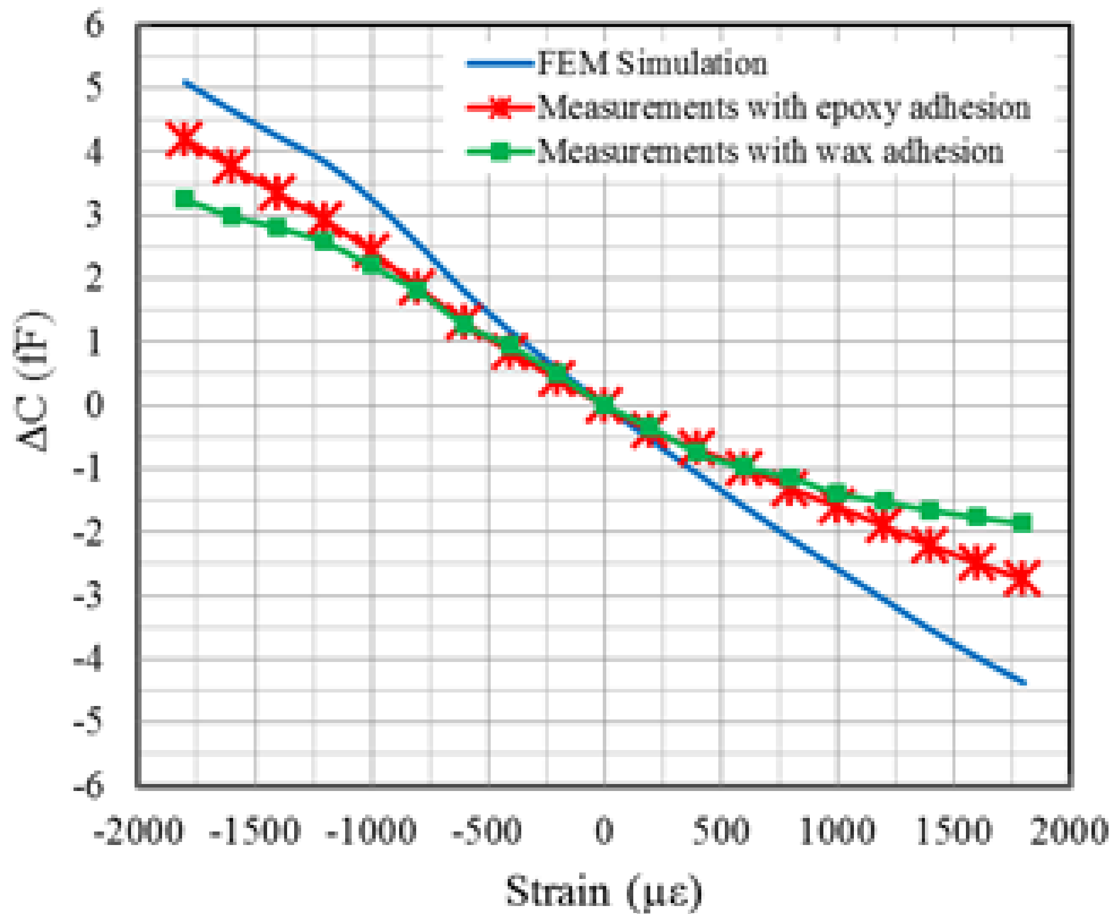

Fig. 6.5: Measured capacitance output characteristic of variable area design sensor, bonded to the substrate using wax and epoxy adhesives.

6.4 Conclusions

A bending strain test fixtures composed of a silicon cantilever, clamps and micrometers under a probe station have been developed to evaluate the performance of the designed and fabricated capacitive strain sensor. The capacitance values and changes are measured using a C-V meter. Two adhesive materials, epoxy resin and wax are used to bond the MEMS sensors to the host structure which is the silicon cantilever. Based on the measurements epoxy showed better strain transfer properties comparing to the wax. Capacitance measurements showed very good match with the FEM results. However, a small difference with the FEM simulation results exists due to the curvature of the electrode fingers because of residual stress and also due to non-ideal strain transfer ratio of adhesive bonding materials. The overall system is able to detect a minimum strain of 50 $\mu\varepsilon$ with the maximum range of up to $\pm 2000\mu\varepsilon$.

7. Development of Multisensor Approach for Reliable Management of Sensors Signals*

7.1 Introduction

Wind energy is a fast-growing sustainable energy technology and wind turbines continue to be deployed in several parts of the world. Driven by the need for more efficient energy harvesting, the size of the wind turbines has increased over the years (several MW of rated power and over 100m in rotor diameter) for both off-shore and land-based installations. Therefore, structural health monitoring (SHM) and maintenance of such turbine structures have become critical and challenging [8]. To keep the number of physical inspections to minimum without increasing the risk of structural failure, a precise and reliable remote monitoring system for damage identification is necessary. Condition-based maintenance (CBM) [5] is increasingly being used recently since it is cost-efficient and significantly improves safety compared to periodic non-destructive evaluations and visual observations [7]. CBM is performed when one or more indicators show that the structure needs maintenance. This type of maintenance necessitates a means to determine the condition of machines while in operation and involves the observation of the system by sampling dynamic response measurements from a group of sensors and the analysis of the data to determine the current state of system health. This goal is being pursued through the development of reliable sensors, and intelligent algorithms.

Although any part of the wind turbine is prone to failure [130], considerable attention is often given to the turbine blades as they are the main elements of the system. The blades could cost up to 20% of the total cost and theirs are the most expensive type of damage to repair [13]. Numerous

* Based on a published manuscript: M. Moradi and S. Sivoththaman, “MEMS multisensor intelligent damage detection for wind turbines,” IEEE Sensors Journal, vol. 15, no. 3, Jan 2015.

wind turbine blade damage detection and health monitoring techniques exist, each with its own advantages and drawbacks: Acoustic emission sensors [24], ultrasonic testing [28], thermal imaging method [29], x-ray radioscopy [30], Eddy current method [31], fiber optic (FO) sensors [25], PZT patches [32], smart materials and strain memory alloy method [33], wavelet transforms [34], and microwave techniques [35] are the key examples. The majority of these methods have limitations with regard to large-scale sensing, difficult signal interpretation, or have safety issues. FO strain sensors and particularly fibre Bragg gratings (FBGs) [26] are currently the most widely used in wind turbine structural monitoring. However, despite many advantages, there are certain limitations to the FO-based sensors too. In order to create the FO network, several interconnects are required, so implementation is challenging and probably requires surface treatment. Each sensor being wired to a central processing unit is also a drawback. A discrete network of sensors is advantageous in this case. Also, optical techniques require complex signal analysis especially for a large array of sensors. Sensor conformality is another issue as sharp bends in the FO may affect the reading. While temperature variations do not affect the optical properties, the expansion or contraction of the optical fiber could add uncertainty in attributing the signal variation to a sensed parameter. Finally, FO sensors can also be expensive for some applications [27]. With the advances in micro-electro-mechanical systems (MEMS), sensing mechanisms deploying MEMS-devices receive serious consideration due to their fast response, high accuracy, stability, and small size. MEMS sensors are cost-efficient, compatible with integration with CMOS technology for data analysis, and create discrete sensor network. These properties are attractive for reliable sensor applications in wind turbines. MEMS strain sensor design and mounting methods to ensure maximum strain transfer to the sensor is addressed elsewhere [57].

High or lasting strain can lead to crack formation, yielding, or fatigue in the structure material. When the composite structure of the wind turbine blade is under stress due to loading conditions, environmental effects and other factors, microfractures form. High stress fields then lead to bigger cracks and possibly turbine failures. Mechanisms and models for structural collapse of turbine blades have been studied [18]. Strain has historically been the main property to be observed in blade health monitoring systems [7]. Excessive strain can exacerbate the growing effects of fatigue, and passing the fracture stress threshold is dangerous. Sensing high stress fields and early detection of cracks are key for safety to reduce rehabilitation costs. Mechanical signature analysis and vibration based measurements analysis are other common techniques in structural damage

detection. They have also been recently used for condition assessment of wind turbine blades [131], [132]. Additional damage indication features would be required for more comprehensive assessment and practical health monitoring schemes often combine different analysis methods rather than relying on a single damage indicator. In a structure like a turbine blade, sensors are placed in different locations and multiple properties must be observed simultaneously. Therefore, fusing measurement data from sensors can provide robust reading and correct inferences can be drawn. Sensor data fusion is the process for combining information gathered from multiple sensors to estimate entity states [133]. Data fusion is used in several SHM techniques [134], [135] and has been tackled in different ways. The simplest method is using weighted averages of the data to obtain the fused value. Statistical methods such as Bayesian estimation [136], Kalman filtering [137], and Dempster-Shafer evidential reasoning [138] etc., are used for optimum decision making and eliminating redundant data or noise.

In this chapter, a methodology for stress level sensing and detection of cracks for wind turbine blades is presented by analyzing the distributed strain fields along the blade and natural frequencies through finite element analysis simulation for different damage scenarios. The proposed technique, using MEMS sensors, is also shown to be effective in the damage prediction in the blades. A multi sensor data fusion procedure is also proposed in this work, resulting in the design of an intelligent damage detection system that includes strain and vibration sensors, data fusion nodes, decision algorithms, and input/output cells. The proposed damage detection method represents global monitoring approach where, as opposed to local techniques, the whole blade is under surveillance so that no defect is missed and damage development is detected at the initial stage before it becomes critical.

7.2 Damage Detection Methodology

Blade strain is the most important SHM quantity for wind turbines. Different types of loads create tensile, compressive or bending stresses on wind turbine blade causing it undergo shape changes or strains. An efficient strain measurement system consisting of sensors and interface electronics is therefore desirable. Also, the sensors can be placed only in the potential damage hot spots [139], [140] and hence optimal placement of the sensors [141], [142] becomes important. The proposed

technique, in addition to detecting excessive strains, obtains strain distributions along the blade through multi-sensor data. This can be extremely helpful since strain distribution will be considerably changed in proximity of damages such as cracks, and propagating damages can be identified through changes in strain distribution. The necessary number of sensors and their spacing depend on the minimum size of damage the system is monitoring. Additionally, information on nonlinear behavior of the blade obtained from strain sensor measurements also gives good indication of how close the failure is [143].

Conventional strain gauges measure strain along a short line and not at a point. If strain field over the body is constant or linear, the measurement would be accurate. However, for the case of arbitrary strain fields, such as in turbine blades, this way of strain measurement will not be exact. FO strain sensors lack accurate point strain detection capability and are only able to detect the existence of excessive strains. In order to reduce the error introduced in certain strain fields strain sensor dimensions have to be small. Silicon micro-machined technology was used to fabricate MEMS strain sensors with micron-scale dimensions and high accuracy. A highly sensitive, MEMS-based strain sensor usable in wind turbine applications reported in previous chapters.

7.2.1 Strain distribution perturbation analysis

The effect of a crack on the strain field distribution in a blade is analyzed by considering a notch-shaped crack on the blade. As schematically shown in Fig. 7.1, the notch surface AB will not be subjected to any load making the internal strain zero on this surface, and the remaining cross section BC supports the whole load. While the strain distribution is uniform away from the notch, the lines of force become denser and cause higher strain fields in the vicinity of the notch. Consequently, the sensor readings will show a sudden decrease near the damage location and an increase beneath or at both sides of the crack location. Existence of a crack perturbs stress field distribution such that local stress must be zero at the crack boundary, and increases to the far-field stress at some distance from the crack. The distance from the damage to which the stress distribution is perturbed depends on the crack dimensions and severity of the damage. Hence this strain field distribution analysis can reliably be used for damage identification.

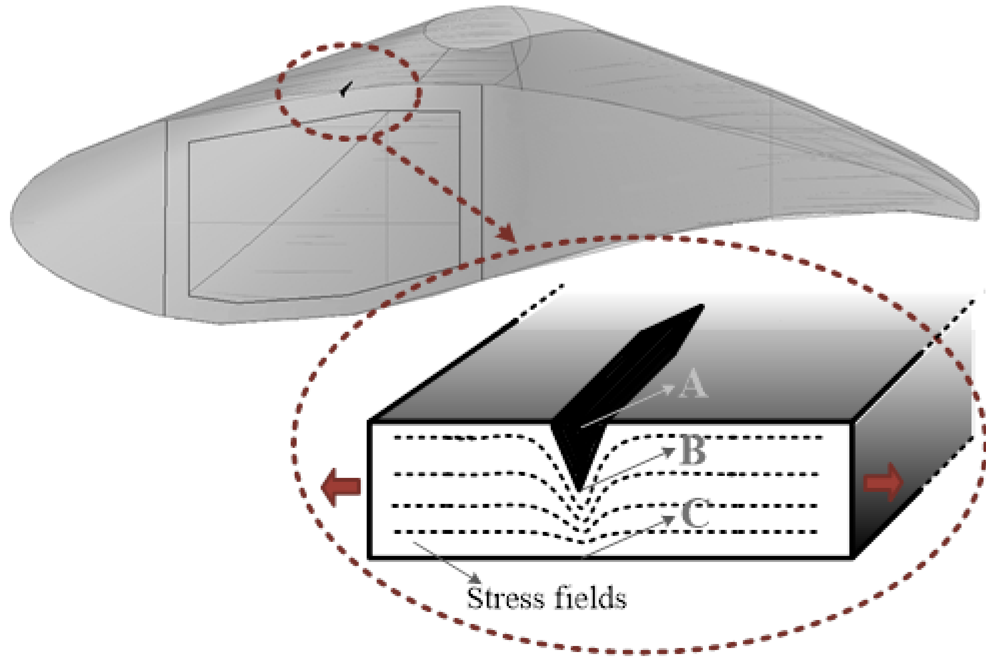

Fig. 7.1: Cross section of a wind turbine blade with a small crack of 2 cm depth and 3mm opening is implemented in the model. The inset shows how strain field distribution is disturbed due to a notch-shaped crack on the blade.

7.2.2 Natural frequency analysis

Structural damage results in a change in stiffness and damping and these changes in turn exhibit themselves in modal properties as variations in natural frequencies, mode shapes and modal damping. Measuring changes in modal parameters is a common method to localize and quantify damages in SHM systems [130]. Therefore, cracks occurring in wind turbine blade can be related to changes in natural frequencies. Strain sensors, including the MEMS strain sensor mentioned earlier, perform accurate vibration measurements too. This is one of the main reasons for proposing the combination of strain sensing and natural frequency analyses as an SHM method in this work. Due to the advances in sensor technology, we can obtain measurements relatively as accurate as 0.001 Hz for natural frequencies extracted from vibration-based measurements [144]. However, it must be noted that small damages do not cause significant modification of natural frequency. Therefore, the MEMS smart sensor with dual capability of strain and vibration sensing, simplifies the system architecture and makes it efficient and cost-effective. The multisensor fusion model, the simulation results and fusion model validation are presented in the next sections.

7.3 Multisensor Fusion Model

Data from individual sensors cannot be fully reliable and do not provide complete information. Fusing measurements data from multiple sensors enables us to make inferences that are not possible through single sensors. Incorporating data fusion into an SHM system requires the combination and integration of different diagnostic tools to improve the detection system and reduce false alarms. A monitoring system using data fusion can be composed of any number of sensors, measuring only one or different properties of the host structure and placed in different locations. In the case of SHM of wind turbine blades, in order to improve the prognostic forecasting of the system, sensors data can also be combined with structural and material properties of the blade, or even damage models. As explained in the previous section, strain fields and natural frequencies measured by MEMS sensors can efficiently be used for damage detection and localization in wind turbine blades. Combining both approaches, a multisensor data fusion procedure is proposed in this section. In addition to strain and vibration sensors, the design includes input/output cells, data fusion nodes and decision algorithms. While a complete analytical treatment of the concept is presented in this work, the implementation of the best data fusion method would also be determined by the allowable degree of complexity.

7.3.1 Fusion module for sensor validation

Internal and external noises render sensor readings uncertain and can affect the system diagnosis results. Fusing the measurements of multiple sensors can also reduce the negative effect of the noise, providing a more robust and reliable reading. Noise effects can often be reduced by applying a filter method such as least squares or Kalman filter. Kalman filter provides a method for inferring the missing information from noisy measurements and is used here in the proposed model. Obtaining accurate sensor readings of vibration and strain and analysis of their variability require the calculation of mean values. This can be estimated using a one-dimensional Kalman filter [145]. If we assume the estimated mean of sensor reading ($y_{1:k} = (y_1, y_2, \ldots, y_k)$) at time step k ($\mu_{k|k}$) follows a random walk process, then:

$$\mu_{k|k} = \mu_{k-1|k-1} + v_{k-1} \qquad (7\text{-}1)$$

where v_{k-1} is the zero-mean white with covariance Q process noise ($N(0,Q)$) at time step $k-1$. We

also suppose that the measured sensor reading at time step k is:

$$y_k = \mu_k + w_k \tag{7-2}$$

where w_k is the measurement noise ($N(0,R)$).

The Kalman filter estimates $\mu_{k/k}$ in a predictor/corrector algorithm [146], as shown in Fig. 7.2. In the prediction step, the filtered reading $\mu_{k-1/k-1}$ and its covariance matrix $\Sigma_{k-1/k-1}$ are projected to the next time step k. Therefore:

$$\mu_{k/k-1} = \mu_{k-1/k-1} \tag{7-3}$$

$$\Sigma_{k/k-1} = Q + \Sigma_{k-1/k-1} \tag{7-4}$$

In the correction step we fuse the predicted values with the measurement y_k:

$$\mu_{k/k} = \mu_{k/k-1} + K_k(y_k - \mu_{k/k-1}) \tag{7-5}$$

$$\Sigma_{k/k} = (I - K_k)\Sigma_{k/k-1} \tag{7-6}$$

$$K_k = \Sigma_{k/k-1}(\Sigma_{k/k-1} + R)^{-1} \tag{7-7}$$

Each fusion node is providing reliable mean value of the object property, $\boldsymbol{Y}$, and its variance, σ.

Natural frequencies and modal properties are global properties of the structure under monitoring. So, multiple sensors are used to determine the same property at different locations of the blade. Furthermore, each sensor output contains measurement errors and in this way sensor uncertainty can be reduced. The output of a single sensor may be misleading and others can resolve the uncertainty. Hence, for vibration sensors located at multiple locations on the blade, we should also develop the best estimate (R_v) out of n sensors reading mean values $\boldsymbol{Y} = (Y_1, Y_2, \ldots, Y_n)$. The

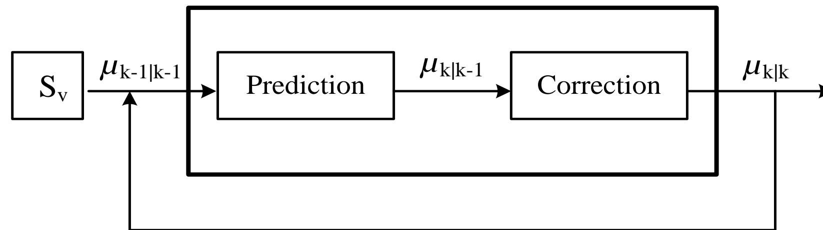

Fig. 7.1: Kalman filtering to achieve accurate estimates of sensor readings.

simplest case of fusion for a multiple sensor configuration that measures the same property is averaging, assuming that each sensor's measurement is equally reliable. If sensors readings are not equally reliable, a weighted average can be used instead.

As a fusion strategy, Bayesian statistics is often used for combining multiple sensors. Maximum likelihood is a well-known Bayesian approach [147], and its estimate, R_v is computed such that the following be maximized:

$$p(Y|R_v) = \prod_{l=1}^{n} p(Y_l|R_v) \tag{7-8}$$

By differentiating the logarithm of the likelihood and equating to zero, it can be shown that [148]:

$$\widetilde{R_v} = \frac{\sum_{l=1}^{n} C_l^{-1} Y_l}{\sum_{l=1}^{n} C_l^{-1}} \tag{7-9}$$

which is the weighted average of the sensors readings, a more accurate and reliable vibration data, and C_l^{-1} is the inverse covariance.

7.3.2 Fusion module system health diagnosis

The next step, as depicted in Fig. 7.3, is the decision algorithm fusion node that produces information about the current blade health status in the form of two variables, *I* and *C*. Of these, *I* can take up values between 0 and 1 and represents the severity of the damage, and *C* is a confidence variable associated with *I*, and can be obtained from the variances. The decision fusion node, either for strain sensors or vibration sensors, can also use data on material properties, load history etc., referred to as external knowledge in Fig. 7.3, to produce accurate indicators. Finally, in the last fusion node, alarm may be issued that the blade is damaged if I_S indicates unhealthy blade and C_S shows enough confidence, or if I_V indicates unhealthy blade and C_V shows enough confidence, or both. There would be a warning if severity indicators are below alarm threshold but higher than the warning threshold. This can be calculated either using the following criteria, or by any other voting schemes [149].

$$I_F = \begin{cases} 1 & \text{if } T_{max} \geq T_F \\ 0.5 & \text{if } T_F \geq T_{max} \geq T_W \\ 0 & \text{otherwise} \end{cases} \tag{7-10}$$

T_{max} can be calculated using any simple or complex formula. A possible simple T_{max} calculation equation can be as follows:

$$T_{max} = Max\big((I_S - T_S).(C_S - U_S), (I_V - T_V).(C_V - U_V)\big) \quad (7\text{-}11)$$

where T_S, T_V and T_F are the threshold values defined based on the desired sensitivity of the monitoring system. U_S and U_V are threshold values for acceptable reading accuracy confidence.

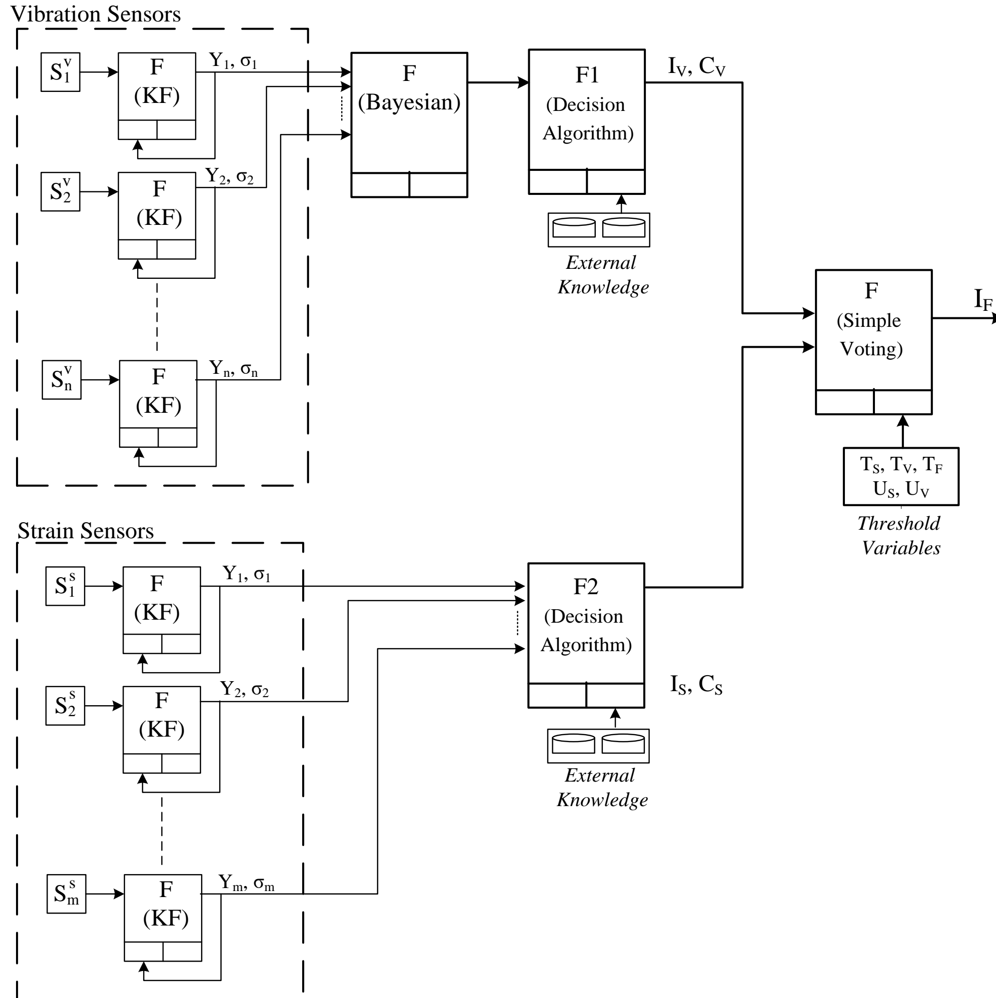

Fig. 7.2: The operation of the proposed intelligent wind turbine damage detection system. Strain and vibration sensors (Si) send their reliable measurements through some data fusion nodes to F_1 and F_2 which outputs the variables *I* and *C*. *I*, a number between 0 and 1, indicates damage severity and *C*, a confidence variable associated with *I*, which can be obtained from the variances. The cell F receives (I_S, C_S) and (I_V, C_V) as input data and generates the decision signal I_F as output. The thresholds variables can be calculated using a history models or experiments and are regarded as external knowledge.

7.4 Simulation and Results

A full-scale finite element model for wind turbine blade has been developed in COMSOL Multiphysics®. A typical blade geometry of 33.25m in length and 2.8m maximum chord at 25% of the length [150] is used for the model. The material is taken to be E-glass composite with Young's modulus of 48 GP [151]. Fig. 7.4 shows a finite element mesh of the blade, generated by the program and also the blade cross section as inset. The major sources of loads on the turbine blades are the aerodynamic force, the centrifugal forces, the inertial force (during shutdown and start-up), weight, and other intermittent forces. The aerodynamic forces are of two types; the drag force almost in the horizontal direction along the wind direction and the lift force in the vertical plane. These forces are functions of wind speed, pitch angle, and rotation speed. They also depend on operational conditions [17]. For the model, the blade is assumed to be operating steadily at 30 rpm at a wind speed of 10 m/s. The blade weight force is constant, but the force vector with respect to the blade changes during rotation. The centrifugal force on the other hand is always along the blade with its magnitude depending on rotation speed. For the used blade model with the weight of 4733 kg, centrifugal force works out to about 185,000 N.

7.4.1 Finite element method model

The model simulation carried out for a structurally healthy blade is illustrated in Fig. 7.5, showing the stress distribution and the tip deflection. The maximum von Mises stress was 680 MPa and the blade tip deflection was 20 cm in the z-direction. Since deflection is large and may result in nonlinear behavior, geometrical nonlinear analysis was required in the simulation. Also, the effect of the centrifugal force creating a restoring force on the deflecting blade is ignored. In the following, details of the finite element simulation of blades suffering from cracks with different severities and locations are presented.

7.4.2 Effect of damage on strain fields

Fig. 7.6 shows the simulation output for a damaged blade model with a 3mm-wide crack with 2cm depth. The stress field distribution perturbation is clearly visible due to the existence of a crack. Stress fields return to normal at some distance from the crack. The distance from the damage to which the stress distribution is perturbed depends on the crack dimensions and severity of damage.

Fig. 7.7 accurately shows the strain distribution in vicinity of the crack from simulation results of healthy and damaged blades. In the damaged blade, sudden decrease of strain magnitude is easily detectable even at locations as far as 1 meter on either side of the crack. Hence, sensors located with at least 2 meters spacing would be able to detect such cracks in a blade under the load explained in previous section. The strain magnitude at the corner sides of the crack is graphed in Fig. 7.6, showing the sudden increase of strain on the corner sides of the crack. This important result underlines the usefulness of strain field analysis in determining the configurations for sensor deployment. However, various damage scenarios and load conditions [152], should be taken into account to determine the optimum placement of sensors in a cost-effective way, without compromising sensitivity.

7.4.3 Effect of damage on natural frequencies

Finite element method analysis has been carried out again to investigate the effect of cracks on natural frequencies. Five different scenarios are considered; two undamaged (U_{1-2}) and three damaged (D_{1-3}). U_1 and U_2 represent the cases when the rotor is parked with no wind load on the

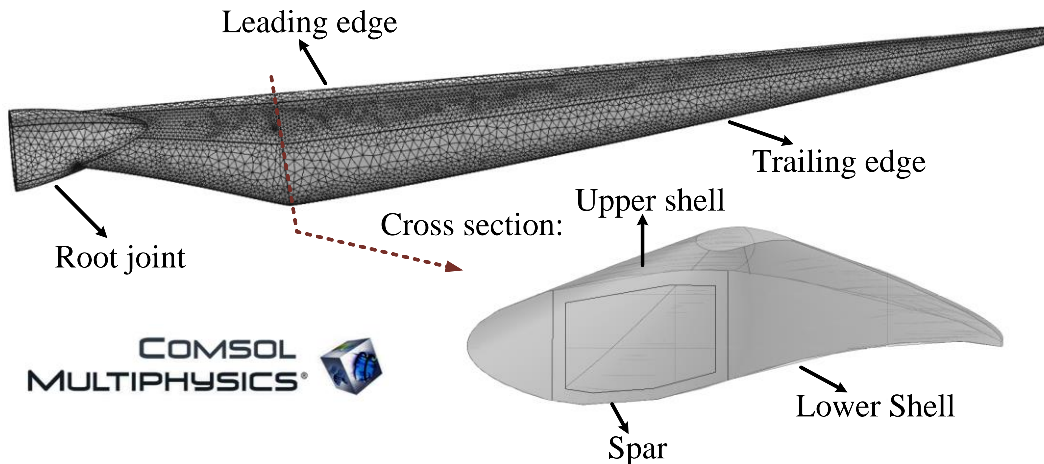

Fig. 7.4: The generated mesh and the finite element model of the blade used for COMSOL simulations.

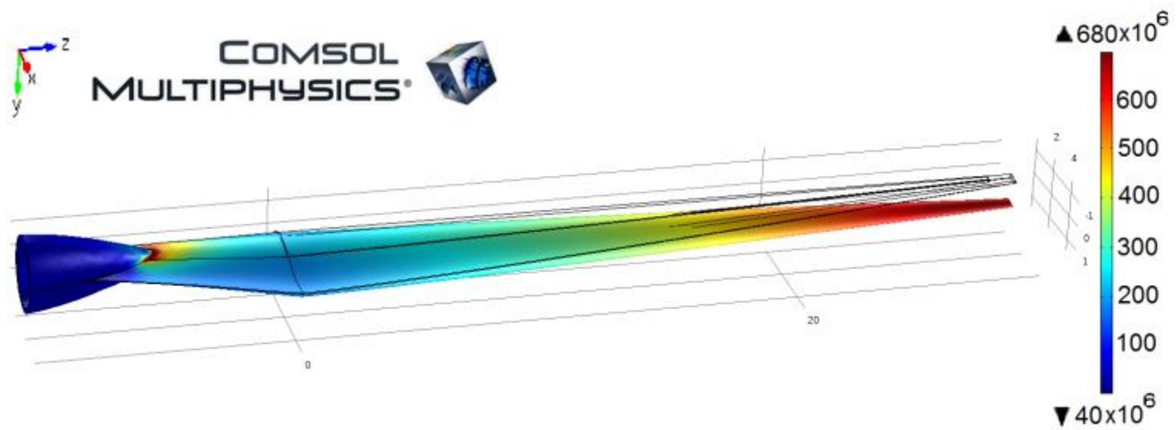

Fig. 7.5: Simulation of stress distribution and deflection of a healthy blade. In this particular case, the tip of the blade is deflected about 20cm.

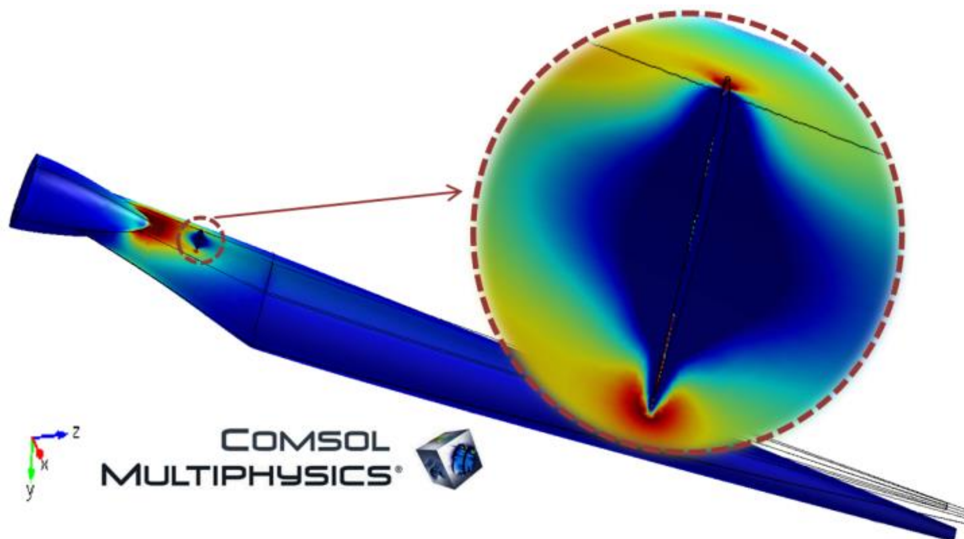

Fig. 7.6: FEM simulation output showing the variation in stress fields of a damaged blade model. The inset shows sudden decrease around the damage location and increase beneath or at both corner sides of the crack.

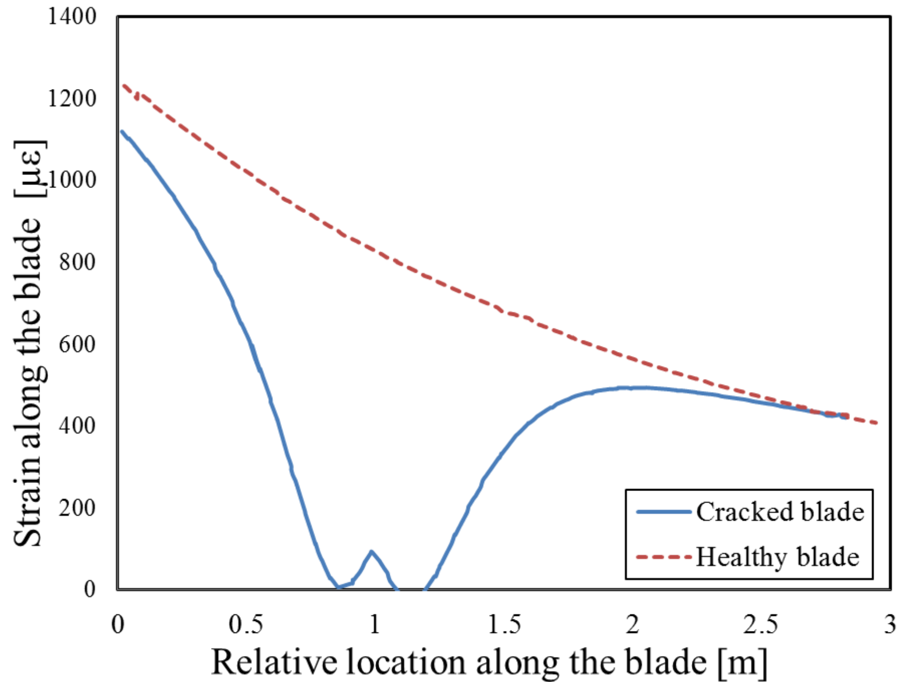

Fig. 7.7: Strain in vicinity of the crack for two cases of healthy and damaged blades. Sudden decrease of strain magnitude is detectable even at locations as far as more than 1 m on each side of the crack. The inset graph shows strain magnitude at the upper corner side of the crack.

blade, and when the blade is rotating therefore subjected to centrifugal loads respectively. In the damaged scenarios, D_1 represents the structure with the small crack treated in subsection B (Fig. 7.6), D_2 a worse crack (1mm wider and deeper) at the same place, and D_3 same as D_1 but at a location with low stress fields, therefore less critical. Each case is carefully simulated in COMSOL Multiphysics®. Natural frequencies of the first ten modes obtained for the five different scenarios are presented in Table 7.1. Comparing the results for U_1 and U_2, it can be seen that applied stress, due to wind load or rotation, does not create a sensible variation in natural frequencies of the structure. So, we can deduce that different wind conditions or rotation speeds do not cause significant frequency change. On the other hand, the presence of damage in the structure causes a decrease in the natural frequencies in all damage cases ($D_{1\text{-}3}$), with very few exceptions. Severity is higher when the crack is bigger (D_2) or is located at higher stressed regions (D_1 vs. D_3). Overall, it is clear that the change is more pronounced in severe cases which are more dangerous. This analysis shows that monitoring the shift in natural frequencies can be a useful tool in SHM of turbine blades.

Table 7.1: Natural frequency (Hz) comparison between undamaged (U1-2) and damaged (D1-3) states (Percentage changes wrt U_2 are shown in square brackets)

M	U_1	U_2	D_1	D_2	D_3
1	0.8220	0.8236	0.8191 [0.546]	0.8136 [1.219]	0.8230 [0.074]
2	2.4119	2.4125	2.4103 [0.091]	2.4087 [0.157]	2.4130 [0.020]
3	3.1777	3.1789	3.1717 [0.223]	3.1700 [0.278]	3.1771 [0.056]
4	6.8730	6.8741	6.8623 [0.171]	6.8607 [0.195]	6.8674 [0.097]
5	11.4057	11.4063	11.3695 [0.323]	11.3345 [0.629]	11.4004 [0.052]
6	12.3186	12.3189	12.3061 [0.104]	12.3039 [0.121]	12.3153 [0.029]
7	13.5927	13.5937	13.5544 [0.290]	13.5188 [0.551]	13.5816 [0.089]
8	19.5327	19.5340	19.4977 [0.186]	19.4777 [0.288]	19.5202 [0.070]
9	25.5493	25.5494	25.5481 [0.005]	25.5364 [0.051]	25.5453 [0.016]
10	27.9317	27.9331	27.8741 [0.211]	27.8361 [0.347]	27.9294 [0.013]

7.5 Multisensor Fusion Model Validation

In this section, we perform simulation of the proposed architecture for system health diagnosis. The process flow chart of sensor validation and damage detection reasoning based on fusion algorithm explained in Section III is shown in Fig. 7.8. Based on this flow chart, four possible scenarios are simulated in Matlab®. Fig. 7.9 shows the mean values of the output signals of three neighbor strain sensors at 20 reading times, and the global estimation of the simulated vibration sensors signal shift. The sensors output signal variances are used to calculate confidence values. The last three graphs show the strain sensors based damage severity indicator, I_S, vibration sensors based damage severity indicator, I_V, and I_F which is the final decision indicator calculated based on I_S, I_V, and their confidence values. Depending on the value of I_F, we can have healthy blade condition ($I_F = 0$), damage warning ($I_F = 0.5$), or damaged blade alarm ($I_F = 1$).

Four scenarios are studied:

1) *Healthy condition (Reading time 1 to 5)*

   Strain sensors show smooth variation of strain distribution based on their locations and vibration frequency shift is very low. Therefore, indicators show healthy status.

2) *Damage Warning (Reading time 11 to 15)*

Both strain sensors and vibration signals show very small perturbation which is less than the threshold or with low confidence values which causes only a warning condition.

3) *Damage Blade Alarm (Reading time 6 to 10)*

Although strain sensors show normal condition but vibration frequency shift is more than threshold which causes the final decision indicator goes to one and sounds damage blade condition alarm.

4) *Damaged Blade Alarm (Reading time 16 to 20)*

Both strain sensors signal and vibration signal indicates existence of a damage which produces a status of damaged blade alarm.

7.6 Conclusions

A new methodology to nondestructively locate and estimate the severity of damage in wind turbine blade structures has been presented. The method is based on strain field distribution analysis combined with natural frequency variation detection which provides global as well as local information on structural health condition. The proposed technique does not require direct human accessibility to the structure, is cost effective, easy to operate, and has the enhanced capability for real-time damage detection. A major advantage of this method is that it uses one type of sensor, a MEMS strain sensor, to measure both vibration and strain signals and leads to accurate readings and much less noise. From the simulation results, we demonstrated that the proposed technique was successful in the turbine blade damage detection under various scenarios. Another advantage of this method is that it can be implemented without the detailed knowledge of material properties or prior models and responses. One of the challenges of the technique is the ability to identify minor cracks or to differentiate the type of damages on composite structures. Delamination and other possible damage models should be also studied. A viable method for signal extraction should also be implemented. Finally, it should be mentioned that the presented method is good enough and applicable to identify defects in other structural parts of the wind turbine as well such as the tower or any other structure where there is no knowledge of its prior state.

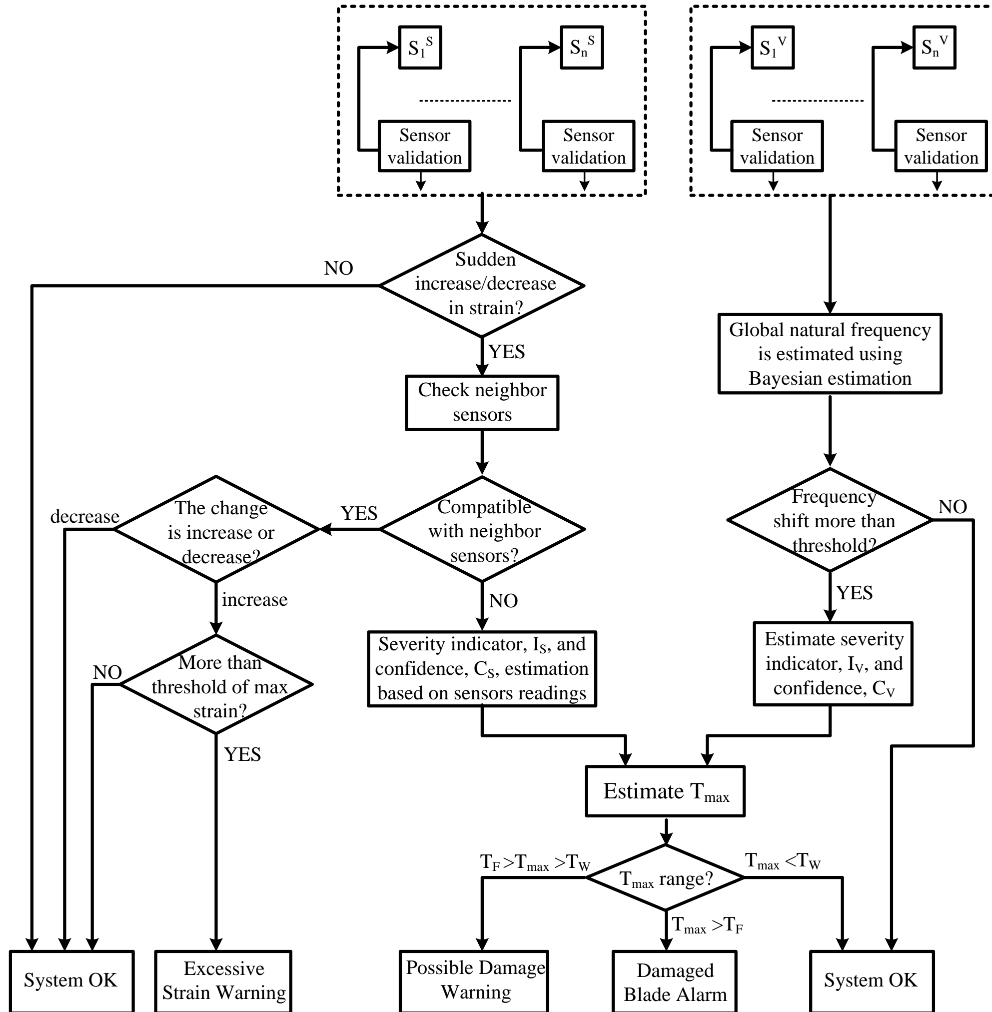

Fig. 7.8: Sensor validation and damage detection reasoning process map.

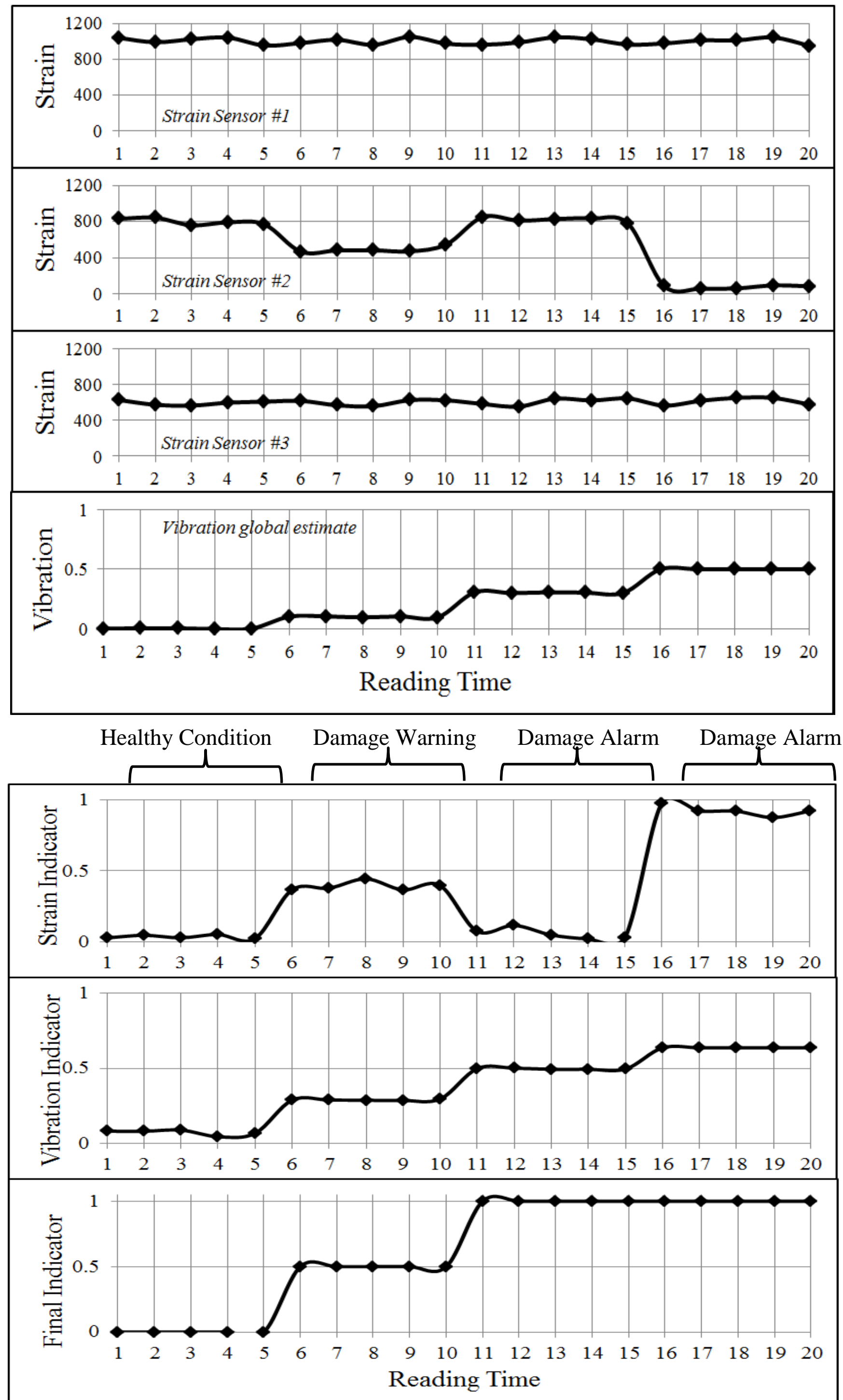

Fig. 7.9: Simulation results for the suggested possible multisensor damage detection architecture. First three graphs are the output signals of three neighbor strain sensors. The next graph is the calculated vibration frequency shifts and last three graphs show the strain sensors based damage severity indicator, I_S, vibration sensors based damage severity indicator, I_V, and I_F which is the final decision indicator.

8. Conclusions

In this thesis, a reliable damage detection approach based on MEMS technology for wind turbine blades is proposed and studied. Although the main part of the study is dedicated to the sensor design, modelling and fabrication, but it looked at the feasibility of the damage detection method systematically too.

Damage and failure can happen at any part of a wind turbine and stress, fatigue, wind gusts, moisture, corrosion and even lightning strikes are the main causes of wind turbine structural damages. Although damage at any component is important, considerable attention has been given to the blades as they are the main elements of the system. Damage to a blade can occur in various ways but they can be extensively avoided by developing successful health monitoring method which sensing technology and the associated signal interpretation algorithms are the essential factors. Among various parameters causing the damage, the most important ones which are blade strain was the subject of this research work. MEMS based sensors are very attractive among other sensing principles and techniques due to different advantages such as high sensitivity, low noise, better scaling characteristics, low cost and higher potential for integration with low power CMOS circuits. Conventional strain sensors based on piezoelectric elements or metal foils are inadequate for high performance and low cost applications due to their large temperature dependence, lower sensitivity, and incompatibility to standard CMOS integration. Therefore, MEMS technology was selected in this work to realize a reliable blade strain sensor.

Two new designs of linear and sensitive MEMS strain sensors were presented. The proposed structures use two pairs of bent beams (or Chevron beams) to achieve higher resolution and sensitivity by mechanically amplifying the displacement created by the applied strain. An analytical model was also developed to predict the deflection behavior of the beams using elliptic integrals, and its accuracy was verified by FEM simulations which showed excellent agreement.

FEM analysis of the comb-drive based designs of variable-gap and variable-area sensor structures showed a capability of measuring strain with resolution of 82 με/fF and 380 με/fF, while demonstrating a maximum strain range of ±1000 με and ±1800 με, respectively. The proposed designs are not complicated and can be realized using standard MEMS fabrication techniques.

A simple formulation was proposed to understand the transmission of strain fields from the host structure to the bonded strain sensor. A verified with FEM analytical model was created to quantify the strain transmission loss due to the interfacial adhesive layer. The solution quantifies the influence of the material parameters on the overall strain transmission ratio and can be used for calibration and evaluation of the sensors even at the design level. The sensitivity of the gauge factor on the adhesive layer thickness has been established, and it is found that smaller sensor dimensions lead to increased sensitivity.

The most important part of this work was the fabrication of the designed sensor structures. A MEMS surface machining fabrication procedure was developed from scratch in our lab. The development also involved silicon nitride and polycrystalline material study, characterization and development. The MEMS fabrication process has five layers. SiN isolation layer, polysilicon interconnection layer, SiN sacrificial layer, polysilicon structural layer, and the metal contact pads. This process can be used for fabrication of any other MEMS structure designs as well. The developed fabrication process was used to realize the designed sensor structures and is the main contribution of this thesis.

A bending strain test fixtures have been developed to evaluate the performance of the designed and fabricated capacitive strain sensors. The overall system is able to detect a minimum strain of 50 με with the maximum range of up to ±2000με. Two different adhesive bonding materials were used to bond the sensor substrate to the cantilever beams. Epoxy showed better strain transfer properties comparing to wax.

Finally, a new methodology to nondestructively locate and estimate the severity of damage in wind turbine blade structures was proposed. The method was based on strain field distribution analysis combined with natural frequency variation detection which provides global as well as local information on structural health condition. The proposed technique does not require direct human accessibility to the structure, is cost effective, easy to operate, and has the enhanced

capability for real-time damage detection. A major advantage of this method is that it uses one type of sensor, a MEMS strain sensor, to measure both vibration and strain signals and leads to accurate readings. From the simulation results, we demonstrated that the proposed technique was successful in the turbine blade damage detection under various scenarios. Another advantage of this method is that it can be implemented without the detailed knowledge of material properties or prior models and responses. The presented method is applicable to identify defects in other structural parts of the wind turbine or any other structure where there is no knowledge of its prior state.

Bibliography

[1] "Annual Market Update 2014 Global Wind Report," Global Wind Energy Council (GWEC), 2014.

[2] H. N. Li, D. S. Li and G. B. Song, "Recent applications of fiber optic sensors to health monitoring in civil engineering," *Engineering structures,* vol. 26, no. 11, pp. 1647–1657, 2004.

[3] C. R. Farrar and K. Worden, "An introduction to structural health monitoring," *Philos. Trans. R. Soc. A—Math. Phys. Eng. Sci.,* vol. 365, no. 1851, p. 303–315, 2007.

[4] D. Li *et al.*, "A review of damage detection methods for wind turbine blades," *Smart Materials and Structures,* vol. 24, no. 3, p. 033001, 2015.

[5] B. K. N. Rao, Handbook of Condition Monitoring, Oxford, U.K.: Elsevier, 1996.

[6] B. Al-Najja, "Total quality maintenance an approach for continuous reduction in costs of quality products," *Journal of Quality in Maintenance Engineering,* vol. 2, no. 3, p. 4–20, 1996.

[7] I. Alsyouf, "The role of maintenance in improving companies productivity and profitability," *International Journal of Production Economics,* vol. 105, no. 1, p. 70–78, 2007.

[8] C. C. Ciang, J. Lee and H. Bang, "Structural health monitoring for a wind turbine system: a review of damage detection methods," *Meas. Sci. Technol.,* vol. 19, no. 12, p. 122001, 2008.

[9] C. Kong, J. Bang and Y. Sugiyama, "Structural investigation of composite wind turbine blade considering various load cases and fatigue life," *Energy,* vol. 30, no. 11, p. 2101–2114, 2005.

[10] M. M. Shokrieh and R. Rafiee, "Simulation of fatigue failure in a full composite wind turbine blade," *Compos. Struct.,* vol. 74, no. 3, p. 332–342, 2006.

[11] M. L. Flemming and S. Troels, "New lightning qualification test procedure for large wind turbine blades," in *Int. Conf. Lightning and Static Electricity*, Blackpool, UK, 2003.

[12] B. Hahn, M. Durstewitz and K. Rohrig, "Reliability of Wind Turbines Experiences of 15 Years with 1,500 W (ed. J. Peinke *et al*, Berlin: Springer)," in *Wind Energy (ed. J Peinke et al.)*, Berlin, Springer, 2007, p. 329–32.

[13] M. M. Khan, M. T. Iqbal and F. Khan, "Reliability analysis of a horizontal axis wind turbine," in *IEEE 14th NECEC conference*, Newfoundland, Canada, 2004.

[14] "Wind Turbine Accident Data to December 31st 2005," Caithness Windfarm Information Forum, [Online]. Available: http://www.caithnesswindfarms.co.uk/.

[15] B. F. Sørensen *et al.*, "Fundamentals for remote structural health monitoring of wind turbine blades—a preproject," Risø-R-1336(EN) Report Risø National Laboratory, Denmark, 2002.

[16] "Industrial wind action," 2012. [Online]. Available: www.windaction.org.

[17] A. Hemami, Wind Turbine Technology, Clifton Park: Cengage Learning, 2012.

[18] L. C. T. Overgaard, E. Lund and O. T. Thomsen, "Structural collapse of a wind turbine blade. Part A: Static test and equivalent single layered models," *Composites Part A: Applied Science and Manufacturing,* vol. 41, no. 2, p. 257–270, 2010.

[19] E. R. Jørgensen *et al.*, "Full scale testing of wind turbine blade to failure—flapwise loading," Risø-R-1392(EN) Report Risø National Laboratory, Denmark, 2004.

[20] Z. Hameed *et al.*, "Condition monitoring and fault detection of wind turbines and related algorithms: A review," *Renewable and Sustainable energy reviews,* vol. 13, no. 1, p. 1–39, 2009.

[21] M. J. Sundaresan, M. J. Schulz and A. Ghoshal, "Structural health monitoring static test of a wind turbine blade," National Renewable Energy Laboratory, CO, USA, 2002.

[22] H. Bang, M. Jang and H. Shin, "Structural health monitoring of wind turbines using fiber bragg grating based sensing system," in *Proc. of Sensors and Smart Structures Technologies for Civil, Mechanical, and Aerospace Systems 2011*, San Diego, California, USA, 2011.

[23] M. J. Schulz and M. J. Sundaresan, "Smart Sensor System for Structural Condition Monitoring of Wind Turbines," National Renewable Energy Laboratory, 2006.

[24] A. Ghoshal *et al.*, "Health monitoring of composite plates using acoustic wave propagation, continuous sensors and wavelet analysis," *J. Reinforced Plastics Composites,* vol. 26, no. 1, p. 95–112, 2007.

[25] J. M. López-Higuera, L. R. Cobo, A. Q. Incera and A. Cobo, "Fiber optic sensors in structural health monitoring," *J. Lightw. Technol.,* vol. 29, no. 3, p. 587–608, 2011.

[26] K. Schroeder *et al.*, "A fibre Bragg grating sensor system monitors operational load in a wind turbine rotor blade," *Meas. Sci. Technol.,* vol. 17, no. 5, p. 1167, 2006.

[27] R. M. Measures, Structural monitoring with fiber optic technology, Academic Press, 2001.

[28] S. E. Burrows, A. Rashed, D. P. Almond and S. Dix, "Combined laser spot imaging thermography and ultrasonic measurements for crack detection," *Nondestructive Testing and Evaluation,* vol. 22, no. 2–3, p. 217–227, 2007.

[29] R. Haj-Ali, B. S. Wei, S. Johnson and R. El-Hajja, "Thermoelastic and infrared-thermography methods for surface strains in cracked orthotropic composite materials," *Eng. Fract. Mech.,* vol. 75, no. 1, p. 58–75, 2008.

[30] E. Jasinien *et al.*, "NDT of wind turbine blades using adapted ultrasonic and radiographic techniques," *Insight-Non-Destructive Testing and Condition Monitoring,* vol. 51, no. 9, p. 477–483, 2009.

[31] J. Bowler and M. Johnson, "Pulsed eddy-current response to a conducting half-space," *IEEE Trans. Magn.,* vol. 33, no. 3, p. 2258–2264, 1997.

[32] G. Park, H. Sohn, C. R. Farrar and D. J. Inman, "Overview of piezoelectric impedance-based health monitoring and path forward," *Shock Vib. Dig.,* vol. 35, no. 6, p. 451–464, 2003.

[33] B. Verijenko and V. Verijenko, "The use of strain memory alloys in structural health monitoring systems," *Compos. Struct.,* vol. 76, no. 1, p. 190–196, 2006.

[34] C. Tsai, C. Hsieh and S. Huang, "Enhancement of damage-detection of wind turbine blades via CWT-based approaches," *IEEE Trans. Energy Conversion,* vol. 21, no. 3, p. 776–781, 2006.

[35] S. Kharkovsky *et al.*, "Millimeter wave detection of localized anomalies in the Space Shuttle external fuel tank insulating foam," *IEEE Trans. Instrum. Meas.,* vol. 55, no. 4, p. 1250–1257, 2006.

[36] J. W. Dally and W. F. Riley, Experimental Stress Analysis 3rd Ed., New York: McGraw-Hil, 1991.

[37] K. Hoffmann, An Introduction to Measurements Using Strain Gages, Darmstadt: Hottinger Baldwin Messtechnik GmbH, 1989.

[38] [Online]. Available: http://www.kyowa-ei.com/.

[39] [Online]. Available: www.meas-spec.com.

[40] [Online]. Available: www.o-eland.com.

[41] R. M. White and F. W. Voltmer, "Direct piezoelectric coupling to surface elastic waves," *Applied Physics Letters,* vol. 7, no. 12, pp. 314-316, 1965.

[42] D. S. Jr. Ballantine *et al.*, Acoustic Wave Sensors - Theory, Design, and Physico-Chemical Applications, Elsevier, 1997.

[43] J. Sirohi and I. Chopra, "Fundamental understanding of piezoelectric strain sensors," *J. Intell. Mater. Syst. Struct.,* vol. 11, no. 4, p. 246–257, 2000.

[44] G. K. Fedder et al., "Technologies for cofabricating MEMS and electronics," *in Proc. IEEE,* vol. 96, no. 2, p. 306–322, 2008.

[45] W. A. Clark, R. T. Howe and R. Horowitz, "Surface micromachined z-axis vibratory rate gyroscope," in *Tech. Dig. Solid-State Sensor and Actuator Workshop*, Hilton Head Island, SC, 1996.

[46] J. -c. Tsai and M. C. Wu, "Design, fabrication, and characterization of a high fill-factor, large scan-angle, two-axis scanner array driven by a leverage mechanism," *J. Microelectromech. Syst.,* vol. 15, no. 2, p. 1209–1213, 2006.

[47] "MEMS Accelerometers," Analog Devices Inc., Norwood, MA, [Online]. Available: http://www.analog.com/en/mems-sensors/mems-accelerometers/products/index.html.

[48] I. Zeimpekis, I. Sari and M. Kraft, "Characterization of a mechanical motion amplifier applied to a MEMS accelerometer," *J. Microelectromech. Syst.,* vol. 12, no. 5, p. 1032–1042, 2012.

[49] M. Suster *et al.*, "Characterization of a mechanical motion amplifier applied to a MEMS accelerometer," *J. Microelectromech. Syst.,* vol. 15, no. 5, p. 1069–1077, 2006.

[50] L. Que, J. -S. Park and Y. B. Gianchandani, "Bent-beam electrothermal actuators-part I: single beam and cascaded devices," *J. Microelectromech. Syst.,* vol. 10, no. 2, p. 247–254, 2001.

[51] L. L. Chu, L. Que and Y. B. Gianchandani, "Measurements of material properties using differential capacitive strain sensors," *J. Microelectromech. Syst.,* vol. 11, no. 5, p. 489–498, 2002.

[52] D. G. Senesky and B. Jamshidi, "MEMS strain sensors for intelligent structural systems," in *New Developments in Sensing Technology for Structural Health Monitoring, Lecture Notes in Electrical Engineering vol. 96*, vol. 96, 2011, p. 63–74.

[53] R. G. Azevedo *et al.*, "A SiC MEMS resonant strain sensor for harsh environment application," *IEEE Sensors J.,* vol. 7, no. 4, p. 568–576, 2007.

[54] A. Arslan *et al.*, "Comb-actuated resonant torsional microscanner with mechanical amplification," *J. Microelectromech. Syst.,* vol. 19, no. 4, p. 936–943, 2010.

[55] M. J. Sinclair, "A high force low area MEMS thermal actuator," in *in Proc. IEEE Inter Society Conference on Thermal Phenomena*, 2000.

[56] Y. B. Gianchandani and K. Najafi, "Bent-beam strain sensors," *J. Microelectromech. Syst.,* vol. 5, no. 1, p. 52–58, 1996.

[57] M. Moradi and S. Sivoththaman, "Strain transfer analysis of surface-bonded MEMS strain sensors," *IEEE Sensors J.,* vol. 13, no. 2, p. 637–643, 2013.

[58] S. D. Senturia, Microsystems Design, Boston, MA: Kluwer Academic, 2000.

[59] J. Guo *et al.*, "Buckled beam linear output capacitive strain sensor," *in Solid-State Sensor, Actuator and Microsystems Workshop*, 2004.

[60] J. Qiu, J. H. Lang and A. H. Slocum, "A curved-beam bistable mechanism," *J. Microelectromech. Syst.,* vol. 13, no. 2, p. 137–146, 2004.

[61] L. F. Campanile and A. Hasse, "A Simple and Effective Solution of the Elastica Problem," *J. Mech. Eng. Sci.,* vol. 222, no. 12, p. 2513–2516, 2008.

[62] A. Banerjee, B. Bhattacharya and A. K. Mallik, "Large deflection of cantilever beams with geometric non-linearity: analytical and numerical approaches," *Int. J. Non-Linear Mech.,* vol. 43, no. 5, p. 366–376, 2008.

[63] J. M. Gere and S. P. Timoshenko, Mechanics of Materials (2nd Edition)., Monterey, CA: Brooks/Cole Engineering Division, 1984.

[64] M. Abramowitz and I. A. Stegun, Handbook of Mathematical Functions with Formulas, Graphs, and Mathematical Tables, New York: Dover, 1965.

[65] W. C. Tang, M. G. Lim and R. T. Howe, "Electrostatic comb drive levitation and control method," *J. Microelectomech. Syst.,* vol. 1, no. 4, p. 170–178, 1992.

[66] C. Acar and A. M. Shkel, "An approach for increasing drive-mode bandwidth of MEMS vibratory gyroscopes," *J. Microelectromech. Syst.,* vol. 14, no. 3, p. 520–528, 2005.

[67] V. Mosser, J. Suski, J. Goss and E. Obermeier, "V. Mosser, J. Suski, J. Goss, and E. Obermeier, “Piezoresistive pressure sensors based on polycrystalline silicon," *Sens. Actuators A, Phys.,* vol. 28, no. 2, p. 113–132, 1991.

[68] J. J. Dosch, D. J. Inman and E. Garcia, "A self-sensing piezoelectric actuator for collocated control," *J. Intell. Mater. Structures,* vol. 3, no. 1, p. 166–185, 1992.

[69] S. Bhalla and C. K. Soh, "Electromechanical impedance modeling for adhesively bonded piezo-transducers," *J. Intell. Mater. Structures,* vol. 15, no. 12, p. 955–972, 2004.

[70] R. Kashyap, Fiber Bragg Gratings, London: Academic Press, 1999.

[71] W. Montero *et al.*, "Uncertainties associated with strain-measuring systems using resistance strain gauges," *J. Strain Analysis,* vol. 46, no. 1, p. 1–13, 2011.

[72] C. Hautamaki *et al.*, "Calibration of MEMS strain sensors fabricated on silicon: Theory and experiments," *J. Microelectromech. Syst.,* vol. 12, no. 5, p. 720–727, 2003.

[73] M. Suster *et al.*, "A high-performance MEMS capacitive strain sensing microsystem," *IEEE J. Microelectromech. Syst.,* vol. 15, no. 5, p. 1069–1077, 2006.

[74] E. F. Crawley and J. de Luis, "Use of piezoelectric actuators as elements of intelligent structures," *AIAA J.,* vol. 25, p. 1373–1385, 1985.

[75] W. Y. Li, C. C. Cheng and Y. L. Lo, "Investigation of strain transmission of surface-bonded FBGs used as strain sensors," *Sens. Actuators A, Phys.,* vol. 149, no. 2, p. 201–207, 2009.

[76] H. Fukuda and T. W. Chou, "An advanced shear-lag model applicable to discontinuous fiber composites," *J. Composite Materials,* vol. 15, no. 1, p. 79–91, 1981.

[77] M. S. Troitsky, Stiffened Plates: Bending, Stability and Vibrations, Amsterdam: Elsevier Scientific Publishing, 1976.

[78] H. L. Cox, "The elasticity and strength of paper and other fibrous materials,” *Brit. J. Appl. Phys.*, vol. 3, no. 3, p. 72, 1952.," *Brit. J. Appl. Phys.,* vol. 3, no. 3, p. 72, 1952.

[79] O. Volkersen, "Recherches sur la theorie des assemblages colles," *Construction Metallique,* vol. 4, no. 3, 1965.

[80] R. D. Adams and N. A. Peppiatt, "Stress analysis of adhesive-bonded lap joints," *J. Strain Analysis,* vol. 9, no. 3, p. 185–196, 1974.

[81] S. P. Kotha, S. Kotha and N. Guzelsu, "A shearlag model to account for interaction effects between inclusions in composites reinforced with rectangular platelets," *Compos. Sci. Technol.,* vol. 60, no. 11, p. 2147–2158, 2000.

[82] V. Lindroos, M. Tilli, A. Lehto and T. Motooka, Handbook of Silicon Based MEMS Materials and Technologies, Norwich, NY: William Andrew, 2010.

[83] Z. J. Guo *et al.*, "Effective magnetostriction and magnetomechanical coupling of Terfenol-D composites," *Appl. Phys. Lett.,* vol. 78, no. 22, p. 3490–3492, 2001.

[84] D. A. Bigwood and A. D. Crocombe, "Elastic analysis and engineering design formulae for bonded joints," *Int. J. Adhesion Adhesives,* vol. 9, no. 4, p. 229–242, 1989.

[85] C.-E. Morosanu, "The preparation, characterization and applications of silicon nitride thin films," *Thin Solid Films,* vol. 65, no. 2, pp. 171-208, 1980.

[86] D. L. Smith *et al.*, "Mechanism of SiNxHy Deposition from NH3–SiH4 Plasma," *J. Electrochem. Soc.,* vol. 137, no. 2, p. 614–623, 1990.

[87] P. J. French *et al.*, "Optimization of a low-stress silicon nitride process for surface-micromachining applications," *Sens. Actuators A: phys.,* vol. 58, no. 2, p. 149–157, 1997.

[88] J. M. Olson, "Analysis of LPCVD process conditions for the deposition of low stress silicon nitride. Part I: preliminary LPCVD experiments," *Materials Science in Semiconductor Processing,* vol. 5, no. 1, p. 51–60, 2002.

[89] J. G. . E. Gardeniers and H. A. C. Tilmans, "LPCVD silicon-rich silicon nitride films for applications in micromechanics, studied with statistical experimental design," *J. Vac. Sci. Technol. A,* vol. 14, no. 5, p. 2879–2892, 1996.

[90] Y. Toivola *et al.*, "Influence of deposition conditions on mechanical properties of low-pressure chemical vapor deposited low-stress silicon nitride films," *J. Appl. Phys.,* vol. 94, no. 10, p. 6915–6922, 2003.

[91] P. Temple-Boyer *et al.*, "Residual stress in low pressure chemical vapor deposition SiNx films deposited from silane and ammonia," *J. Vac. Sci. Technol. A,* vol. 16, no. 4, p. 2003–2007, 1998.

[92] M. Maeda and K. Ikeda, "Stress evaluation of radio-frequency-biased plasma-enhanced chemical vapor deposited silicon nitride films," *J. Appl. Phys.,* vol. 83, no. 7, p. 3865–3870, 1998.

[93] S. Habermehl, "Stress relaxation in Si-rich silicon nitride thin films," *J. Appl. Phys.,* vol. 83, no. 9, p. 4672–4677, 1998.

[94] W. A. P. Claassen *et al.*, "Influence of deposition temperature, gas pressure, gas phase composition, and RF frequency on composition and mechanical stress of plasma silicon nitride layers," *J. Electrochem. Soc.,* vol. 132, no. 4, p. 893–898, 1985.

[95] M. P. Hughey and R. Cook, "Massive stress changes in plasma-enhanced chemical vapor deposited silicon nitride films on thermal cycling," *Thin Solid Films,* vol. 460, no. 1, p. 7–16, 2004.

[96] I. Kobayashi, T. Ogawa and S. Hotta, "Plasma-enhanced chemical vapor deposition of silicon nitride," *J. J. Appl. Phys.,* vol. 31, no. 2A, p. 336, 1992.

[97] S. A. Campbell, The science and engineering of microelectronic fabrication, New York: Oxford University Press, 1996.

[98] P. Eriksson, J. Y. Andersson and G. Stemme, "Thermal characterization of surface-micromachined silicon nitride membranes for thermal infrared detectors," *J. Microelectromech. Sys.,* vol. 6, no. 1, p. 55–61, 1997.

[99] A. Tarraf *et al.*, "Stress investigation of PECVD dielectric layers for advanced optical MEMS," *J. Micromech. Microeng.,* vol. 14, no. 3, p. 317–323, 2004.

[100] J. Bühler, F. P. Steiner and H. Baltes, "Silicon dioxide sacrificial layer etching in surface micromachining," *J. Micromech. Microeng. R1,* vol. 7, no. 1, 1997.

[101] K. D. Mackenzie *et al.*, "Stress control of Si-based PECVD dielectrics," in *207th Electrochemical Society Meeting*, Quebec City, 2005.

[102] M. J. Loboda and J. A. Seifferly, "Chemical influence of inert gas on the thin film stress in plasma-enhanced chemical vapor deposited a-SiN: H films," *J. Mat. Res.,* vol. 11, no. 2, p. 391–398, 1996.

[103] R. W. Hoffman, "The mechanical properties of thin condensed films," *Physics of thin films,* vol. 3, p. 211–273, 1966.

[104] D. A. G. Bruggeman, "Calculation of various physics constants in heterogeneous substances | Dielectricity constants and conductivity of mixed bodies from isotropic substances," *Ann. Phys.,* vol. 24, no. 7, p. 636–664, 1935.

[105] M. Born and E. Wolf, Principles of Optics, Oxford: Pergamon Press, 1975.

[106] G. G. Stoney, "The tension of metallic films deposited by electrolysis," *Proc. R. Soc. London, Series A,* vol. 82, no. 553, pp. 172-175, 1909.

[107] W. A. Brantley, "Calculated elastic constants for stress problems associated with semiconductor devices," *J. Appl. Phys.,* vol. 44, no. 1, p. 534–535, 1973.

[108] L. K. Nanver, P. J. French and E. J. G. Goudena, "Low stress nitride as surface isolation in bipolar transistor," *Mater. Schi. Technol.,* vol. 11, p. 36–40, 1995.

[109] D. V. Tsu, G. Lucovsky and M. J. Mantini, "Local atomic structure in thin films of silicon nitride and silicon diimide produced by remote plasma-enhanced chemical-vapor deposition," *Phys. Rev. B,* vol. 33, p. 7069, 1986.

[110] P. N. Sen and M. F. Thorpe, "Phonons in A X 2 glasses: From molecular to band-like modes," *Phys. Rev. B,* vol. 15, no. 8, p. 4030, 1977.

[111] V. Y. Doo, D. R. Nichols and G. A. Silvey, "Preparation and properties of pyrolytic silicon nitride," *J. Electrochem. Soc.,* vol. 113, no. 12, p. 1279–1281, 1966.

[112] M. P. Hughey and R. F. Cook, "Stress development kinetics in plasma-enhanced chemical-vapor-deposited silicon nitride films," *J. Appl. Phys.,* vol. 97, no. 11, p. 114914, 2005.

[113] A. V. Rhanov (Ed.), Silicon Nitride in Electronics, Amsterdam: Elsevier, 1988.

[114] A. K. Sinha, H. J. Levinstein and T. E. Smith, "Thermal stresses and cracking resistance of dielectric films (SiN, Si3N4, and SiO2) on Si substrates," *J. Appl. Phys.,* vol. 49, no. 4, p. 2423–2426, 1978.

[115] G. E. Robertson, J. H. Seinfeld and L. G. Leal, "Combined forced and free convection flow past a horizontal flat plate," *AIChE Journal,* vol. 19, no. 5, pp. 998–1008, 1973.

[116] S. T. McComas and E. R. G. Eckert, "Combined free and forced convection in a horizontal circular tube," *Journal of Heat Transfer,* vol. 88, no. 2, pp. 147–152, 1966.

[117] A. S. Grove, Physics and Technology of Semiconductor Devices, New York: Wiley, 1967.

[118] W. A. P. Claassen *et al.*, "The deposition of silicon from silane in a low-pressure hot-wall system," *Journal of Crystal Growth,* vol. 57, no. 2, pp. 259–266, 1982.

[119] M. E. Coltrin, R. J. Kee and J. A. Miller, "A mathematical model of the coupled fluid mechanics and chemical kinetics in a chemical vapor deposition reactor," *Journal of The Electrochemical Society,* vol. 131, no. 2, pp. 425–434, 1984.

[120] B. S. Meyerson and J. M. Jasinski, "Silane pyrolysis rates for the mdeling of chemical vapor deposition," *J. Appl. Phys.,* vol. 61, pp. 785–787, 1987.

[121] T. I. Kamins, "Design properties of polycrystalline silicon," *Sensors and Actuators A: Physical,* vol. 23, no. 1, pp. 817–824, 1990.

[122] A. C. Adams, "Dielectric and polysilicon film deposition," in *VLSI Technology*, McGraw-Hill, 1983, pp. 93–129.

[123] F. C. Eversteyn and B. H. Put, "Influence of AsH3, PH 3, and B 2 H 6 on the Growth Rate and Resistivity of Polycrystalline Silicon Films Deposited from a SiH4-H 2 Mixture," *Journal of the Electrochemical Society,* vol. 120, no. 1, pp. 106–110, 1973.

[124] M. L. Yu and B. S. Meyerson, "The adsorption of PH3 on Si (100) and its effect on the coadsorption of SiH4," *Journal of Vacuum Science & Technology A,* vol. 2, no. 2, pp. 446–449, 1984.

[125] F. L-S, T. Y-C and R. S. Muller, "Integrated movable micromechanical structures for sensors and actuators," *IEEE Trans. Electron Devices,* vol. 35, no. 6, pp. 724–730, 1988.

[126] S. Wolf and R. N. Tauber, "Silicon Processing for the VLSI Era Vol. 1," CA, Lattice Press, p. 529–534.

[127] J. M. E. Harper, "Ion Beam Etching, in D. M. Manos and D. L. Flamm (eds.)," in *Plasma Etching – An Introduction*, San Diego, Academic Press, p. 391–423.

[128] C. J. Mogab, A. C. Adams and D. L. Flamm, "Plasma etching of Si and SiO2 – The effect of Oxygen addition to CF4 plasmas," *Journal of Applied Physics,* vol. 49, no. 7, p. 3796–3803, 1978.

[129] K. B. Lee, Principles of microelectromechanical systems, John Wiley & Sons, 2011.

[130] B. Lu, Y. Li, X. Wu and Z. Yang, "A review of recent advances in wind turbine condition monitoring and fault diagnosis," in *Power Electronics and Machines in Wind Applications, PEMWA.*, 2009.

[131] A. Ghoshal *et al.*, "Structural health monitoring techniques for wind turbine blades," *Journal of Wind Engineering and Industrial Aerodynamics,* vol. 85, no. 3, 2000.

[132] J. Park et al., "Linear vibration analysis of rotating wind-turbine blade," *Curr. Appl. Phys.,* vol. 10, no. 2, p. S332–S334, 2010.

[133] A. N. Steinberg, "Data fusion system engineering," *IEEE AESS Syst. Mag.,* vol. 16, no. 6, p. 7–14, 2001.

[134] K. Worden and J. M. Dulieu-Barton, "An overview of intelligent fault detection in systems and structures," *International Journal of Structural Health Monitoring,* vol. 3, no. 1, p. 85–98, 2004.

[135] "[24] M. Carminati, G. Ferrari, R. Grassetti, and M. Sampietro, "Real-time data fusion and MEMS sensors fault detection in an aircraft emergency attitude unit based on Kalman filtering," IEEE Sensors Journal, vol. 12, no. 10, pp. 2984–2992, 2012.," *IEEE Sensors Journal,* vol. 12, no. 10, p. 2984–2992, 2012.

[136] R. C. Lou and M. Lin, "Dynamic multi-sensor data fusion system for intelligent robots," *IEEE J. Robot Automation,* vol. 4, no. 4, p. 386–396, 1988.

[137] D. L. Hall, Mathematical Techniques in multisensor Data Fusion, Boston, MA: Artech House, Inc, 1992.

[138] G. Shafer, A Mathematical Theory of Evidence, Princetonm NJ: Princeton Univ. Press, 1976.

[139] M. J. Sundaresan, M. J. Schulz and A. Ghoshal, "Structural health monitoring static test of a wind turbine blade," National Renewable Energy Laboratory, CO, USA, 2002.

[140] M. M. Shokrieh and R. Rafiee, "Simulation of fatigue failure in a full composite wind turbine blade," *Compos. Struct.,* vol. 74, no. 3, p. 332–342, 2006.

[141] Z. Hameed, *et al.*, "Condition monitoring and fault detection of wind turbines and related algorithms: A review," *Renewable and Sustainable energy reviews,* vol. 13, no. 1, p. 1–39, 2009.

[142] M. Meo and G. Zumpano, "On the optimal sensor placement techniques for a bridge structure," *Eng. Struct.,* vol. 27, p. 1488–1497, 2005.

[143] E. R. Jørgensen, *et al.*, "Full scale testing of wind turbine blade to failure—flapwise loading," Risø-R-1392(EN) Report Risø National Laboratory, Denmark, 2004.

[144] G. Roebben, *et al.*, "Impulse excitation apparatus to measure resonant frequencies, elastic moduli, and internal friction at room and high temperature," *Review of scientific instruments,* vol. 68, no. 12, p. 4511–4515, 1997.

[145] B. D. O. Anderson and J. B. Moore, Optimal Filtering, Englewood Cliffs, N.J.: Prentice-Hall, 1979.

[146] H. B. Mitchell, Multi-Sensor Data Fusion: An Introduction, Berlin, Germany: Springer-Verlag, 2007.

[147] R. C. Luo, C. C. Chang and C. C. Lai, "Multisensor fusion and integration: theories, applications, and its perspectives," *IEEE Sensors Journal,* vol. 11, no. 12, p. 3122–3138, 2011.

[148] J. K. Hackett and M. Shah, "Multi-sensor fusion: a perspective," in *IEEE Int. Conf. on Robotics and Automation*, 1990.

[149] N. Persson, F. Gustafsson and M. Drevo, "Indirect tire pressure monitoring using sensor fusion," in *Proceedings SAE 2002*, Detroit, 2002.

[150] D. A. Griffin, "WindPACT turbine design scaling studies technical area 1–composite blades for 80- to 120-meter rotor," NREL/SR-500-29492, National Renewable Energy Laboratory, Golden, CO, 2001.

[151] J. C. Watson and J. C. Serrano, "Composite materials for wind blades," 2010. [Online]. Available: http://www.ppg.com/glass/fiberglass/products/Documents/WindSystems_PPG%20%20-Hybon.pdf.

[152] A. M. Sadri, J. R. Wright and R. J. Wyne, "Modelling and optimal placement of piezoelectric actuators in isotropic plates using genetic algorithms," *Smart Structures and Materials,* vol. 8, no. 4, p. 490–498, 1999.